



**OPTICAL AND ELECTRICAL CHARACTERIZATION OF MELT-GROWN
BULK INDIUM GALLIUM ARSENIDE AND INDIUM ARSENIC PHOSPHIDE
ALLOYS**

DISSERTATION

JEAN WEI

AFIT/DS/ENP/11-M02

**DEPARTMENT OF THE AIR FORCE
AIR UNIVERSITY**

AIR FORCE INSTITUTE OF TECHNOLOGY

Wright-Patterson Air Force Base, Ohio

APPROVED FOR PUBLIC RELEASE; DISTRIBUTION UNLIMITED

The views expressed in this dissertation are those of the author and do not reflect the official policy or position of the United States Air Force, the Department of Defense, or the United States Government. This material is declared a work of the U.S. Government and is not subject to copyright protection in the United States.

AFIT/DS/ENP/11-M02

OPTICAL AND ELECTRICAL CHARACTERIZATION OF MELT-
GROWN BULK INDIUM GALLIUM ARSENIDE AND INDIUM
ARSENIC PHOSPHIDE ALLOYS

DISSERTATION

Presented to the Faculty

Department of Engineering Physics

Graduate School of Engineering and Management

Air Force Institute of Technology

Air University

Air Education and Training Command

In Partial Fulfillment of the Requirements for the

Degree of Doctor of Philosophy

Jean Wei, BS, MS

March 2011

APPROVED FOR PUBLIC RELEASE; DISTRIBUTION UNLIMITED

OPTICAL AND ELECTRICAL CHARACTERIZATION OF MELT-GROWN
BULK INDIUM GALLIUM ARSENIDE AND INDIUM ARSENIC PHOSPHIDE
ALLOYS

Jean Wei, BS, MS

Approved:

//SIGNED//

Yung Kee Yeo, PhD (Chairman)

Date

//SIGNED//

Robert Hengehold, PhD (Member)

Date

//SIGNED//

Shekhar Guha, PhD (Member)

Date

//SIGNED//

Mark Oxley, PhD (Member)

Date

Accepted:

//SIGNED//

M. U. Thomas
Dean, Graduate School of
Engineering and Management

Date

Abstract

Optical and electrical properties of bulk melt-grown ternary $\text{InAs}_{1-y}\text{P}_y$ and $\text{In}_x\text{Ga}_{1-x}\text{As}$ polycrystals were investigated as functions of phosphorus and indium compositions and temperatures using the photoluminescence, Fourier transform infrared (FTIR) transmission spectrum, refractive index, and Hall-effect measurements. These ternary alloys were grown using the vertical Bridgman techniques. The as-grown undoped bulk ternary $\text{InAs}_{1-y}\text{P}_y$ and $\text{In}_x\text{Ga}_{1-x}\text{As}$ polycrystals have been found to exhibit n-type conductivity irrespective of the alloy compositions possibly due to residual impurities and native defects. In general, carrier concentrations and Hall mobilities increase with the indium composition for $\text{In}_x\text{Ga}_{1-x}\text{As}$, whereas they decrease with increasing phosphorus mole fraction for the $\text{InAs}_{1-y}\text{P}_y$ sample. The FTIR spectra of all these ternary samples demonstrated good infrared transmission. A systematic measurement of photoluminescence was carried out in order to gain insight into the various radiative transitions in the $\text{InAs}_{1-y}\text{P}_y$ and $\text{In}_x\text{Ga}_{1-x}\text{As}$ crystals, which include the temperature, laser excitation power, and sample location dependent studies. The wavelength, temperature, and composition dependent refractive indices of $\text{InAs}_{1-y}\text{P}_y$ and $\text{In}_x\text{Ga}_{1-x}\text{As}$ were studied using minimum deviation and Michelson Fabry-Perot interferometry methods. The measured results of refractive indices, transport properties, bandgap energies, and optical transmissions are presented here as functions of alloy composition, temperature and photon energy for the first time, to the best of our knowledge. Although the bulk $\text{InAs}_{1-y}\text{P}_y$ and $\text{In}_x\text{Ga}_{1-x}\text{As}$ samples show good optical

transmissions, PL transitions, and high carrier mobilities, they do exhibit some random compositional fluctuations across the sample. A practical method of extracting bandgap energies directly from the FTIR transmission spectra has been presented in this work, and the results are promising even though further refinement is required. Bandgap energies estimated from the transmission spectra agree well with those obtained from PL spectra and the previously reported values from the thin film studies. Overall, the optical and electrical properties of these crystals are well suited for a variety of device applications that do not require single crystalline material.

Acknowledgments

Writing this dissertation has been one of the greatest challenges of my life. Without the support and guidance of my colleagues, family and friends, I would never have been able to complete it. First of all, I must thank Dr. Yung Kee Yeo, my advisor, who deserves many thanks for all of his advice, corrections, and insight throughout the project. His assistance was indispensable. Dr. Shekhar Guha, Dr. Leo Gonzalez, Dr. Joel Murray, and Jacob Barnes, Derek Upchurch, and Amelia Carpenter from IR Lab were also invaluable. They offered countless tips on the experimental design and minutiae of lab equipment, provided help in trouble shooting, and set things straight when I came perilously close to serious damage. Without them I would probably be wandering in the darkness. Thanks to Dr. Glen Gillen from California Polytechnic, who developed the interferometry refractive index measurement and trained me in its use. Thanks to Dr. Elizabeth Moore who trained me to use the Hall system at AFIT. Dr. Mee-Yi Ryu was also of great assistance as her kindness, needed guidance, and useful discussions were critical to my success. Thanks to 1st Lt Austin Bergstrom who had made the PL system finally works. Thanks to Partha Dutta and Geeta Rajagopalan; they provided me 99% of the samples in this work. Thanks to Steve Molla, who has offered consistent support and reviewed my drafts for typos and grammar errors. Last but not least, thanks to my family (my daughter and my parents), for without them this effort would be worth nothing. Their love, patience, and support gave me the foundation I needed to complete this study.

Jean Wei

Table of Contents

	Page
Abstract	iv
Acknowledgments.....	vi
List of Figures	ix
List of Tables	xv
1. Introduction	1
Motivation	1
Objective.....	4
Approach	5
Dissertation Summary and Layout	5
2. Theory	7
Semiconductor Basics	7
Bulk III-V Ternary Crystal Growth.....	8
Band Structure and Bandgap Energy	11
Temperature Effects on Semiconductors.....	15
Semiconductor Impurities	17
3. Characterization Techniques and Experimental Setups	19
Electrical Characterization	19
<i>Hall-effect Theory</i>	19
<i>Hall-effect Measurement System</i>	23
Optical Characterization.....	25
<i>Fourier Transform Infrared Spectroscopy</i>	25
<i>Photoluminescence Measurement</i>	27
Refractive Index	34
<i>Prism Based Measurement Using Minimum Deviation Method</i>	34
<i>Wafer Based Measurement Using Michelson and Fabry-Perot Interferometer</i>	35
Electron Probe Micro Analyzer (EPMA)	40
Infrared Imagery	42
4. Results and Discussions of Binary InAs, InP, and GaAs	45
Purpose	45
Determination of Bandgap Energy	45

	Page
<i>Bandgap Energy Obtained from Transmission Spectra for InAs</i>	48
Temperature Dependent Bandgap Energy Obtained from Transmission Spectra.....	52
<i>Temperature Dependent Bandgap of InAs</i>	53
<i>Temperature Dependent Bandgap of InP</i>	60
<i>Temperature Dependent Bandgap of GaAs</i>	65
Determination of dn/dT from dE_g/dT	68
Refractive-Index Measurements.....	69
5. Results and Discussions on Bulk Ternary $InAs_{1-y}P_y$	73
Ternary $InAs_{1-y}P_y$ Crystal Growth.....	73
Bulk $InAs_{1-x}P_y$ Crystal Images	76
Bandgap Energy of Bulk $InAs_{1-y}P_y$	78
Photoluminescence Measurements.....	81
Refractive Index Measurements	91
Hall-effect Measurements	96
6. Results and Discussions on Bulk Ternary $In_xGa_{1-x}As$	99
Ternary $In_xGa_{1-x}As$ Crystal Growth	99
Bandgap Energy of Bulk $In_xGa_{1-x}As$	101
Photoluminescence Studies	104
<i>Sample Location Dependent PL Measurements</i>	105
<i>Laser Excitation Power Dependent PL Measurements</i>	108
<i>Temperature Dependent PL Measurements</i>	113
Refractive Index Measurements	119
Hall-effect Measurements	120
7. Conclusions and Future Work	122
Appendix A	128
Appendix B	129
Appendix C	134
Bibliography	137

List of Figures

Figure	Page
1.1. Bandgap energy vs. lattice constant (\AA) at 300 K for various III-V semiconductors.	2
2.1. Crystal lattice structure	8
2.2. A schematic pseudobinary phase diagram of a III-V ternary compound(GaInSb)	9
2.3. Schematic lattice constant match and mismatch effects on the quality of crystal.....	10
2.4. Vertical Bridgman growth of $\text{Ga}_{1-x}\text{In}_x\text{Sb}$ system.....	11
2.5. A typical bandgap structure	12
2.6. Illustration of band structures of semiconductor materials.....	15
3.1. A schematic diagram illustrating of the van der Pauw Hall-effect.....	21
3.2. A schematic diagram of the LakeShore 7505 automated Hall measurement system	24
3.3. A schematic layout of Perkin Elmer Spectrum GX FTIR system with the PC interface.....	27
3.4. Common radiative transitions take place in semiconductors. (a) band-to-band, (b) free exciton, (c) neutral donor and free hole recombination, (d) a free electron transitioning to a neutral shallow acceptor, and (e) (f) donor-acceptor transitions for shallow and deep states, respectively.	29
3.5. Experimental setup for the PL measurement	32
3.6. (a) Illustration of a ray of light dispersed through a prism, and (b) deviation angle vs. incident angle. Red data points are measured at 295 K and blue at 100 K with an InP prism at $4.6\text{ }\mu\text{m}$	34
3.7. (a) Prism dimensions (b) Minimum deviation method experimental layout	35
3.8. Schematic Michelson and Fabry-Perot interferometers layout.....	36

Figure	Page
3.9. Illustration of optical path nd changing with rotating angle θ	37
3.10. (Top) Michelson interferometer interference pattern observed at a detector; (Bottom) phase information extracted from the interference pattern for both setups and their difference	38
3.11. (Top) Electron probe micro analyzer (EPMA): CAMECA 100. (Bottom) a typical analysis spectrum of EPMA	41
3.12. Santa Barbara focaplance image IR infrared camera.....	42
3.13. MIR imaging system using Santa Barbara Focalplane ImagIR.....	43
3.14. MIR images of six InAs crystals using Santa Barbara focal plane infrared camera	44
4.1. (a) A theoretical graph of the absorption coefficient and its first derivative in a uniform bulk sample showing a sharp peak of the derivative in the vicinity of the bandgap. (b) The second derivative of the absorption coefficient for different values of bandgap variation within the sample.	48
4.2. (a) Transmission spectra of InAs 143 samples with five thicknesses (b) $d(-T)/dE$ vs. E . Peak locations are defined as $E_{L\ min}$. (c) $d^2(-T)/dE^2$ vs. E . The minimum locations are defined as $E_{L\ max}$. E is a photon energy.....	50
4.3. $E_{L\ min}$ and $E_{L\ max}$ vs. sample thickness for a set of InAs 143 samples.....	51
4.4. (top) Temperature dependent transmission spectra of InAs sample WT 524-10; (bottom) temperature dependent $\left(-\frac{dT}{dE}\right)$ plotted as a function of photon energy.....	54
4.5. $E_{L\ min}$ (red dot) extracted from transmission spectra of InAs and bandgap energy of InAs by Fang <i>et al.</i> (solid curve).....	55
4.6. $E_L \ln(dC)$ vs. temperature and a fitting curve with $E_g - E_{L\ min} = \theta T^b$, with $b=0.5$	56
4.7. Temperature dependent bandgap energy obtained from transmission spectra (red dots) and published results (solid curve) by Fang, <i>et al.</i>	57

Figure	Page
4.8. Temperature dependent transmission spectra of three InAs samples (a) InAs WT 524-11 (b) InAs D1 (c) InAs 100	58
4.9. Temperature dependent bandgap energies of four InAs samples (symbols). The solid curve is temperature dependent bandgap energies reported by Fang <i>et al.</i>	59
4.10. Temperature dependent transmission spectra of three InP samples (a) InP B2 (b) InP R3781 un (c) InP 6.....	61
4.11. $\frac{d(1-T)}{dE}$ vs. E for InP sample at various temperatures (a) InP sample B2. (b) InP sample R3781_un	62
4.12. (top) $E_{L\min}$ (symbols) of three InP samples and published E_g (solid curve). (bottom) $(E_g - E_{L\min})$ plotted as a function of temperature. The curve is fitted with a power series function of θT^b with $b=0.5$	63
4.13. Temperature dependent bandgap energies obtained from transmission spectra (triangle, dot, and square) for three InP samples and published bandgap energies (solid curve).	64
4.14. (a), (b) and (c) Temperature dependent transmission spectra of three GaAs samples of GaAs 82, GaAs WV 19557 and GaAs 12472-24, respectively. (d) $d(1-T)/dE$ of GaAs 12472-24 plotted as a function of photon energy.	66
4.15. (a) Extracted $E_{L\min}$ of three GaAs samples (symbols) and published E_g values (solid curve). (b) Temperature dependent bandgap energies of three GaAs samples obtained from transmission spectra (#, dot, and square) and published E_g values (solid curve)	67
4.16. Obtained θ values of the material plotted as a function of material's refractive index	68
4.17. Prism angle measurement setup.....	70
4.18. (a) Temperature dependent refractive indices of InAs measured at three wavelengths, 3.39, 4.6 and 10.6 μm (b) Best fit curve for dn/dT vs. wavelength	70

Figure	Page
4.19. (a) Temperature dependent refractive index of InP measured at four wavelengths of 1.55, 3.39, 4.6 and 10.6 μm . (b) Best fit curve for dn/dT vs. wavelength.	71
5.1. Crystal boul and crystal wafer of an $\text{InAs}_{1-y}\text{P}_y$ crystal.....	75
5.2. Prism used in refractive index measurements using minimum deviation method...	76
5.3. MIR images of $\text{InAs}_{1-y}\text{P}_y$ crystal samples.....	76
5.4. Images of a laser beam at 4.6 μm , before or passing through $\text{InAs}_{1-y}\text{P}_y$ crystals.....	78
5.5. (Top) Transmission spectra of six $\text{InAs}_{1-y}\text{P}_y$ samples with composition ranging from 0.19 to 0.66; (Bottom) the 1 st derivatives of transmission spectra with respect to photon energy plotted as a function of photon energy	80
5.6. $E_{L\min}$ values obtained from transmission spectra (red dots) plotted as a function of phosphorus composition. The solid line is the bandgap energies of $\text{InAs}_{1-y}\text{P}_y$ calculated from equation 5.1	81
5.7. Location dependent PL spectra of a $\text{InAs}_{0.81}\text{P}_{0.19}$ sample taken at 12 K with a laser excitation power of 300 mW	82
5.8. Photoluminescence spectra of $\text{InAs}_{0.81}\text{P}_{0.19}$ sample measured at 12 K at different incident laser powers.....	84
5.9. Integrated photoluminescence intensities of peaks A and B for $\text{InAs}_{0.81}\text{P}_{0.19}$ sample measured at 12 K plotted as a function of excitation power.	85
5.10. Temperature dependent PL spectra of the $\text{InAs}_{0.81}\text{P}_{0.19}$ with a laser power of 300 mW	86
5.11. FX peak of $\text{InAs}_{0.81}\text{P}_{0.19}$ (red) and $E_{L\min}$ (black) vs. Temperature. E_g (blue) is calculated using Eq. $E_g = E_{L\min} + \theta\sqrt{T}$	88
5.12. FX peak (red dots) and $E_{L\min}$ (black) of $\text{InAs}_{0.81}\text{P}_{0.19}$ vs. Temperature. E_g is calculated using Eq. $E_g = E_{L\min} + \theta\sqrt{T}$ (blue), and the Varshni equation solid black line	89

Figure	Page
5.13. Temperature dependent bandgap energy of $\text{InAs}_{1-y}\text{P}_y$ and their linear fit	90
5.14. Refractive index of $\text{InAs}_{0.81}\text{P}_{0.19}$ alloy as a function of temperature	92
5.15. Refractive index of $\text{InAs}_{0.81}\text{P}_{0.19}$ alloy as a function of wavelength	93
5.16. Refractive Index of $\text{InAs}_{0.81}\text{P}_{0.19}$ measured at 4.6 μm , and at 95 K and 295 K as a function of composition.....	94
5.17. Measured dn/dT values of $\text{InAs}_{1-y}\text{P}_y$ alloy for $y=0.00, 0.19, 1.00$	95
5.18. Hall-effect measurement data at 77 and 295 K for various $\text{InAs}_{1-y}\text{P}_y$ samples as a function of phosphorus mole fraction: (a) carrier concentration and (b) Hall mobility.	96
5.19. Temperature dependent Hall-effect measurements for the $\text{InAs}_{0.9}\text{P}_{0.1}$ from 20 to 310K.....	97
6.1. Crystal boul (a), crystal wafer (b), and Mid IR image (c) of $\text{In}_x\text{Ga}_{1-x}\text{As}$	101
6.2. (Top) Room temperature transmission spectra of various $\text{In}_x\text{Ga}_{1-x}\text{As}$ samples. (Bottom) First derivatives of transmission spectra with respect to photon energy plotted as a function of photon energy. For $x = 0$, the peak position should be read from the top horizontal scale, and for the rest of $x \geq 0.75$, the peak positions should be read from the bottom horizontal scale.	103
6.3. The estimated bandgap energy $E_g = (E_{L \min} + 0.03x + 0.045(1-x))$ from transmission spectra (red dot) for $\text{In}_x\text{Ga}_{1-x}\text{As}$ plotted as a function of In mole fraction. The solid curve represents banggap energies obtained from the published thin film E_g equation.	104
6.4. Location dependent photoluminescence spectra of $\text{In}_{0.75}\text{Ga}_{0.25}\text{As}$ measured at 12 K with a laser incident excitation power of 100 mW	105
6.5. Position-dependent photoluminescence spectra for the $\text{In}_{0.82}\text{Ga}_{0.18}\text{As}$ measured at 12 K at five different positions with a laser excitation power of 100 mW	107
6.6. Excitation power dependent PL spectra for $\text{In}_{0.75}\text{Ga}_{0.25}\text{As}$ measured at 12 K.	109

Figure	Page
6.7. Integrated photoluminescence intensities of peak A for the $\text{In}_{0.75}\text{Ga}_{0.25}\text{As}$ sample measured as a function of laser power at 12 K.	110
6.8. Excitation power dependent PL spectra for $\text{In}_{0.82}\text{Ga}_{0.18}\text{As}$ measured at 12 K.	111
6.9. Integrated photoluminescence intensities of peaks A and B for the $\text{In}_{0.82}\text{Ga}_{0.19}\text{As}$ sample measured as a function of laser power at 12 K.	112
6.10. Temperature dependent PL spectra for $\text{In}_{0.75}\text{Ga}_{0.25}\text{As}$ with a laser power of 300 mW	114
6.11. Temperature dependent PL spectra for the $\text{In}_{0.82}\text{Ga}_{0.18}\text{As}$ sample	115
6.12. Temperature dependent transmission spectra (a) $\text{In}_{0.75}\text{Ga}_{0.25}\text{As}$; (b) $\text{In}_{0.82}\text{Ga}_{0.18}\text{As}$	116
6.13. Temperature dependent B-B transition nergies of $\text{In}_{0.75}\text{Ga}_{0.25}\text{As}$ sample taken at two sample locations. (Red dot taken at spot B and blue square taken at spot C) along with $E_{L\min}$ (black triangle) obtained from transmission spectra	117
6.14. (a) Temperature dependent FX peaks (red dots) and $E_{L\min}$ (blue square) of the $\text{In}_{0.82}\text{Ga}_{0.18}\text{As}$. (b) E_g (black triangle) calculated using $E_g = E_{L\min} + \theta\sqrt{T}$ with $\theta = 0.0035 \text{ eVK}^{-0.5}$ plotted as a function of temperature. The solid curve is Varshni equation fit	117
6.15. Refractive indices of bulk $\text{In}_x\text{Ga}_{1-x}\text{As}$ measured at 100 K and 295 K using Michelson and Fabry-perot method (a) measured at $4.6 \mu\text{m}$; (b) measured at $10.6 \mu\text{m}$	119
6.16. Hall-effect measurement results at 77 and 300 K for various $\text{In}_x\text{Ga}_{1-x}\text{As}$ samples as a function of indium mole fraction: (a) carrier concentration and (b) Hall mobility	121

List of Tables

Table	Page
3.1 List of samples used in the PL experiments and their composition.....	33
3.2 Refractive index calibration results of a ISP Optics Si window and published results of Si.....	40
4.1 InAs Samples investigated.....	57
4.2 InP Sample Information.....	60
4.3 GaAs sample information	65
4.4 Comparison between calculated dn/dT and experimental dn/dT	69
4.5 Comparison between calculated dn/dT and experimental dn/dT	72
5.1 Bulk ternary $InAs_{1-y}P_y$ sample information	76
5.2 Composition dependent Varshni coefficients summary for $InAs_{1-y}P_y$	90
5.3 Temperature dependent Cauchy coefficients for $InAs_{1-y}P_y$ alloy	92
5.4 Comparison of theoretical and experimental dn/dT for $InAs_{0.81}P_{0.19}$ alloy.....	95
6.1 $In_xGa_{1-x}As$ crystal information.....	102
6.2 Composition-dependent Varshni coefficients for $In_xGa_{1-x}As$	118
6.3 Refractive index of $In_xGa_{1-x}As$ as a function of composition at various wavelengths and temperatures	120

OPTICAL AND ELECTRICAL CHARACTERIZATION OF MELT-GROWN BULK $\text{In}_x\text{Ga}_{1-x}\text{As}$ AND $\text{InAs}_{1-y}\text{P}_y$ ALLOYS

1. Introduction

Ternary crystals such as $\text{In}_x\text{Ga}_{1-x}\text{As}$ and $\text{InAs}_{1-y}\text{P}_y$ are direct bandgap semiconductors with bandgaps ranging from 0.36 eV to 1.42 eV for $\text{In}_x\text{Ga}_{1-x}\text{As}$ and from 0.36 eV to 1.35 eV for $\text{InAs}_{1-y}\text{P}_y$ shown in Fig. 1.1 [1]. Their applications include near to mid infrared light sources such as light emitting diodes (LEDs) and lasers diodes (LDs) [2-9], infrared photo detectors [10-12], high electron mobility transistor (HEMT) devices [13-14], and low bandgap (0.5-0.7 eV) thermophotovoltaic energy conversion devices [15-16]. Early characterization studies for these materials trace back to as early as 1978 [17], but most of these previous studies concentrated on epitaxial films [18-21] grown on bulk binary substrate materials. Bulk sample of $\text{In}_x\text{Ga}_{1-x}\text{As}$ and $\text{InAs}_{1-y}\text{P}_y$ were not commercially available until recently.

1.1 Motivation

These direct bandgap semiconductors are good candidates for Short Wavelength Infrared (SWIR) and Middle Wave Infrared (MWIR) optoelectronic devices due to their bandgap range.

In the past, $\text{In}_x\text{Ga}_{1-x}\text{As}$ and $\text{InAs}_{1-y}\text{P}_y$ ternary thin films were grown on lattice matched or mismatched binary semiconductors such as GaAs, InP, and InAs. Since the lattice constants of GaAs, InP and InAs are 5.6532, 5.8687, and 6.0584 Å, respectively,

as shown in Fig. 1.1 [1], the ability to grow thick, high-quality epitaxial layers of $\text{In}_x\text{Ga}_{1-x}\text{As}$ and $\text{InAs}_{1-y}\text{P}_y$ on a GaAs, InP, or InAs substrate is very limited due to lattice mismatch except for a specific composition [22-25]. For example, only $\text{In}_{0.53}\text{Ga}_{0.47}\text{As}$ lattice matches to InP, and thus very good quality thick films of this composition can be grown on InP. The strained critical thickness of an $\text{In}_x\text{Ga}_{1-x}\text{As}$ or $\text{InAs}_{1-y}\text{P}_y$ epitaxial layer depends on the extent of the lattice mismatch between the ternary epitaxial layer and the binary substrates, normally $< 1 \mu\text{m}$. Also, the strained epitaxial layers grown on lattice mismatched substrates may have strain-induced crystalline defects, which are known cause for dislocations, rough surface morphologies, and interface cracking [26-30]. In order to overcome the limits imposed by lattice mismatch, researchers have tried to pursue growing bulk ternary semiconductor substrates [31-35].

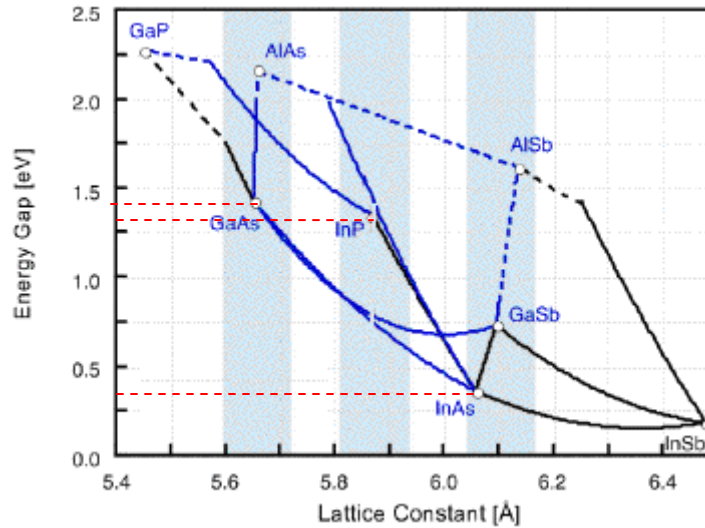


Figure 1.1. Bandgap energy vs. lattice constant (Å) at 300 K for various III-V semiconductors.

The bulk III-V ternary $\text{In}_x\text{Ga}_{1-x}\text{As}$ and $\text{InAs}_{1-y}\text{P}_y$ alloys provide many advantages over epitaxial layers that are grown on binary III-V compound crystals. First, the bulk

ternary alloys can be used as new substrates to grow lattice matched, high quality epitaxial layers with a large thickness for a wide range of compositions and bandgaps. This provides for extra freedom and more opportunities for advancing novel optoelectronic device designs and bandgap engineering. Second, bulk growth is cost effective, and there is strong potential for developing bulk $\text{In}_x\text{Ga}_{1-x}\text{As}$ and $\text{InAs}_{1-y}\text{P}_y$ devices, thus avoiding the expensive and time-consuming epitaxial deposition.

In spite of the promising advantages of bulk $\text{In}_x\text{Ga}_{1-x}\text{As}$ and $\text{InAs}_{1-y}\text{P}_y$ alloys, the utilization of these materials for efficient optoelectronic devices has been hampered by the challenges associated with their growth challenges. Bulk ternary crystal growth requires stringent control over the synthesis conditions in order to avoid crystal defects. The most serious problem encountered in melt-grown bulk ternary material is cracking. Cracking is likely due to the combined results of a large lattice/composition mismatch between the seed and the first-to-freeze crystal, constantly changing composition along the length, and the induced stress due to growth in a steep thermal gradient. Other crystal growth problems such as precipitates, inclusions, residual impurities, high native defect concentrations, and compositional variation across the substrate and from wafer to wafer are also present. In the future, the quality of bulk ternary alloys must improve greatly from its current state.

Since prior research on $\text{In}_x\text{Ga}_{1-x}\text{As}$ and $\text{InAs}_{1-y}\text{P}_y$ alloy systems was limited to a narrow composition range [12, 36-38], adequate knowledge of the optical and electrical properties of this ternary system is lacking. Systematic studies of carrier concentration, mobility, and resistivity for the $\text{In}_x\text{Ga}_{1-x}\text{As}$ and $\text{InAs}_{1-y}\text{P}_y$ alloy systems as functions of composition have not yet been reported although some work have been reported on

InGaAs films [39-40]. Information on the electrical properties of these materials is not only important to electronic device applications, but can also be correlated to optical properties such as carrier concentration dependent optical absorption [41].

For optical device applications, for example, those in waveguide configuration, the refractive index of the active material and substrate must be known to a high accuracy (on the order of 10^{-4}), while current reported values have accuracy on the order of 10^{-1} [42,43]. Furthermore, for nonlinear optical applications, such as smart optical switches, it is important to know the temperature dependent refractive index values. Unfortunately, they are not available in the current literature. Previous refractive index results of ternary semiconductors were limited to theoretical calculations deduced from known binary property parameters [42, 43]. Refractive index measurements on quaternary InGaAsP epitaxial layers grown on InP have been reported [17, 44], but temperature dependent refractive index values of $\text{In}_x\text{Ga}_{1-x}\text{As}$ and $\text{InAs}_{1-y}\text{P}_y$ have not yet been reported. Also, it is necessary to compare properties measured from thin film and from bulk material in order to provide accurate information of the material.

1.2 Objective

The objective of this study is to investigate the electrical and optical properties of melt-grown bulk ternary $\text{In}_x\text{Ga}_{1-x}\text{As}$ and $\text{InAs}_{1-y}\text{P}_y$ alloys as functions of composition and temperature using various characterization methods such as Fourier Transform Infrared (FTIR) transmission spectrum, Hall-effect, photoluminescence (PL), and refractive index measurement techniques to determine relevant material parameters such as transmission cut-off wavelength, carrier concentration, mobility, bandgap energy, refractive index, and

composition homogeneity. It is aimed at a systematic investigation across a full composition range of indium and phosphorus mole fractions and at a temperature range from cryogenic temperature to above room temperature. This study aims to a better understanding of these relatively new bulk III-V ternary crystal properties.

1.3 Approach

Traditional characterization techniques such as Fourier transmission infrared spectroscopy, photoluminescence, and Hall-effect measurement methods were employed in this study. In addition, Electron Probe Micro Analyzer (EPMA) as well as infrared imagery was also used.

Specific goals of this investigation are:

- a. Determination of bandgap energies of bulk $\text{In}_x\text{Ga}_{1-x}\text{As}$ and $\text{In}_y\text{As}_{1-y}\text{P}_y$ as functions of composition and temperature using FTIR transmission spectra and PL spectra.
- b. Measurements of carrier concentration, mobility, and resistivity of melt-grown bulk $\text{In}_x\text{Ga}_{1-x}\text{As}$ and $\text{In}_y\text{As}_{1-y}\text{P}_y$ alloys as functions of composition and temperature using Hall-effect measurements.
- c. Refractive index measurements of the alloys as functions of composition, photon energy, and temperature using minimum deviation method and Michelson Fabry-Perot interferometers. Exploiting compositional homogeneity within the wafers using both EPMA and photoluminescence methods.

1.4 Dissertation Summary and Layout

In this dissertation, literature surveys are presented at the beginning as a part of the introduction. Relevant background theories are described in chapter 2. This is followed, by descriptions of measurement techniques used in this work, as well as details of the experiments and experimental layouts in chapter 3. Chapter 4 describes the first set of experimental results obtained from binary semiconductors. Chapters 5 and 6

contain experimental results and discussions. The discussions also include comparisons of the bulk and thin film properties, as well as comparisons among the results acquired using different characterization techniques.

Chapter 7 is the conclusions and future work including important results and lessons learned, followed by a brief recommendation for future work. A list of publications is given in Appendix A. Appendix B contains the operating procedures for the Hall-effect and PL measurements. Appendix C is a magnetic field correction for Hall-effect measurement based on the position of sample and the location of the Gauss meter.

2. Theory

2.1 Semiconductor Basics

Many inorganic semiconductors are found in crystalline form. In a single crystal, atoms have a regular geometric arrangement and periodicity as shown in Fig. 2.1 [45]. The electrical and optical properties of the crystal are determined from both the chemical composition and the arrangement of the atoms. Semiconductors can be elemental or compound. Elemental semiconductors consist of only one type of atom such as carbon (C), silicon (Si) and germanium (Ge). A compound semiconductor consists of two or more elements. Semiconductors are also classified as direct bandgap or indirect bandgap based on their bandgap properties.

Single crystal materials are further characterized by the atomic distances (the length of one side of the unit cell) between the atoms in their periodical arrangement, which are also called lattice constants. In cubic structures, the length of each side of the unit cells is the same, and thus they are characterized by one lattice constant. Hexagonal structures have two unique lattice constants to describe their structures. This parameter is important in crystal growth and device fabrication. The lattice constants of a substrate and a crystal that is grown on the substrate should be the same (or close) to minimize the formation of defects and imperfections during the growth process.

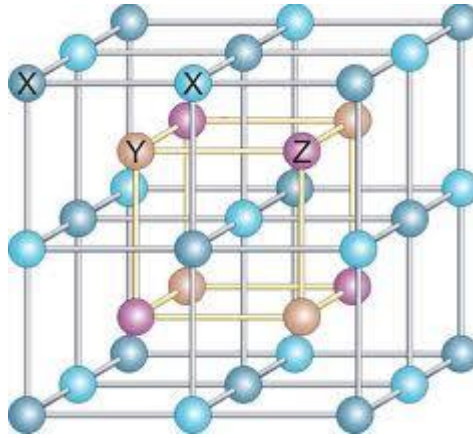


Figure 2.1. Crystal lattice structure.

2.2 Bulk III-V Ternary Crystal Growth

Growing high quality single crystalline semiconductors requires precise control over all aspects of the growth conditions [47], such as the temperature, composition, impurities in the source materials, vapor pressure, growth substrate, cooling rate, etc. In short, strict thermodynamic equilibrium conditions must be maintained throughout the entire growth process. This makes compound crystal growth difficult [47-51]. Because the stoichiometry (the correct chemical ratio of the compound's constituent elements) in a liquid or gas state must be maintained, the thermal parameters to obtain the right composition of solid crystal must also be controlled at the same time. This relationship is governed by a phase diagram. In developing new material, the phase diagram is unknown, therefore crystal growers have to use a pseudo phase diagram as shown in Fig. 2.2 [47], and determine optimized growth conditions through design of experiments. During these trials, crystal characterization is essential in order to guide the crystal grower toward optimum growth condition. Feedback from these characterizations results in the proper adjustment in crystal growth conditions.

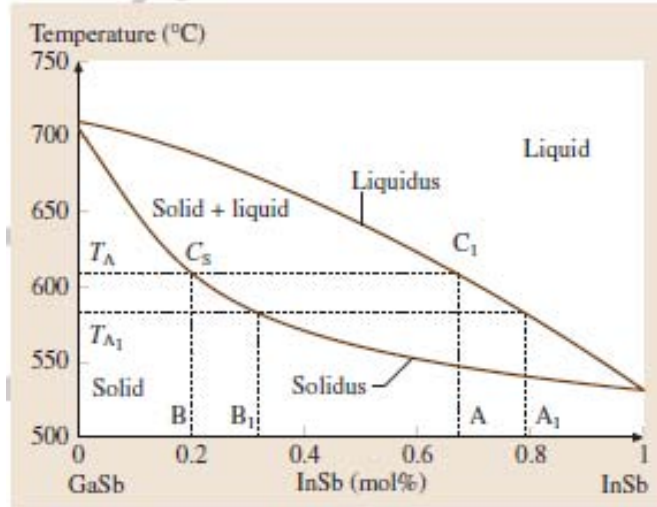


Figure 2.2. A schematic pseudobinary phase diagram of an III-V ternary compound (GaInSb).

Crystal growth methods are classified into two categories; epitaxial and melt. The first is epitaxy, which can be further classified to vapor-phase epitaxy (VPE), liquid phase epitaxy (LPE), and molecular beam epitaxy (MBE). It is a growth method of applying oriented single crystals with a controlled thickness over a substrate. This method provides good control over purity, doping, and thickness. It is extensively used in device manufacturing. To obtain high quality epitaxial layers, it is important that the substrate and the epitaxial layer are lattice matched. When the lattice constants do not match, stress and defects arise such as dislocations and vacancies as shown in Fig. 2.3 [52, 53]. The strength of stress increases linearly with the epitaxial layer thickness, limiting the maximum critical thickness that can be grown on a substrate. This is when the strain energy approaches the chemical energy value. Above this thickness, dislocations propagate upward, multiplying as they go and forming threading dislocations, causing adverse effects on the electrical and optical properties.

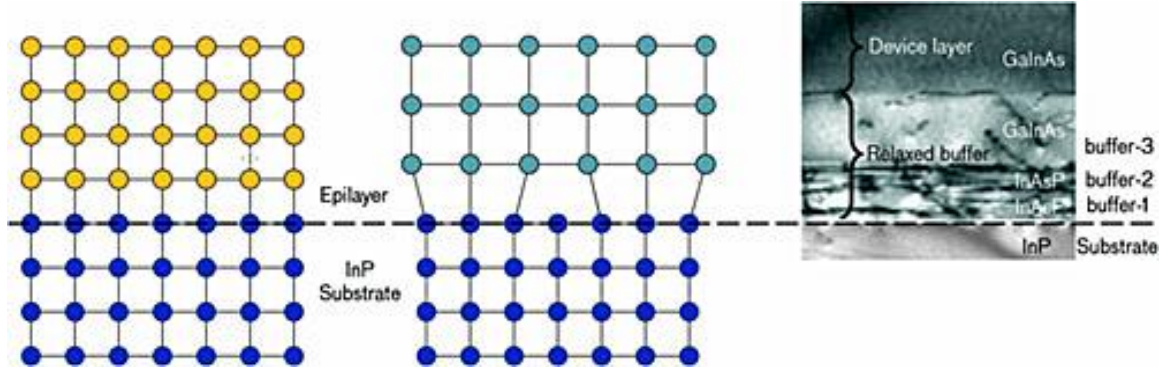


Figure 2.3. Schematic lattice constant match and mismatch effects on the quality of crystal.

Bulk crystal growth typically uses the Czochralski Method (melt). In this method, a seed crystal is placed in contact with the same material in liquid form and slowly rotated as it is retracted from the liquid solution. A modified version of this method is called the Bridgman-Stockbarger method [47]. This method can be implemented in either a vertical or horizontal system. This principle is based on directional solidification by translating a molten charge (melt) from the hot to cold zone of the furnace. A vertical Bridgman growth of $\text{Ga}_{1-x}\text{In}_x\text{Sb}$ system is shown in Fig. 2.4 [47].

The first step of bulk ternary crystal growth is to generate a single crystalline seed of a specific ternary composition starting from a binary seed. During this process, the melt composition needs to be continuously changed for grading the alloy composition of the crystal. The second step is to grow a homogeneous crystal of a specific composition. For this step, the melt source ratio needs to be maintained as a constant throughout the growth. For both of these steps, precise control over the solute feeding process and melt composition is necessary. There are other techniques and conditions in controlling the growth parameters to ensure a high quality crystal. These conditions include [47] usage of melt encapsulation, vapor pressure control for group V volatile species, crucible

material, and post growth crystal annealing. Post growth cooling cycles are equally important. Fast cooling rates can result in thermal strain that results in a cracking of the wafers during processing.

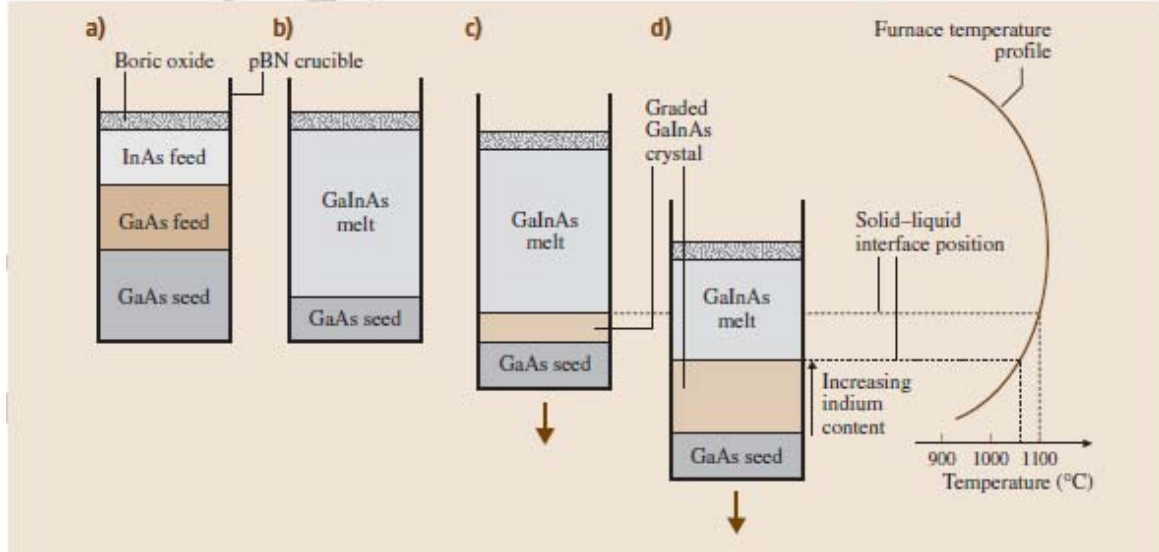


Figure 2.4. Vertical Bridgman growth of $\text{Ga}_{1-x}\text{In}_x\text{Sb}$ system.

2.3 Band Structure and Bandgap Energy

Band theory of solids can be used to better understand how crystal structure and residing defects can affect the fundamental properties of a semiconductor. The simplest theory in solid state physics is the free electron model. This model is based on the assumption that conduction band electrons are free to move around. However, they are confined in semiconductor lattice structures (i.e. the periodic potential which arises from the lattice arrangement of the host atoms). Using the classical quantum mechanics “particle in a box” model, one can solve Schrödinger’s equation in the crystal lattice, and the solution of the wave function gives discrete electronic energy levels [54]. Extending this simplified model to an infinite number of lattice structures (similar to infinite number of quantum wells

with periodic potential V_0), the wave functions of the electrons interact and form the discrete energy levels of the individual atoms called the energy band structure. A typical band structure is shown in Fig. 2.5 [55]. In momentum (k) space, the lower energy state of valence band (E_v) is at the bottom, and the conduction band (E_c) is on the top. The energy difference between E_v and E_c at $k = 0$ is called bandgap energy (E_g). Near $k = 0$ the energy band can be approximately considered as parabolic, thus $E_v = -\frac{\hbar^2 k^2}{2m_h}$,

$$E_c = E_g + \frac{\hbar^2 k^2}{2m_e}, \text{ where } m_h \text{ and } m_e \text{ are the effective masses of holes and electrons}$$

respectively, and \hbar is the reduced Plank's constant.

The magnitude of E_g is also an important material parameter. In general, materials are classified into three categories based on the magnitude of E_g .

Conductor	$E_g = 0 \text{ eV}$
Insulator	$E_g > 6 \text{ eV}$
Semiconductor	$0.1 \text{ eV} < E_g < 6 \text{ eV}$

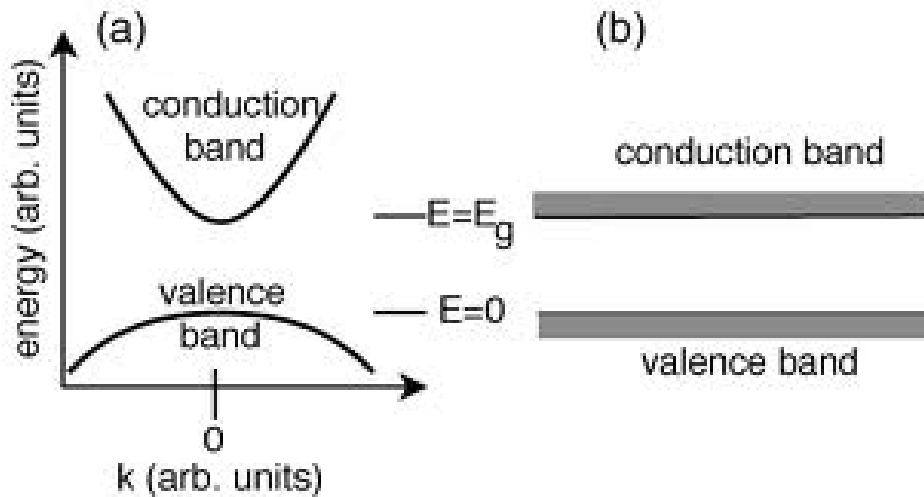


Figure 2.5. A typical bandgap structure.

Semiconductors act like an insulator at low temperatures. However, as the temperature increases, a significant number of electrons are thermally excited from the states near the top of the valence band to those near the bottom of the lowest empty conduction band because the width of the forbidden energy gap is smaller. This creates partially filled bands and allows conduction to occur. In general, semiconductor's E_g is less than ~ 4 eV. Throughout this work, investigation is limited to infrared semiconductors, i.e., $E_g < 1.5$ eV.

The density of electrons in the upper band, N_c , (or holes in the lower band, N_h) is closely related to the Fermi-Dirac distribution,

$$f(E) = \frac{1}{1 + \exp\left(\frac{E - E_F}{k_B T}\right)}. \quad (2.1)$$

Here $f(E)$ is the probability of occupying energy states, k_B is Boltzmann constant, and T is the temperature (K). E_F is the Fermi energy, which usually lies in the middle of the bandgap for intrinsic semiconductors. The density of states, g_c , at the conduction band is expressed as

$$g_c(E) = \frac{(2m_e)^{3/2}}{2\pi^2\hbar^3} \sqrt{E - E_c}, \quad (2.2)$$

where $E > E_g$, and m_e is the effective mass of the upper conduction band electron. E_c is the energy at the bottom of the conduction band. Below the bandgap energy, where $E < E_g$, the density of state is proportional to following relationship:

$$g(E) \propto e^{\frac{E-E_g}{k_B T}}, \quad (2.3)$$

where T is the temperature and k_B is the Boltzmann constant.

Motion of electrons is only allowed in the valance and conduction bands. When a semiconductor is under optical radiation, if the photon energy is less than the semiconductor's bandgap energy, the photon will pass through so that light transmits through the semiconductor. When the photon energy is larger than the bandgap energy, this photon will be absorbed by the semiconductor where it excites an electron from the valance band to its conduction band, leaving behind a positively charged state. Actually the absence of the electron is referred to as a hole. The hole is not an actual particle, but it behaves as one and has many similar properties of the electron.

According to Beer-Lamber's law, the radiation will exponentially decay after propagating through a media. This relationship can be expressed as

$$T = \frac{I}{I_0} = e^{-\alpha d}, \quad (2.4)$$

where I_0 is the incident photon intensity, and I is the transmitted intensity. T is the transmission (%), α is the absorption coefficient of the material, and d is the thickness of the sample.

For direct bandgap materials, the valance band maximum and conduction band minimum occur at the same point in k -space as shown in Fig. 2.6 [46]. For an indirect bandgap material, the E_v maximum and the E_c minimum do not occur at the same point in k -space. Therefore, for an optical transition, it would require additional conservation of momentum of phonon besides the energy requirement. Because of this, direct bandgap

material such as InAs, GaAs, InP, InGaAs and InAsP are more desirable in making fast and efficient light sources. On the other hand, some indirect bandgap materials such as Si, Ge, and diamond are good photo detector candidates.

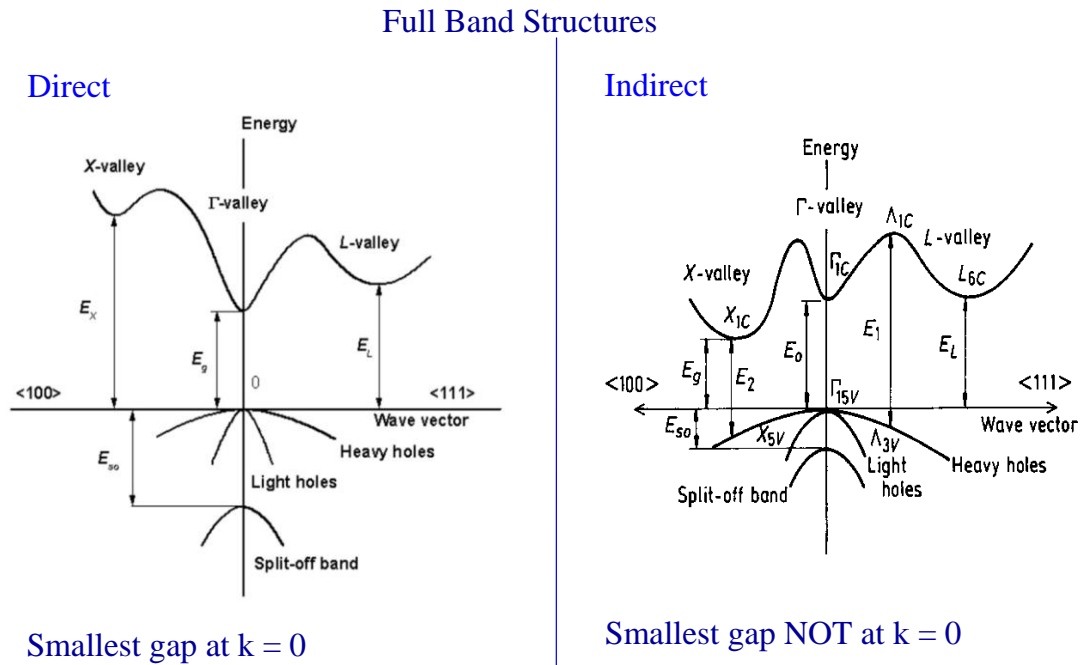


Figure 2.6. Illustration of band structures of semiconductor materials.

2.4 Temperature Effects on Semiconductors

At temperature $T = 0$ K, electrons occupy their lowest energy state. The valence band is full but the conduction band is completely empty. As the temperature is increased, some electrons will gain sufficient thermal energy to move to the conduction band and contribute to conduction. As the temperature further increases, the lattice of the semiconductor material expands and the oscillations of the atoms near their equilibrium location in the lattice will increase. This change would narrow the bandgap by changing

the population of electrons and holes in the conduction band and the valence band. In addition, the increased motion of the atoms broadens the energy levels.

This temperature change results in a change of the material properties. For instance, at temperatures much lower than the Debye temperature, the energy gap varies proportionately to the square of the temperature. When the temperature is much above the Debye temperature, the energy gap varies linearly with the temperature. The observed temperature dependent E_g agrees with the empirical Varshni relationship [56]:

$$E_g(T) = E_g(0) - \frac{\alpha T^2}{T + \beta}, \quad (2.5)$$

where $E_g(0)$ is the value of the energy gap at 0 K, also called the absolute bandgap energy, and α and β are constants (Varshni coefficients). Note that the value of β is in the range of the Debye temperature, but these two coefficients are not independent.

Temperature dependent refractive index is affected by the change of bandgap energy [57] through the relation

$$\frac{dn}{dE_g} = - \left\{ \frac{\sqrt{6}}{\pi} \frac{e^2}{(4\pi\epsilon_0)\hbar} \frac{1}{\sqrt{E_p}} \sqrt{\frac{m_e}{E_p}} \right\} \frac{1}{n_0 E_g} g\left(\frac{\hbar\omega}{E_g}\right), \quad (2.6)$$

where $g(x) = \frac{\pi}{4} \text{Re} \left\{ \frac{\sqrt{1-x} + \sqrt{1+x} - 2\sqrt{1-x}\sqrt{1+x}}{x^2 \sqrt{1-x}\sqrt{1+x}} \right\}$, m_e is the electron mass, n_0 is the

refractive index at room temperature and E_p is the Kane energy.

For infrared materials, $E_p \approx \frac{3E_g}{4\left(\frac{m_c}{m_e}\right)}$, where $\frac{m_c}{m_e}$ is effective electron mass (m_c is the

reduced mass). E_p is almost a constant for narrow banggap material, and roughly $E_p=11.24$ eV for InAs.

Using the chain rule, one can write:

$$\frac{dn}{dT} = \frac{dn}{dE_g} \frac{dE_g}{dT}. \quad (2.7)$$

Thus, the temperature dependent refractive index can be obtained from the known temperature dependent bandgap energy and dn/dE_g .

2.5 Semiconductor Impurities

A perfect crystal is something that only exists conceptually and can rarely be found in nature. Semiconductors form closed valance shells through covalent bonding with their nearest neighbors. When impure atoms from neighboring columns in the periodic table occupy a lattice site in the host crystal, they attempt to form all the bonds the crystal's atoms would have created. Sometimes the impure atoms will complete all the bonds and have one or more extra electrons, such as the case when silicon ions (column IV) replace Ga (column III) atoms in an InAsP crystal. These “extra” electrons are then free to modify the conduction. In this case, impurity ions are referred to as donors. On the other hand, impurity ions may not have enough electrons to complete all the bonds (e.g., Zn on an As site) and thus create holes that are readily available to participate in the conduction in the valance band. Impurity ions of this type are called

acceptors. The existence of impurities and the impurity level in semiconductor will greatly affect both the semiconductor's electrical and optical properties.

When the impure atom is embedded with the pure semiconductor, the binding energy is significantly reduced. The binding energy of an electron in an impure atom is much smaller compared to the bandgap. This makes it easier to thermally ionize the donor electrons to produce conduction. For a semiconductor's electrical properties, if the impurities exist in a controlled manner, then the electrical conductivity (σ) can be manipulated in an accurate and reliable way, which is governed through equation 2.8.

$$\sigma = e(n\mu_n + p\mu_p). \quad (2.8)$$

Where e is the charge of the electron, n and p are the electron and hole carrier concentrations, and μ_n and μ_p represent the mobility for the electrons and holes, respectively. Intentionally introduced impurities can benefit the conduction up to the critical doping density, at which the doping density becomes so large that the impure atoms are separated by less than the Bohr radius. At this point the material acts like a metal.

Heavy doping can result in impure band formation and cause band tailing or band filling. Spatial distribution of impure atoms is generally random, causing random fluctuations at the band edges (known as band tailing). As the impurity concentration grows, free carriers begin to occupy states above the bottom of the conduction band. This is known as band filling.

3. Characterization Techniques and Experimental Setups

In this work, both electrical and optical properties of infrared semiconductor materials were investigated using various characterization techniques. The detailed characterization methods and experiments are described in this chapter.

The optical characterizations were performed in the infrared materials Laboratory at Wright-Patterson Air Force Base (WPAFB) in Ohio. Electrical characterizations were performed in the Semiconductor Laboratory of the Engineering Physics Department, Air force Institute of Technology, Bldg 644 at WPAFB.

3.1 Electrical Characterization

The electrical characterization is based on the Hall-effect/sheet-resistivity measurement. This method provides quantitative information for semiconductor conductivity type (n- or p-type), carrier concentration, mobility, and resistivity. These parameters are very useful in semiconductor device designs and applications.

3.1.1 Hall-effect Theory

The Hall-effect theory was discovered in 1879 by Edwin H. Hall, an American physicist. He discovered that a small transverse voltage was generated across a thin metal strip in the presence of an orthogonal magnetic field. The discovery of this transverse voltage (the Hall Voltage) enabled the independent calculation of the mobility and the carrier concentration of the material, which was only accomplished up to that time through difficult measurements. In 1958, van der Pauw developed a theory which could be shown experimentally in an easier manner than the original Hall-effect method. He showed that the shape of the measuring sample was not a factor and only required that

the sample be simply connected and exhibit highly ohmic point contacts on the periphery of the material [58]. Similar discussions can also be found in Moore's dissertation [59].

According to the Hall-effect theory, electrons moving in a specimen find themselves subject to the Lorentz Force in the presence of a perpendicular magnetic field. Hall-effect measurements are conducted by placing a sample in a magnetic field that is orthogonal to its surface as illustrated in Fig. 3.1. For the van der Pauw method, a current is applied to the material so that the charged carriers move in the x direction. The moving charges induce an internal electric field in the material, which deflects the charges toward the edges of the material. Positively charged particles (holes) move to one edge, and the negatively charged particles (electrons) move to the opposite edge. This particle movement is the result of the charge carriers being subject to the Lorentz Force, which is normal to the magnetic field. The Lorentz Force is given by

$$\vec{F}_L = q \vec{E} + \vec{v} \times \vec{B} , \quad (3.1)$$

where q is the charge of the particle, \vec{E} is the electric field, \vec{v} is the velocity of the electrons, and \vec{B} is the magnetic field. If one type of carrier is dominant, this shift causes a buildup of unequal surface charge which creates a potential difference across the sample surface, the Hall voltage.

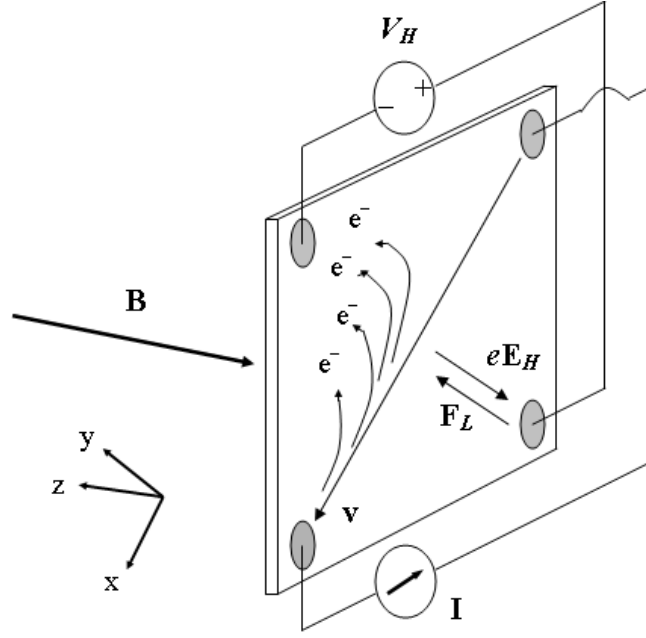


Figure 3.1. A schematic diagram illustrating of the van der Pauw Hall-effect.

This generated transverse voltage will therefore have a different sign for n and p-type materials as shown in Fig. 3.1.

The Hall-effect can be described much more easily with the rod-shaped specimen, and the following description applies to rod-shaped specimen. Solving the cross product in equation 3.1, the Lorentz Force equation becomes

$$F_y = qE_y + qv_x B_z. \quad (3.2)$$

The system will strive for equilibrium and therefore the Hall Voltage will grow until it becomes equal to the Lorentz Force. When this occurs, F_y is zero and equation 3.2 can be simplified to

$$E_y = -v_x B_z. \quad (3.3)$$

The current density which is defined in equation 3.4 can be solved for the velocity and substituted into the electric field equation 3.3, rendering the equation to experimentally measurable quantities.

$$I_x = nqv_x r_H \rightarrow v_x = \frac{I_x}{nqr_H}. \quad (3.4)$$

The Hall factor is represented by r_H and denotes the Hall to drift mobility ratio, which is usually approximated to be 1, but can vary between 1 and 2. This estimation causes Hall Effect measurements to often underestimate the values of the carrier concentrations. The substitution of v_x into equation 3.3 yields an equation for the transverse electric field in terms of the Hall coefficient, R_H , applied current density, J_x , and applied magnetic field, B_z . That is, it is given by

$$E_y = \frac{I_x B_z}{nqr_H} = R_H J_x B_z. \quad (3.5)$$

The above equation is then used to define the Hall voltage, V_H . The Hall voltage is the product of the generated electric field and the width of the sample, w .

$$V_H = E_y w = R_H J_x B_z w. \quad (3.6)$$

The Hall voltage, being a measurable quantity, is used to calculate the Hall coefficient. Equation 3.6 can be solved Hall coefficient

$$R_H = \frac{V_H}{J_x B_z w}. \quad (3.7)$$

The magnitude of the Hall voltage is inversely proportional to the carrier concentration and the sign of this voltage indicates the dominant carrier type. For electron conductivity, the Hall coefficient is negative, and the coefficient is positive for hole conduction. The sheet carrier concentration, N_s , and mobility, μ_H can be calculated using following relations:

$$N_s = \frac{r_H}{qR_H} \quad \text{and} \quad \mu_H = \frac{R_H}{\rho_s}. \quad (3.8)$$

Temperature-dependent Hall (TDH) measurements provide carrier concentrations and mobility values as a function of temperature. At low temperatures, even the shallow impurities could freeze, leaving the material highly resistive. If the material is highly degenerate, TDH measurements will reveal the degenerate layer at low temperatures via the temperature independent mobility and carrier concentration.

3.1.2 Hall-effect Measurement System

The Hall-effect measurements are made with an automated Lake Shore 7505 system using the standard van der Pauw method. A diagram of the system is provided in Fig. 3.2. The samples are placed on Janis vacuum heads designed for low (10-320 K) and high temperature (300-700 K) measurements which are placed between two coil magnets that are capable of producing up to a 5 kG magnetic field. All measurement is done in a 5 kG field. Current is supplied to the sample with a Keithley 220 current source and the generated Hall voltage is measured using a Keithley 2182 nanovoltmeter. Lake Shore Hall program version 3.3 automates the process and records the resistivity and Hall data.

LakeShore 7505 Hall Effect Measurement System

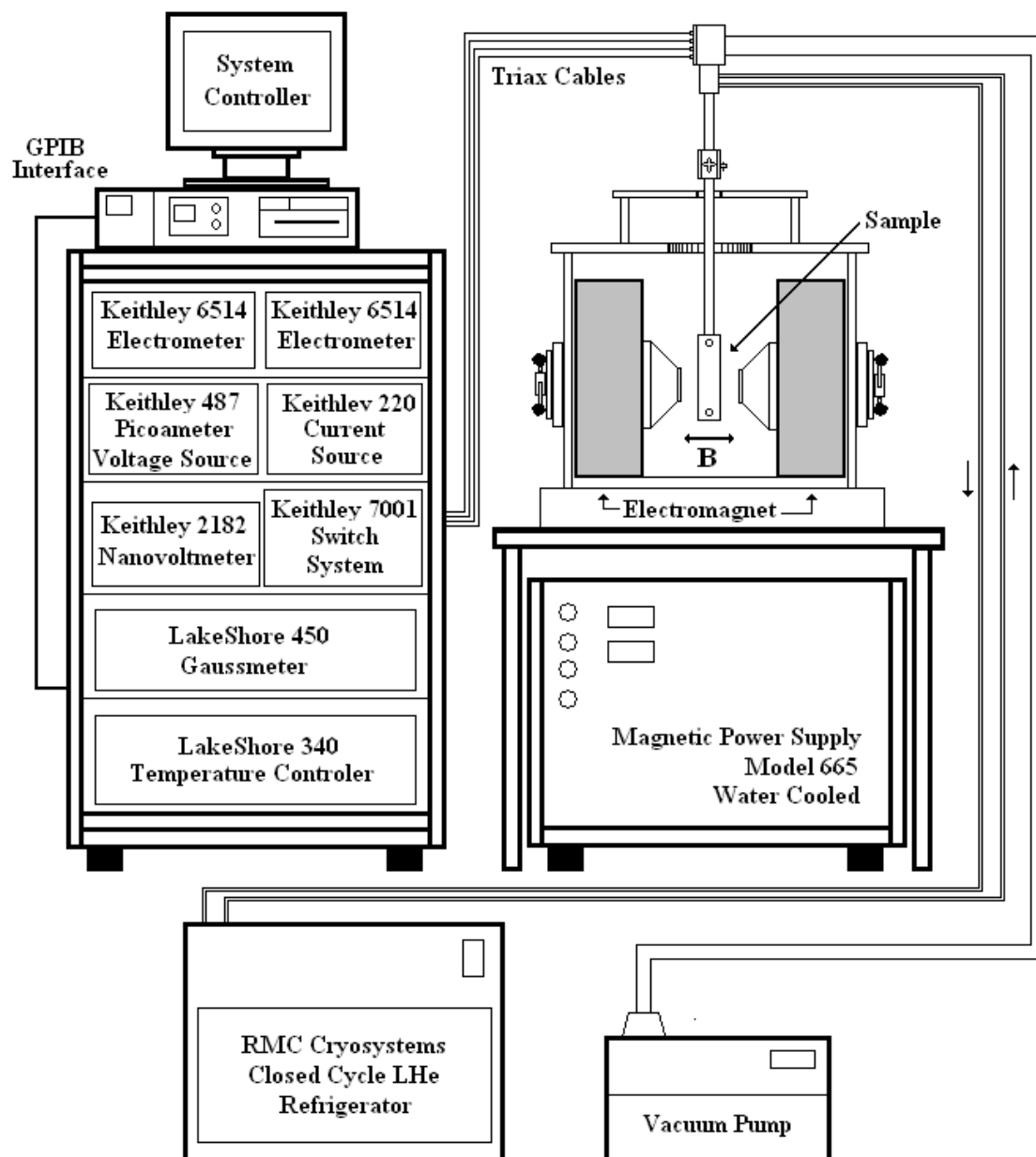


Figure 3.2. A schematic diagram of the LakeShore 7505 automated Hall measurement system.

Hall Measurements provide only average carrier concentration and mobility values over the entire conducting thickness. A total of 8 current-voltage pair measurements are averaged to calculate the sheet resistivity. Four current-voltage pair measurements are taken under forward and reverse magnetic fields, and are averaged to calculate the Hall coefficient. Temperature-dependent Hall-effect measurements were made at 5 kG using the standard van der Pauw technique at temperatures ranging from 10 to 300 K. Ohmic contacts were placed on the periphery of the sample using indium.

3.2 Optical Characterization

There are three methods used primarily for optical characterizations in this study. They are transmission spectrum, photoluminescence (PL), and refractive index measurements. Other methods such as infrared imagery and micro probe wavelength dispersing methods were also employed in this study. Optical measurements were conducted as functions of temperature and sample composition.

3.2.1 Fourier Transform Infrared Spectroscopy

FTIR spectroscopy [60] is a technique for collecting infrared spectra. A transmission spectrum gives the most fundamental optical property of the sample: transmission. Other optical properties such as the absorption coefficient, bandgap energy, temperature dependent bandgap energy (dE_g/dT), and thermal optical coefficient (dn/dT) can also be extracted from the transmission spectra. The dn/dT can also be independently measured using the minimum deviation method and hence this value can be compared with the predicted dn/dT from transmission spectra. Since the bandgap

energy can also be extracted from the PL measurement, the value can be compared with that obtained from the transmission spectrum.

A Perkin Elmer Spectrum GX was used to measure the transmission spectra of the samples. The Perkin Elmer Spectrum GX is a single-beam Michelson interferometer-based FTIR spectrometer, and was allowed in transmission mode. The system is configured with a mid-infrared (MIR) or near-infrared (NIR) single source. Most frequently for InGaAs and InAsP samples, MIR source and MIR beam splitters were selected. Deuterated Triglycine Sulfate (DTGS) detector allowed for a detection range of 7000 to 50 cm^{-1} with a maximum resolution of 0.3 cm^{-1} . It is fully automated and computer controlled. A schematic layout of the NIR mode of Perkin Elmer Spectrum GX FTIR system is shown in Fig. 3.3. It includes a built-in 35 W tungsten halogen illuminator, a motorized stage, and a CCD video camera. The heart of the optical design is the Michelson interferometer shown in Fig. 3.3, which provides the measurement with stability, reliability and sensitivity. A single scan measurement is fast, because information of all frequencies is collected simultaneously. In this work, the wavelength for MIR is ranging from 0.6 to 25 μm . Most samples studied were at a temperature range of 80 – 400 K. Samples are grouped by $\text{In}_x\text{Ga}_{1-x}\text{As}$ and $\text{InAs}_{1-y}\text{P}_y$ with different compositions of x and y.

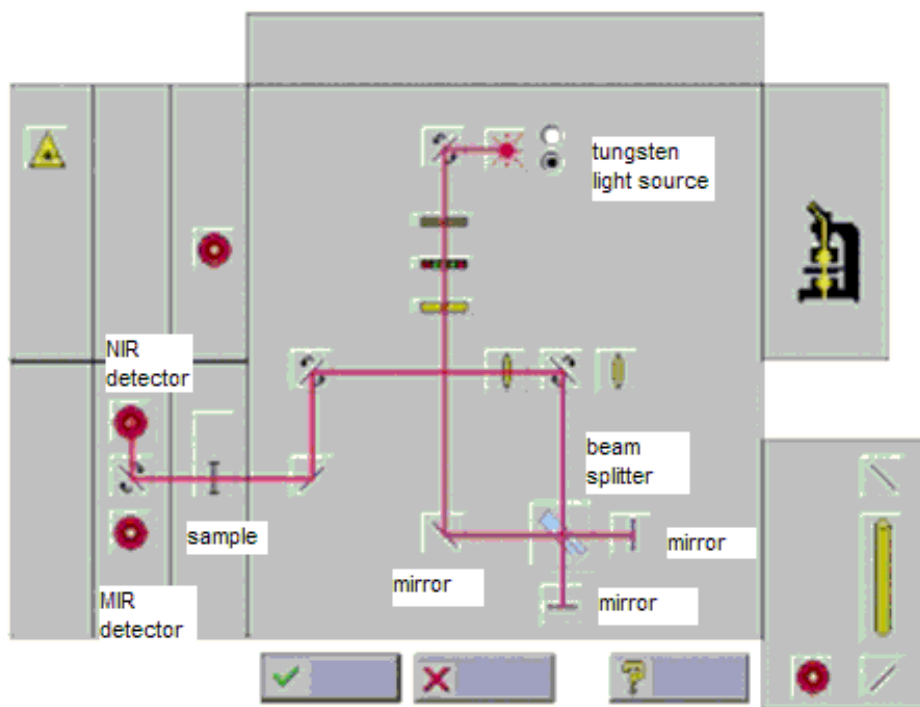


Figure 3.3. A schematic layout of Perkin Elmer Spectrum GX FTIR system with the PC interface.

3.2.2 Photoluminescence Measurement

A semiconductor material will emit photons as well as thermal radiation when it is radiated with a sufficient energy such as a laser. There are two types of luminescence that semiconductors exhibit: fluorescence and phosphorescence. Fluorescence is the emission of photons due to a direct transition from an excited state to a ground state, while phosphorescence utilizes intermediate transitions so that the luminescence persists after the excitation source is terminated. Materials that have this type of luminescence are generally referred to as phosphors [61]. Semiconductors in this study exhibit fluorescence. Similar discussions on the PL measurement can also be found in Fellow's dissertation [62].

PL can be a powerful semiconductor characterization tool because it provides direct observation of the energy levels that exist in the material. This provides an excellent tool to appraise the quality of a crystal. Luminescence is a combination of several types of electron-hole pair recombination such as excited state electrons (e) with ground state holes (h) in semiconductors. The electrons and holes also relax to equilibrium through a succession of interactions with defect and impurity levels within the bandgap, and they eventually leads to recombination. The wavelength of the emitted luminescence is given by $h\nu = h\left(\frac{c}{\lambda}\right) = \Delta E = E_i - E_f$, where h is the Plank's constant, ν is the frequency, c is the speed of light, λ is the wavelength, and ΔE is the initial energy (E_i) minus the final energy (E_f) in the transition.

Possible transitions include transitions between the conduction band to the valence band, and transitions between levels within the bandgap induced by impurities and defects, such as donor and acceptor levels. The most common radiative transitions are illustrated in Fig. 3.4.

Luminescence spectra can be collected for all radiative transitions that occur between two energy levels. They are: the band-to-band transition (a), the free exciton transition (b), the neutral donor and free hole recombination (c), a free electron transitioning to a neutral shallow acceptor (d), and the donor-acceptor transitions for shallow (e) and deep states (f), which are demonstrated in Fig. 3.4.

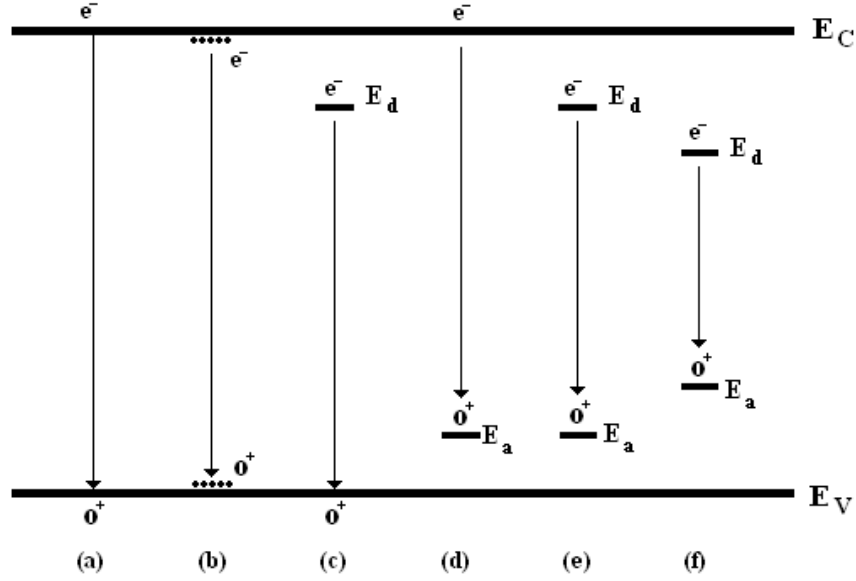


Figure 3.4. Common radiative transitions take place in semiconductors. (a) band-to-band, (b) free exciton, (c) neutral donor and free hole recombination, (d) a free electron transitioning to a neutral shallow acceptor, and (e) (f) donor-acceptor transitions for shallow and deep states, respectively.

Among all of the above transitions, the band-to-band (B-B) transition, labeled (a), is generally dominant at room temperature. The energy of this transition is given by

$$h\nu = E_c - E_v = E_g, \quad (3.9)$$

where E_c is the conduction band minimum, E_v is the valence band maximum, and E_g is the energy gap. The free exciton (FX) transition, labeled as (b), is common in pure semiconductors, and the electron bound to the hole through Coulombic force recombines. The energy of this transition is the bandgap energy minus the binding energy of the two particles (electron and hole), and is shown in equation 3.10.

$$h\nu = E_g - m_r^* \frac{q^4}{2\kappa\hbar^2} \quad (3.10)$$

where m_r^* is the reduced effective mass of the exciton, q is the charge, and κ is equal to $4\pi\epsilon_r$, where ϵ_r is the relative dielectric constant. Transition (c) shows the transition from an electron on a neutral donor recombining with a free hole (D^0, h), while transition (d) illustrates the recombination of a free electron in the conduction band and a hole on a shallow neutral acceptor (e, A^0). The energies for these transitions are given by

$$h\nu = E_g - E_{d,a}, \quad (3.11)$$

where E_d is a donor energy level and E_a is an acceptor energy level. The last two transitions in the diagram are extremely important and are the same transition; only the depths of the acceptor and the donor levels change. They are the donor-acceptor pair (DAP) transitions, where an electron on a shallow donor recombines with a hole on a shallow neutral acceptor, or as seen in (f) where an electron in a deep donor recombines with a hole in the deep acceptor. The energy of this type of transition is given by

$$h\nu = E_g - E_d - E_a + \frac{q^2}{\kappa r}, \quad (3.12)$$

where r is the separation distance between the donor and the acceptor. The last term in the equation represents the electrostatic energy gained as the transition is complete. The DAP transitions can have a broad spectrum due to the wide number of assumed discrete values r . This transition provides a good means for studying the interband transitions that occur in the semiconductor material. The FX transition dominates at low temperatures for most pure semiconductor materials exhibiting strong exciton peaks. The DAP peak can serve as a measure of the compensation level of the material. A material which is fairly

compensated may exhibit strong DAP peaks and be fairly resistive with a high level of shallow donor and acceptor concentrations.

The relative intensity of the transition feature can give insight into the electrical and structural properties of the semiconductor material. Deep defect levels in the bandgap region can trap electrons and prohibit luminescence.

3.2.2.1 Photoluminescence Experiment

The PL experiment setup is shown in Fig. 3.5, where the excitation laser is a Spectra-Physics BeamLok 2085-20 multi-line continuous wave (CW) argon ion laser with a principle wavelength of 514.5 nm. The laser beam was attenuated using an optical neutral density (ND) filter, and passed through an optical chopper running at a duty cycle of approximately 170 Hz. The laser beam size is about 3 mm in diameter, and was guided by mirrors to the sample surface. Samples were mounted on a cold finger connected to the Helitran using Crycon thermal grease to create a heat sink.

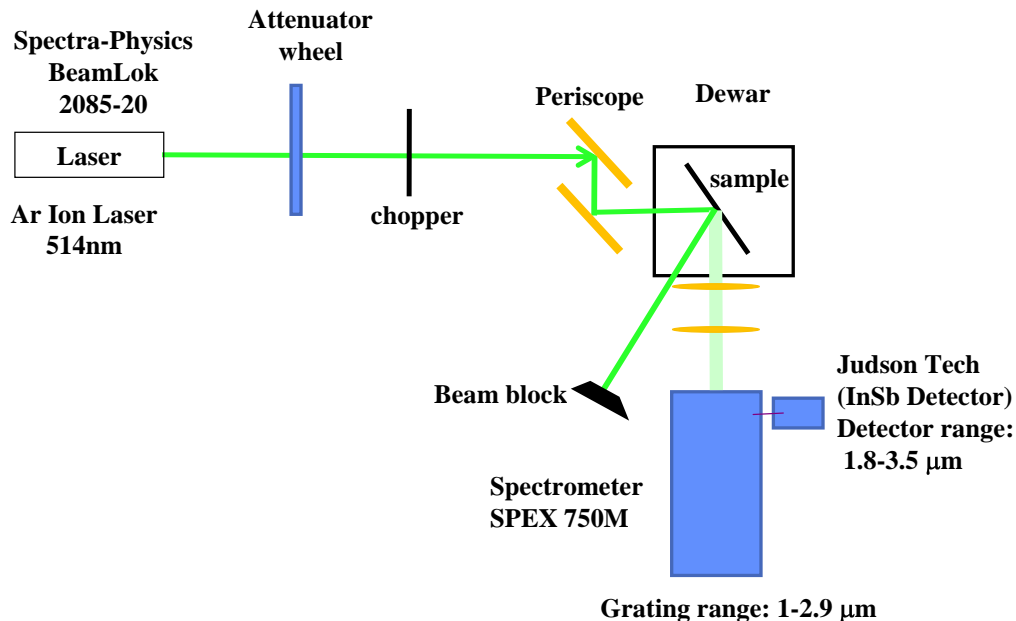


Figure 3.5. Experimental setup for the PL measurement

After the vacuum pump reaches approximately 20 milliTorr, a valve was opened to allow evaporated liquid helium gas to cool down the sample to approximately 10 K. Photoluminescence is generated on the sample surface when it is irradiated by the laser. Two CaF_2 lenses were used. The first lens with a focal length of 10 cm collects the emissions from the sample surface and the second lens with a focal length of 30 cm focuses the photoluminescence into the monochromator slit of the spectrometer entrance. The path between sample and the monochromator was covered by a tube and purged with high-purity dry nitrogen in order to avoid atmospheric absorption. PL signals were measured using a liquid nitrogen cooled J10D InSb detector from Teledyne Judson Technologies. The detector was operated with a 12 V bias. Depending on the wavelength range of the emissions, an SP35 cold filter was used to increase the signal-to-noise ratio by blocking background IR radiation outside of the 1.7 – 3.5 μm range. The PL signal

was measured using a Stanford Research SR 850 Lock-In amplifier synchronized to the optical chopper. These signals were recorded on a computer using SPEX software for analysis. PL studies were carried out as functions of laser power, sample temperature, composition and location. The lowest temperature is approximately 10 K, and the highest temperature reaches 295 K. The laser power range is 100-500 mW. Three to five locations per sample were investigated. The samples used in these PL studies are listed in table 3.1.

Table 3.1. List of samples used in the PL experiments and their composition

Sample name of $\text{In}_x\text{Ga}_{1-x}\text{As}$	Composition x^*	Sample name of $\text{InAs}_{1-y}\text{P}_y$	Composition y^*
InAs WT 524-10	1	IAP 040709	0.19
IGA 061206-6	0.99	IAP 101807-11	0.24
IGA 052406-4	0.93	IAP 31407-8	0.34
IGA 052406-2	0.91	IAP 022308 b3	0.41
IGA 052406-1	0.82		
IGA 041506-1	0.75		

*Composition is measured using CAMECA SX 100 micro probe analyzer at AFRX/RXB, building 655, area B, WPAFB, Ohio

3.3 Refractive Index

3.3.1 Prism Based Measurements Using Minimum Deviation Method

The minimum deviation method is one of the most accurate methods in measuring refractive indices. In this method, samples are required to be cut into a prism shape, and the light is dispersed when it enters the prism as shown in Fig. 3.6 (a). By varying the incident light angle (θ_{1i}), the corresponding deviation angle (δ) changes accordingly as shown in Fig. 3.6 (b). From this curve, one can identify the minimum deviation angle.

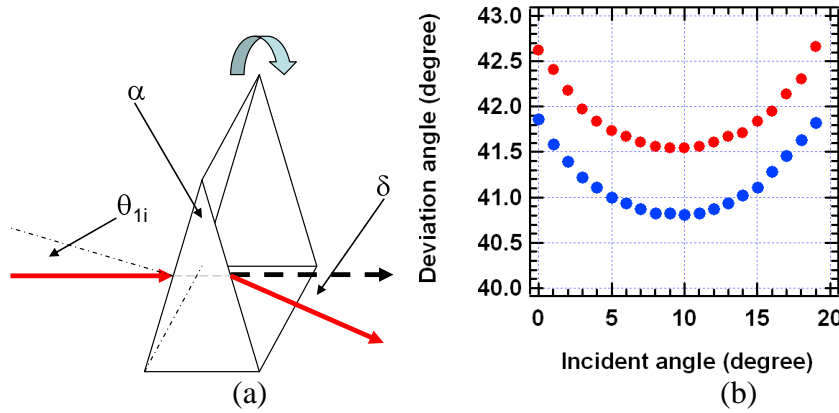


Figure 3.6. (a) Illustration of a ray of light dispersed through a prism, and (b) deviation angle vs. incident angle. Red data points are measured at 295 K and blue at 100 K with an InP prism at 4.6 μm .

From the obtained minimum deviation angle (δ_m) and known prism angle α , the refractive index can be calculated using the following relationship:

$$n = \frac{\sin[(\delta_m + \alpha) / 2]}{\sin \frac{\alpha}{2}}. \quad (3.13)$$

In this minimum deviation method, a prism shaped $\text{InAs}_{1-y}\text{P}_y$ sample is placed in a cryostat. Sample temperature is controlled by an Omega temperature controller with a temperature range from 77 K to 300 K. The temperature-dependent refractive index, $n(T)$, as well as dn/dT can be measured. Several laser sources having wavelengths of 3.39 μm , 4.6 μm , and 10.6 μm are used. The prism has dimensions as shown in Fig. 3.7 (a). The experimental setup for refractive index measurement is shown in Fig. 3.7 (b). The sample is mounted on a rotational stage having resolution of 0.001° . Distance, d , is determined by calibration on a reference sample and of CaF_2 . L is the location where the detector has the highest intensity for each incident angle. The deviation angle (δ) is given by $\tan^{-1}(L/d)$.

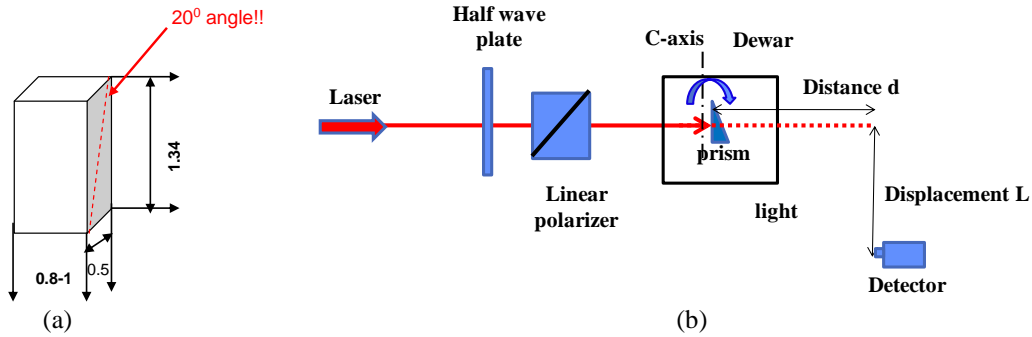


Figure 3.7. (a) Prism dimensions; (b) Minimum deviation method experimental layout.

3.3.2 Wafer Based Measurement Using Michelson and Fabry-Perot Interferometer

Both Michelson and Fabry-Perot interferometers were used to measure the optical path length (OPL) for wafer shaped samples [63-65].

$$\text{OPL} = nd, \quad (3.14)$$

where n is refractive index, d is the sample thickness. Refractive index (n) can be determined if d is known, and vice versa. However, it is difficult to measure an accurate thickness at low temperature and thus difficult to determine n at low temperatures. When combining the two methods (Michelson and Fabry-Perot interferometers), n and d can be decoupled, enabling determination of n and d precisely at any temperature. The schematic layout is shown in Fig. 3.8.

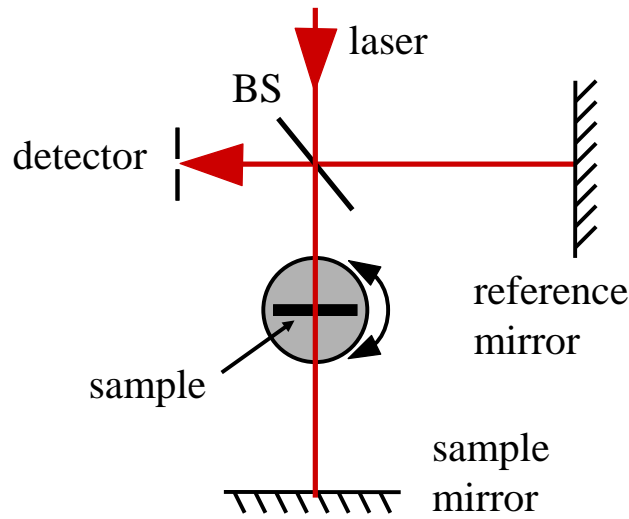
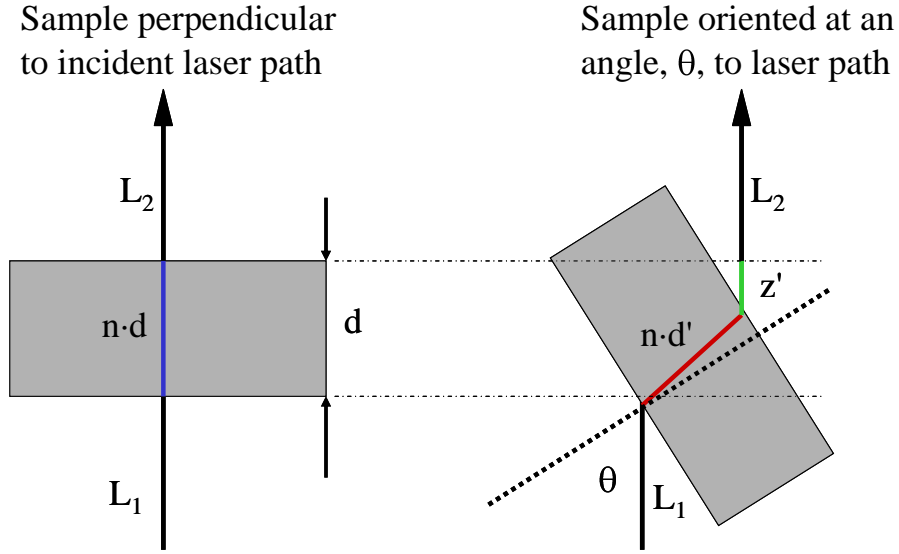


Figure 3.8. Schematic layout of the Michelson and Fabry Perot interferometers.

A wafer shape sample is placed in a cryostat, which is able to control over a temperature range of 100 – 295 K. A rotation stage is used to rotate the sample. The optical path changes as the sample is rotated as shown in Fig. 3.9. That is, the optical length changes from $(L_1 + nd + L_2)$ to $(L_1 + nd'(\theta) + z'(\theta) + L_2)$, where θ is the rotation angle.



$$\text{Optical path difference} = (nd' + z') - nd$$

Figure 3.9. Illustration of optical path nd changing with rotating angle θ

In case of Michelson interferometer, this optical length change in sample arm affects the intensity reading at a detector, where two electric fields combine. One is the laser beam reflected from the reference mirror which is a constant, and the other is the laser beam reflected from the sample mirror, which depends on rotation angle. These combined two electrical fields at a detector can be expressed as:

$$E_D = A_s \exp \left[\frac{i4\pi d}{\lambda} \sqrt{n^2 - \sin^2 \theta} + 1 - \cos \theta + \phi_s \right] + A_r \exp i\phi_r . \quad (3.15)$$

The intensity read by a detector is the modulus square of the electric field, thus the intensity received by the detector is:

$$I_D = A_r^2 + A_s^2 + 2A_r A_s \cos \left[\frac{i4\pi d}{\lambda} \sqrt{n^2 - \sin^2 \theta} + 1 - \cos \theta + \phi_s - \phi_r \right] . \quad (3.16)$$

The intensity modulation caused by the interference is observed at the detector, and it is shown in Fig. 3.10 (top).

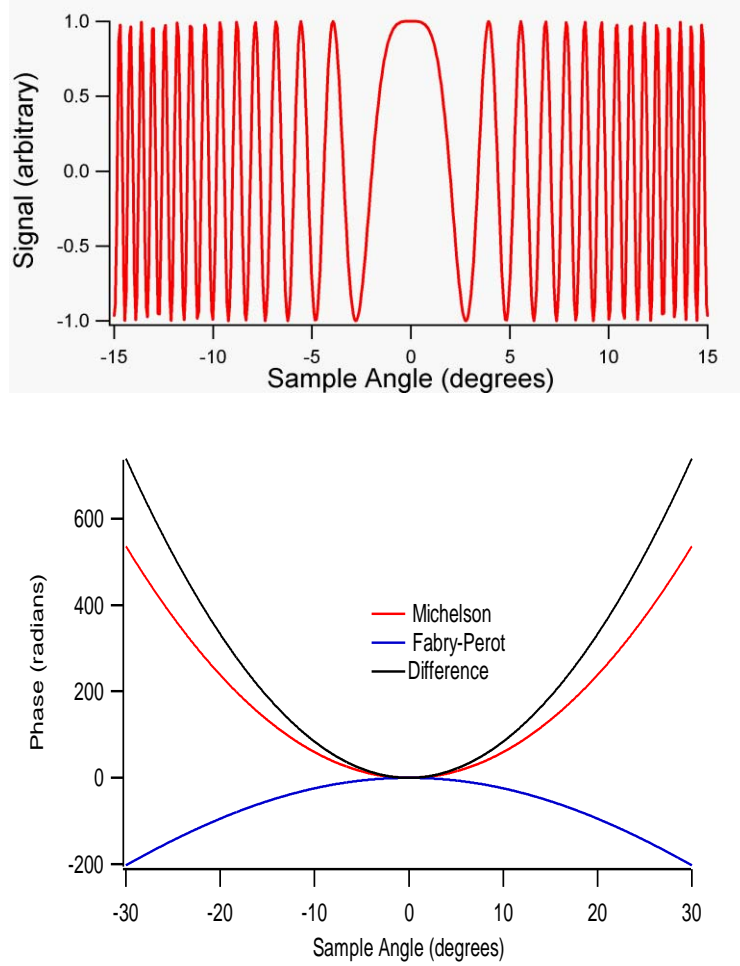


Figure 3.10. (top) Michelson interferometer interference pattern observed at a detector; (bottom) phase information extracted from the interference pattern for both setups and their difference

The phase information from interference pattern peaks were extracted as shown in Fig. 3.10 (bottom) and fits to equation 3.17 given by

$$\phi_m(\theta) = \frac{4\pi d}{\lambda} (\sqrt{n^2 - \sin^2 \theta} + 1 - \cos \theta). \quad (3.17)$$

Thus, the refractive index n can be calculated if d , the thickness of the sample, is known.

If the sample thickness is unknown, Fabry-Perot interferometer will be needed.

A simple Fabry-Perot interferometer is formed when the reference mirror in Fig. 3.8 is blocked. Rotating sample results in laser intensity modulations of the transmitted light due to the interference of multiple internal reflections. Similar to Michelson interferometry, an interference pattern is received at a detector and the phase information can be extracted using equation 3.18 given by

$$\phi_{fp}(\theta) = \frac{4\pi d}{\lambda} (\sqrt{n^2 - \sin^2 \theta}). \quad (3.18)$$

When combining both Michelson and Fabry-Perot interferometers, the sample thickness is decoupled as shown in equation 3.19, thus both d and n can be determined.

$$\phi_m(\theta) - \phi_{fp}(\theta) = \frac{4\pi d}{\lambda} (1 - \cos \theta). \quad (3.19)$$

Refractive-index measurements were carried out on bulk $\text{In}_x\text{Ga}_{1-x}\text{As}$ wafer fabricated from a boule grown using multi-zone vertical gradient freeze (VGF) technique. The sample was placed in a LN_2 cooled cryostat. The cold finger was mounted on a rotation stage with a resolution of $\pm 0.001^\circ$. Two discrete laser sources were used, a pulsed (kHz) frequency doubled CO_2 laser at $4.6 \mu\text{m}$ (2W) and a grating CW CO_2 laser at $10.6 \mu\text{m}$ (200 mW). All light sources were chopped at a repetition rate of 50 Hz using a ThorLabs optical chopper synchronized to a lock-in amplifier. The signal-to-noise ratio could be increased using lock-in amplifier (SR850). Different beam splitters were used for each laser source, a dielectric coated CaF_2 (50/50) for the $4.6 \mu\text{m}$ laser and a coated ZnSe (50/50) for the $10.6 \mu\text{m}$ laser. A Boston Electronics HgCdTe photodiode was used

for MIR and Long IR, and a ThorLab InGaAs detector for NIR used to measure the laser intensity. Both the reference and sample mirrors are gold mirrors.

Prior to sample measurement, the calibration procedure is conducted using an ISP Optics silicon window. Calibration results are listed in table 3.2.

Table 3.2. Refractive index results of an ISP Optics Si window and published results of Si

ISP optics Si-w-25-2	Thickness	Refractive index
Measured Result	2.035 mm	3.421±0.005 at 4.6 μm @ 295 K 3.416±0.003 at 10.6 μm @ 295 K
reference [66]		3.415 at 10.6 μm @300 K
reference [67]		3.4214 at 4.6 μm @300 K

3.4 Electron Probe Micro Analyzer (EPMA)

The electron micro probe analysis method allows determination of sample composition. The instrument shown in Fig. 3.11 (top) is a Cameca SX-100 electron probe micro analyzer. The measurement technique is called Wavelength Dispersive Spectroscopy (W.D.S). A high energy electron beam (typically at 5-30 keV) is focused onto the sample. The electrons excite characteristic X-rays for the elemental constituents that are present within the specimen material as shown in Fig. 3.11 (bottom).

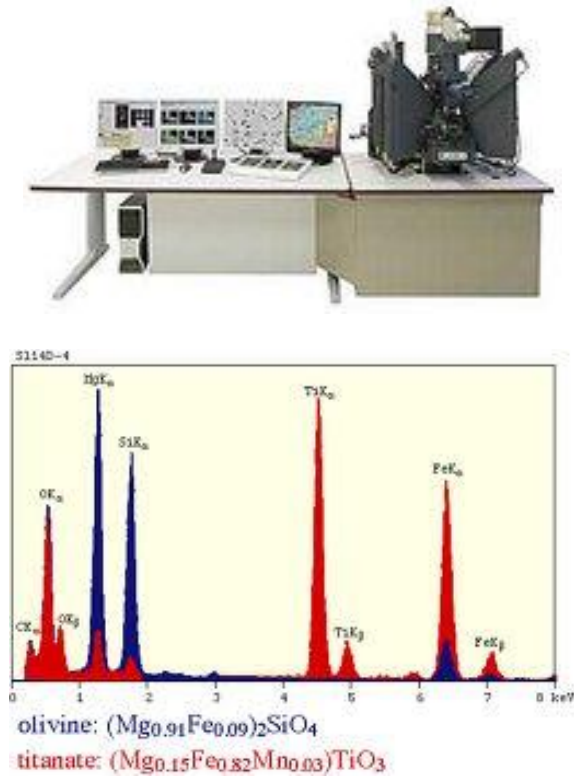


Figure 3.11. (Top) Electron probe micro analyzer (EPMA): CAMECA 100. (Bottom) a typical analysis spectrum of EPMA.

The X-ray count rates are then measured on the specimen, and they are compared against the x-ray count rates collected from the standard reference materials composition. A matrix correction is then applied to convert the X-ray count rate into concentration values in weight fraction. In our case, the data was then normalized to 100% total composition so that the concentrations could be reported as an atomic percentage. The SX-100 uses the PAP matrix correction in which PAP is a general model for the calculation of X-ray intensities and can be used for a wide range of X-ray energies (100 eV to greater than 10 keV) and accelerating voltages (1- 40 keV). GaAs, InAs, and InP were used as reference materials for the calibration of the wavelength dispersive spectrometers for our analyses. Calibration is always done just prior to analysis.

The volume of specimen material analyzed is tear drop shaped having a diameter on the order of a few microns ($5\text{ }\mu\text{m}$) at each analysis point. The size of the analysis volume varies depending on several factors such as accelerating voltage of the electrons, average atomic number of the specimen material, and energy of the X-rays being excited. In this study, each measurement is an average result from 16 sample locations. However, since this is a micro analyzer, it may have its limit in studying bulk composition of large area. In this study, two methods (micro analyzer and PL) will be compared in the analysis of composition.

3.5 Infrared Imagery

Since these samples are optically transparent in the infrared, a Santa Barbara Focalplane ImagIR infrared camera [68] shown in Fig. 3.12 was used for this study. This camera uses an InSb focal plane arrays and includes Integrated Detector/Dewar/Cooler Assemblies, and digital camera heads.



Figure 3.12. Santa Barbara focaplance image IR infrared camera.

The imaging system is shown in Fig. 3.13, where sample is placed in front of the camera. At the far left is a black body source. Next are two lenses to collimate the blackbody in order to illuminate on the back surface of the sample. The PC is connected to the integrated InSb detector, and using the WinIR software, the image from the PC can be saved to a digital disc.

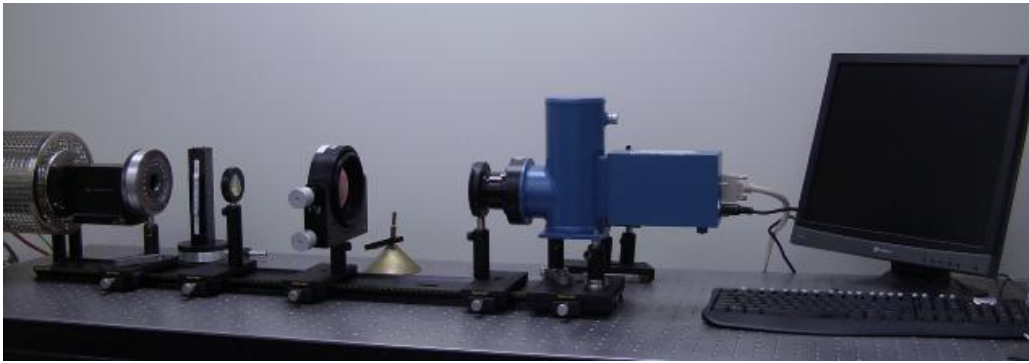


Figure 3.13. MIR imaging system using Santa Barbara Focalplane ImagIR.

Typical IR images obtained from this camera are shown in Fig. 3.14. In these images, a photodiode (heat source) is placed next to the sample to enhance the visibility. Six InAs samples of different thicknesses and from different vendors were viewed. From Fig. 3.14, sample HAFB5_1, IA 03052_1 and IA03052_2 show good optical quality by their high optical transparency and uniformity. On the other hand, cloudy spots and light scattering were seen in sample IA 03052_1 and IA 03051_2, indicating defects in these crystals.

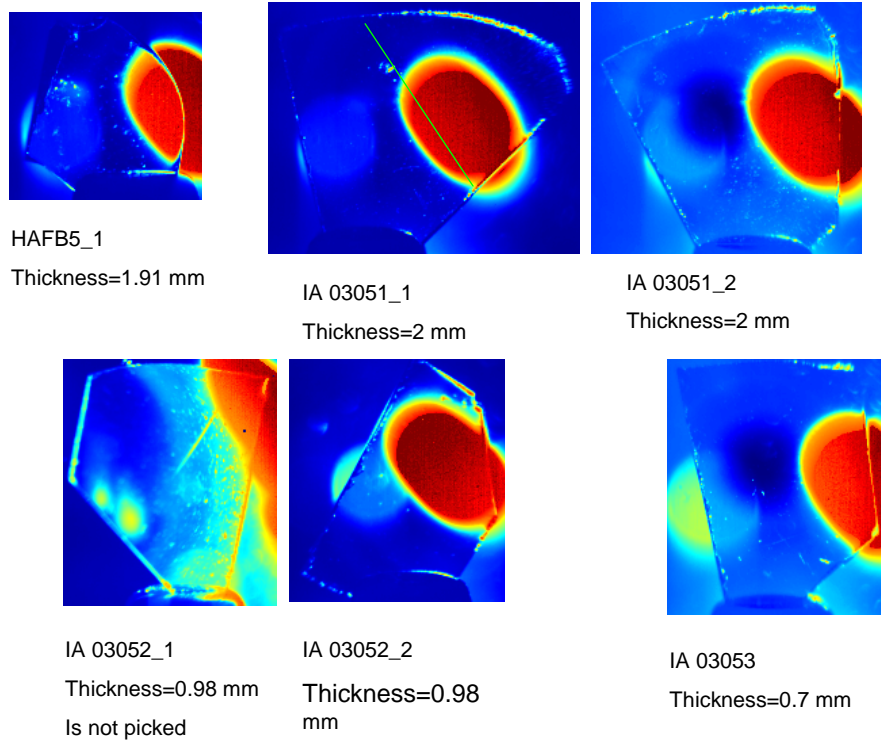


Figure 3.14. MIR images of six InAs crystals using Santa Barbara focal plane infrared camera.

4. Results and Discussions of Binary InAs, InP, and GaAs

4.1 Purpose

Studying binary crystals such as InAs, InP and GaAs serves two purposes. First, they are the end compositions of ternary $\text{In}_x\text{Ga}_{1-x}\text{As}$ and $\text{InAs}_{1-y}\text{P}_y$ ($x, y = 0$, or 1). Therefore, these binaries are natural boundaries of the ternary alloys. Second, binary (epitaxial layer or bulk) InAs, InP, and GaAs have been extensively studied in the past, so many electrical and optical properties are known. Thus these binaries can provide excellent reference points by extrapolating the results obtained from ternary properties as a function of composition. Moreover, not all the optical properties for binary compounds are known, for example, at cryogenic temperature or over a wide spectral range. This work provides the necessary measurements over the extended temperature and spectral range.

4.2 Determination of Bandgap Energy

PL is a well established method of estimating bandgap energy [69]. The absorption coefficient (α) method [70] is another way to determine bandgap energy in semiconductors. In both cases, they are not always available at all desired temperatures or spectral ranges. For instance, most PL measurements are carried out at cryogenic temperatures and the PL peak becomes broad as the temperature increases, disappearing long before reaching room temperature. As a result, it is difficult to estimate the bandgap energy at room or higher temperatures using PL. As for the absorption coefficient method, it is dependent on the absorption edge intersecting the photon energy in the absorption spectra, which can be complicated by impurities in the semiconductor.

Impurities can cause band tailing [71, 72], making it difficult to accurately determine the bandgap energy. This complication becomes worse when studying newly developed materials such as melt-grown bulk ternary $\text{In}_x\text{Ga}_{1-x}\text{As}$ and $\text{InAs}_{1-y}\text{Py}$. Since their crystal growth condition has yet to be optimized, the current state of ternary crystal quality is far from being perfect. In other words, impurity and/or defect levels could be high. In the worst case, PL can be scattered and the PL spectrum may be completely unavailable. Therefore, the absorption coefficient method must be used to find bandgap energy.

The following sections describe an alternative method of extracting the bandgap energy directly from the transmission spectra.

The expression for transmission through an etalon is given as:

$$T = \frac{(1-R)^2 e^{-\alpha d}}{1-R^2 e^{-2\alpha d}}, \quad (4.1)$$

where T is the transmittance, R is the reflectance, α is the absorption coefficient, and d is the sample (wafer) thickness. At normal incidence, $R = \left(\frac{n-1}{n+1}\right)^2$, where n is the index of refraction. For a single pass, transmission at normal incidence is given by

$$T = \frac{I}{I_0} = (1-R)^2 e^{-\alpha d}. \quad (4.2)$$

For semiconductors, there are two regions near the bandgap. One of them is known as the Urbach region [73], where the energy is less than bandgap. Another is known as the Kane absorption region [74], where the energy is greater than bandgap. That is, the absorption coefficient can be approximately expressed as

$$\begin{aligned}\alpha &\approx Ce^{(E-E_g)/E_t}, E < E_g \\ \alpha &\approx A\sqrt{E-E_g}, E > E_g.\end{aligned}\tag{4.3}$$

Here the C and A parameters are constants for a given material, for instance, A is the density of state in conduction band. E_t is an empirical value with a dimension of energy, which is on the order of thermal energy $k_B T$ for some materials. Note here that the derivative of α with respect to the photon energy can be expressed as

$$\begin{aligned}\frac{d\alpha}{dE} &\approx \frac{C}{E_t} \exp\left(\frac{E-E_g}{E_t}\right), E < E_g \\ \frac{d\alpha}{dE} &\approx \frac{A}{2} \frac{1}{\sqrt{E-E_g}}, E > E_g.\end{aligned}\tag{4.4}$$

Thus, in the Urbach absorption range, the derivative is an exponentially increasing function. On the other hand, in the Kane region, the derivative is decreasing as $(E-E_g)^{-1/2}$. This leads to a sharp peak of $d\alpha/dE$ in the vicinity of the transition between the two types of absorption, which occurs at $E \approx E_g$ as shown in Fig.4.1 (a) [75] for the uniform bulk semiconductor materials. Therefore, E_g of a bulk sample with uniform composition can be estimated from the location of the peak of $d\alpha/dE$.

For a material with non-uniform compositions, there is a contribution from both types of absorption depending on $E < E_g$ or $E > E_g$, and $d\alpha/dE$ does not show a sharp peak. Consequently, $d\alpha/dE$ for a material with non-uniform compositions will result in a smoother, wider peak in comparison with the derivative for a uniform bulk material as shown in Fig. 4.1.(a). The width of the peak depends on the range of composition variation, which provides a range of bandgap variation in the material. In order to determine these boundaries of the mixed absorption region (the range of composition

variation) more precisely, the second derivative, $d^2\alpha/dE^2$, is obtained as shown in Fig. 4.1 (b) [75], where points of peaks are defined as $E_{g \text{ min}}$ and $E_{g \text{ max}}$. The energy difference $\Delta E_g = E_{g \text{ max}} - E_{g \text{ min}}$ can be measured as the distance between the peaks of $d^2\alpha/dE^2$ and $d\alpha/dE$. While the derivative peaks (1st and 2nd) do not indicate the precise numerical value of the bandgap, this approach appears to be very sensitive to bandgap variations within the material [75].

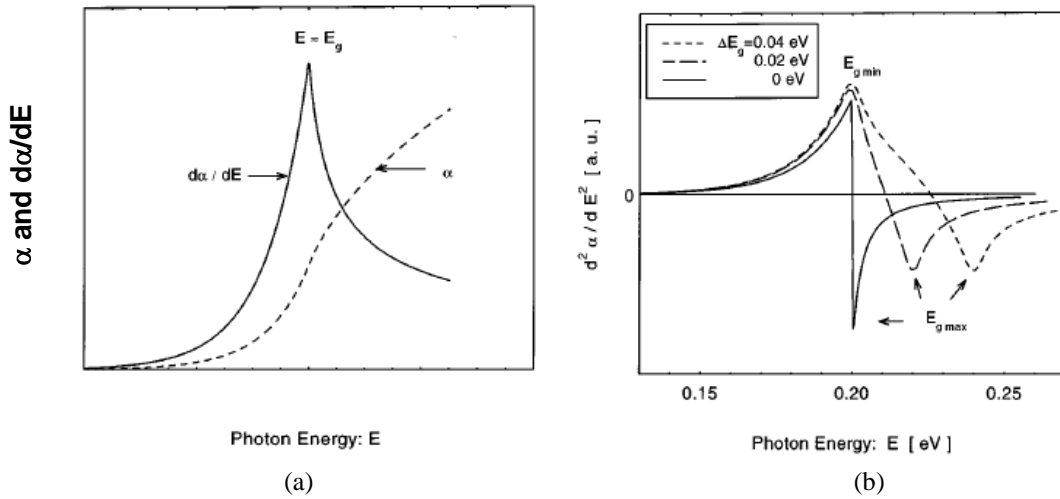


Figure 4.1. (a) A theoretical graph of the absorption coefficient and its first derivative in a uniform bulk sample showing a sharp peak of the derivative in the vicinity of the bandgap. (b) The second derivative of the absorption coefficient for different values of bandgap variation within the sample.

4.2.1 Bandgap Energy Obtained from Transmission Spectra for InAs

Our modified method is based on Ariel's model [75]. It begins with taking the first and second derivatives of transmission (equation 2.4) instead of the absorption coefficient with respect to the photon energy. After some rearrangement, the first and second derivatives of transmission are as follows.

$$-\frac{dT}{dE} = d \frac{d\alpha}{dE} e^{-\alpha d} = T d \alpha' \quad (4.5)$$

$$\frac{d^2T}{dE^2} = Td\left[d\left(\frac{d\alpha}{dE}\right)^2 - \frac{d^2\alpha}{dE^2}\right] \quad (4.6)$$

Transmission spectra of a set of InAs 143 samples with different thickness were measured at room temperature and the results are shown in Fig. 4.2. (a). These wafers were grown by the Wafer Technology Company, and diced and thinned by United Semiconductor LLC into seven pieces with thicknesses ranging from 100 – 1000 μm .

$E_{L \min}$ and $E_{L \max}$ can be determined from the peak locations of $-\frac{dT}{dE}$ and $-\frac{d^2T}{dE^2}$ as shown in Fig. 4.2 (b) and (c), respectively. They have similar characteristics of the $E_{g \min}$ and $E_{g \max}$ shown in Fig. 4.1(a) and (b). The difference is that $E_{L \min}$ and $E_{L \max}$ shown in Fig. 4.2 (b) and (c) are sample thickness dependent, whereas the $E_{g \min}$ and $E_{g \max}$ are not.

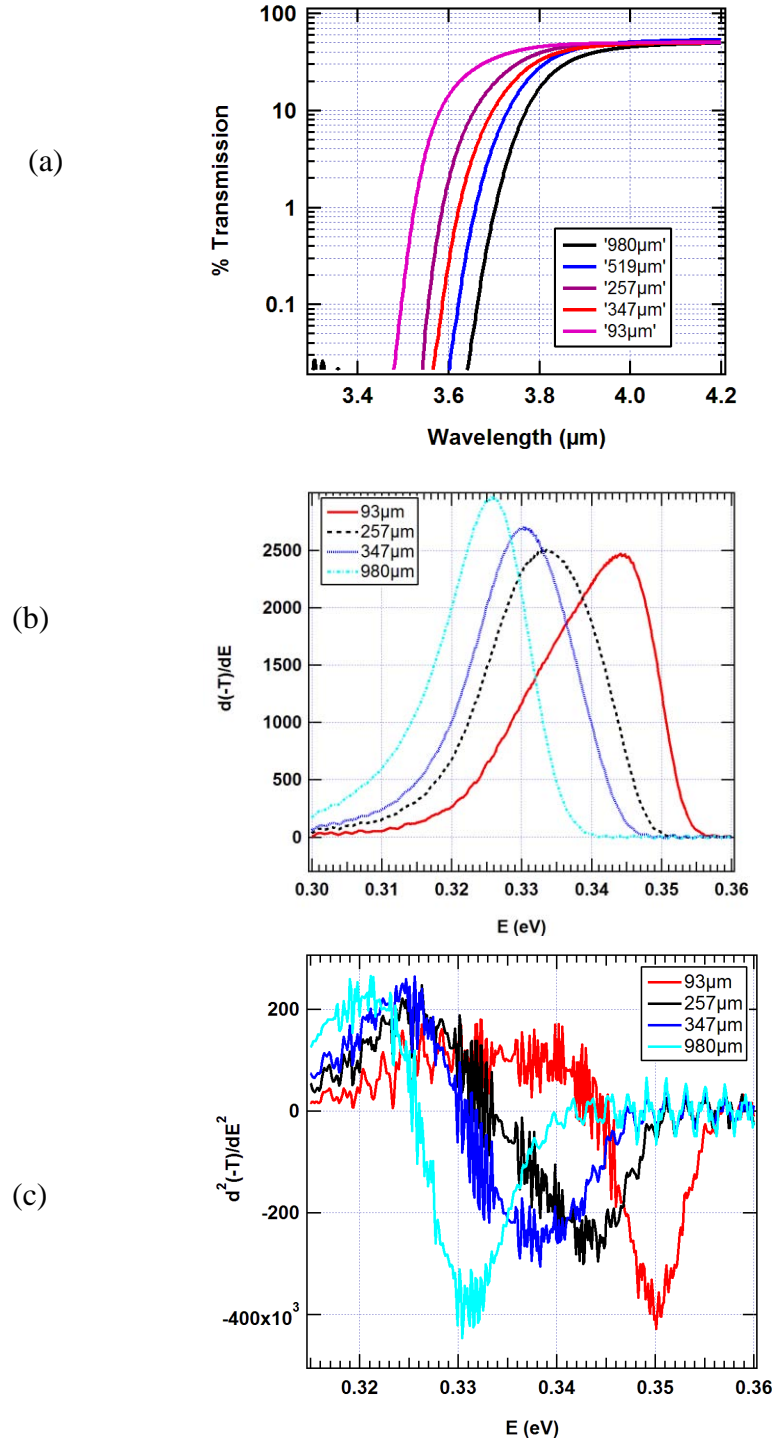


Figure 4.2. (a) Transmission spectra of InAs 143 samples with five thicknesses (b) $d(-T)/dE$ vs. E . Peak locations are defined as $E_{L \min}$. (c) $d^2(-T)/dE^2$ vs. E . The minimum locations are defined as $E_{L \max}$. E is photon energy.

The values of $E_{L \min}$ and $E_{L \max}$ energies in eV were extracted from the peak locations of $-\left(\frac{dT}{dE}\right)$ and $-\left(\frac{d^2T}{dE^2}\right)$, respectively and the results are plotted as a function of thickness in

Fig. 4.3. Difference between $E_{L \min}$ and $E_{L \max}$ is in the range of 5 – 10 meV for each sample and both data are fit to exponential function as shown in equations 4.7 and 4.8.

$$E_{L \min} = 0.326 + 0.032 \exp(-d/164) \quad (4.7)$$

$$E_{L \max} = 0.329 + 0.028 \exp(-d/341), \quad (4.8)$$

where d is the sample thickness in μm .

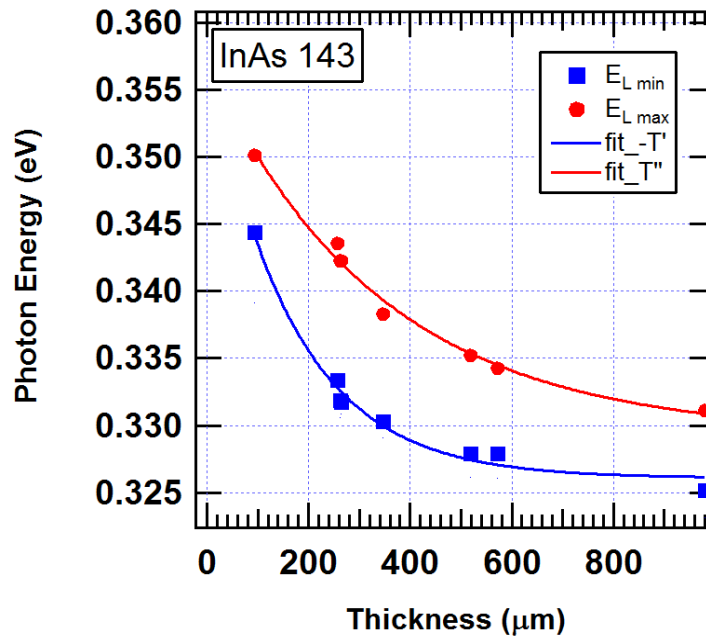


Figure 4.3. $E_{L \min}$ and $E_{L \max}$ vs. Sample thickness for a set of InAs 143 samples

From equations 4.7 and 4.8, $E_{L \min}(d=0) = 0.358$ eV and $E_{L \max}(d=0) = 0.357$ eV, which agree very well with the published InAs bandgap values, that are in the range of 0.354~0.36 eV at room temperature, [69, 76-77]. Thus, $E_g = E_{L \min}|_{d=0} \approx E_{L \max}|_{d=0}$.

Another observation from Fig. 4.3 is that $E_{L \min}$ decreases faster than $E_{L \max}$ as sample thickness increases from 0 to 600 μm , and then $E_{L \min}$ almost remains constant after $d > 800 \mu\text{m}$. For InAs, this also reveals that for a thick sample ($d \geq 1 \text{ mm}$), the difference between bandgap energy and E_L , $(E_g - E_{L \min})$ or $(E_g - E_{L \max})$, is about 32 and 28 meV, respectively.

4.3 Temperature Dependent Bandgap Energy Obtained from Transmission Spectra

Temperature dependent bandgap energy is valuable information for semiconductor material, but it is not available for many ternary materials such as InGaAs and InAsP. If the temperature dependent bandgap energy can somehow be extracted directly from the transmission spectra, it would be very useful, because the knowledge of temperature dependent bandgap energy $\left(\frac{dE_g}{dT}\right)$ is essential for device designers as well as field engineers. In addition, the temperature dependent refractive index (dn/dT) , known as the thermo optical coefficient, is another important parameter that can be calculated from $\left(\frac{dE_g}{dT}\right)$ [47].

In order to find E_g/dT , we like to start with taking second derivatives of the absorption coefficient

$$\frac{d^2\alpha}{dE^2} = \frac{C}{E_t^2} e^{\frac{E-E_g}{E_t}}, E < E_g, \quad (4.9)$$

$$\frac{d^2\alpha}{dE^2} = -\frac{A}{4} (E-E_g)^{-\frac{3}{2}}, E > E_g, \quad (4.10)$$

where $A \approx \frac{q^2 \left(2 \frac{m_h^* m_e^*}{m_h^* + m_e^*} \right)^{\frac{3}{2}}}{nch^2 m_e^*}$ is a constant for a given material [78,79]. From equation 4.6,

and 4.9, it can be found that

$$T'' = \frac{TdC \exp\left(\frac{E-E_g}{E_t}\right)}{E_t^2} [dC \exp\left(\frac{E-E_g}{E_t}\right) - 1], E < E_g \quad (4.11)$$

The peak location of (T'), which is $E_{L \min}$, can be found by solving equations 4.11 for

$T''=0$. Then,

$$E_g = E_{L \min} + E_t \ln(dC), E < E_g \quad (4.12)$$

Here, $E_{L \min}$ can be found from transmission data. E_t is a function of temperature.

4.3.1 Temperature Dependent Bandgap of InAs

Temperature dependent transmission spectra of an InAs sample WT 524-10 having a thickness of 1 mm is shown in Fig. 4.4 (top), and its $\left(-\frac{dT}{dE}\right)$ are plotted as a function of photon energy in Fig. 4.4 (bottom).

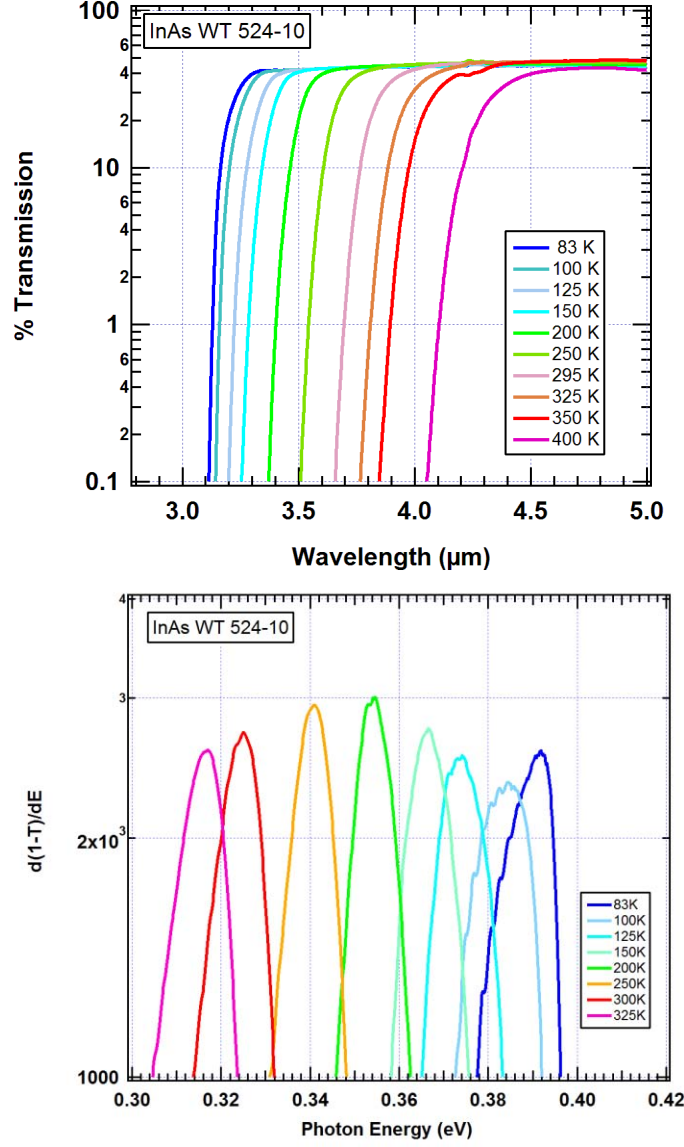


Figure 4.4. (Top) Temperature dependent transmission spectra of InAs sample WT 524-10.

(Bottom) temperature dependent $\left(-\frac{dT}{dE}\right)$ plotted as a function of photon energy

The values of $E_{L \min}$ (red dots) are extracted from the peak locations of $\left(-\frac{dT}{dE}\right)$ from Fig. 4.4 (bottom). Then the $E_{L \min}$ (red dot) are plotted as a function of temperature as shown in Fig. 4.5, along with the published bandgap of InAs by Fang *et al.* [69] (solid curve).

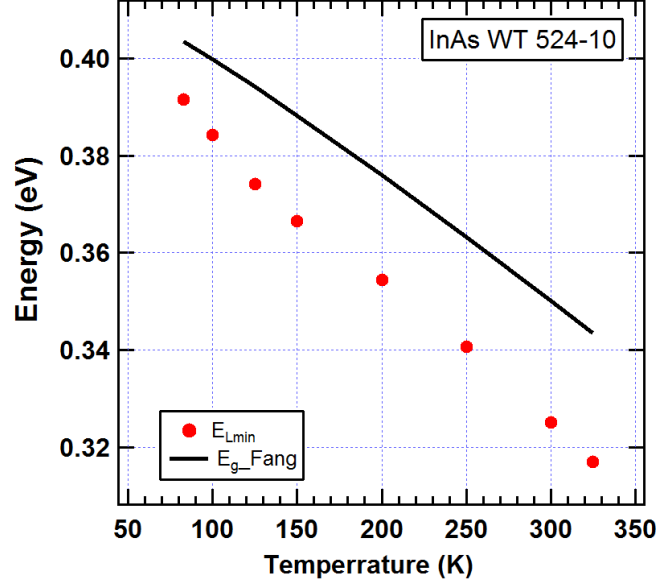


Figure 4.5. E_{Lmin} (red dot) extracted from transmission spectra of InAs and bandgap energy of InAs by Fang *et al.* (solid curve)

The difference between bandgap energy and E_{Lmin} , $(E_g - E_{Lmin}) = E_t \ln(dC)$, is plotted as a function of temperature in Fig. 4.6. Since E_t is a function of T , $[E_g - E_{Lmin}]$ (red dots) may be approximately fitted with a function of temperature (T) with a form θT^b . The fitting factor b is ~ 0.49 for InAs, and thus E_g can be expressed approximately as

$$E_g = E_{Lmin} + \theta \sqrt{T}, \quad (4.13)$$

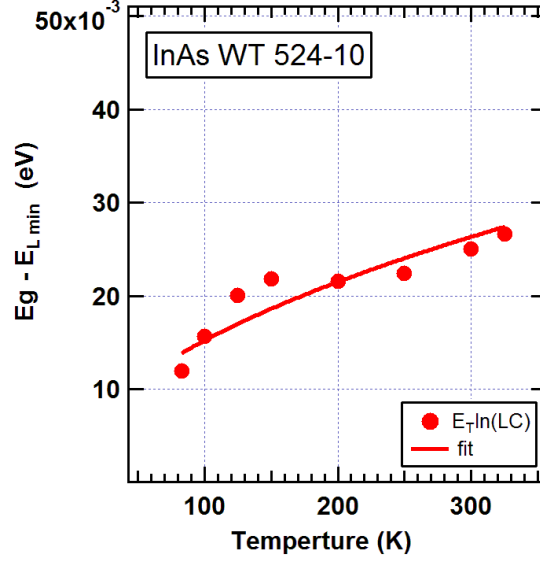


Figure 4.6. $E_g - E_{L \min}$ vs. temperature and a fitting curve with $E_g - E_{L \min} = \theta T^b$, with $b=0.5$.

where θ is a constant fitting parameter for a given material and thickness. For example, for InAs sample WT 524-10 with a 1 mm thickness, θ is found to be $\sim 0.0015 \text{ eVK}^{-0.5}$.

Using the expression given in equation 4.13, the temperature dependent bandgap energies of InAs WT 524-10 were calculated from the values of $E_{L \min}$, and the results (red dots) are plotted in Fig. 4.7 along with the published temperature dependent bandgap energies for InAs [69] (solid curve). This comparison demonstrates a good agreement with the published data [69], with the maximum deviation being less than 2 meV.

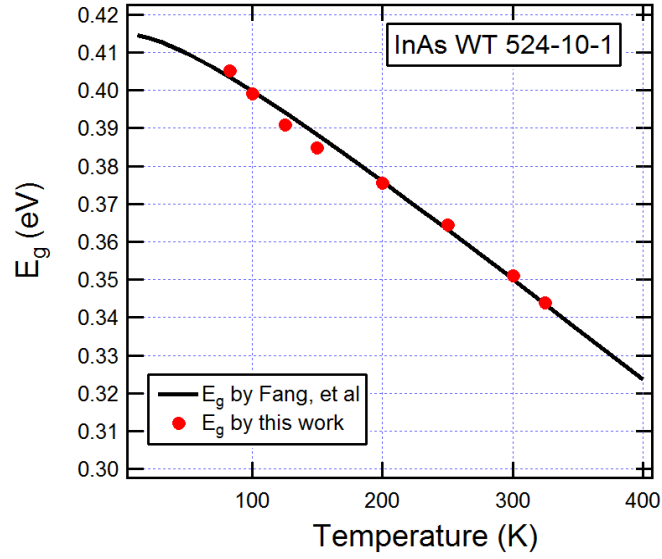


Figure 4.7. Temperature dependent bandgap energy obtained from transmission spectra (red dots) and published results (solid curve) by Fang, *et al.*

The relation of equation 4.13 was verified using three more InAs samples (InAs WT 524-11, D1, and 100) having different thickness and doping concentrations. The detailed sample information is listed in table 4.1, and their temperature dependent transmission spectra are shown in Fig. 4.8.

Table 4.1. InAs samples investigated for banggap estimation

Sample name	Doping	Type	Thickness (mm)	Carrier Concentration (cm ⁻³)
InAs WT 524-10	undoped	n	1.00	2.4×10^{16}
InAs WT 524-11	undoped	n	1.00	7.5×10^{16}
InAs D1	undoped	n	0.43	1.58×10^{17}
InAs 100	S-doped	n	0.50	5.17×10^{17}

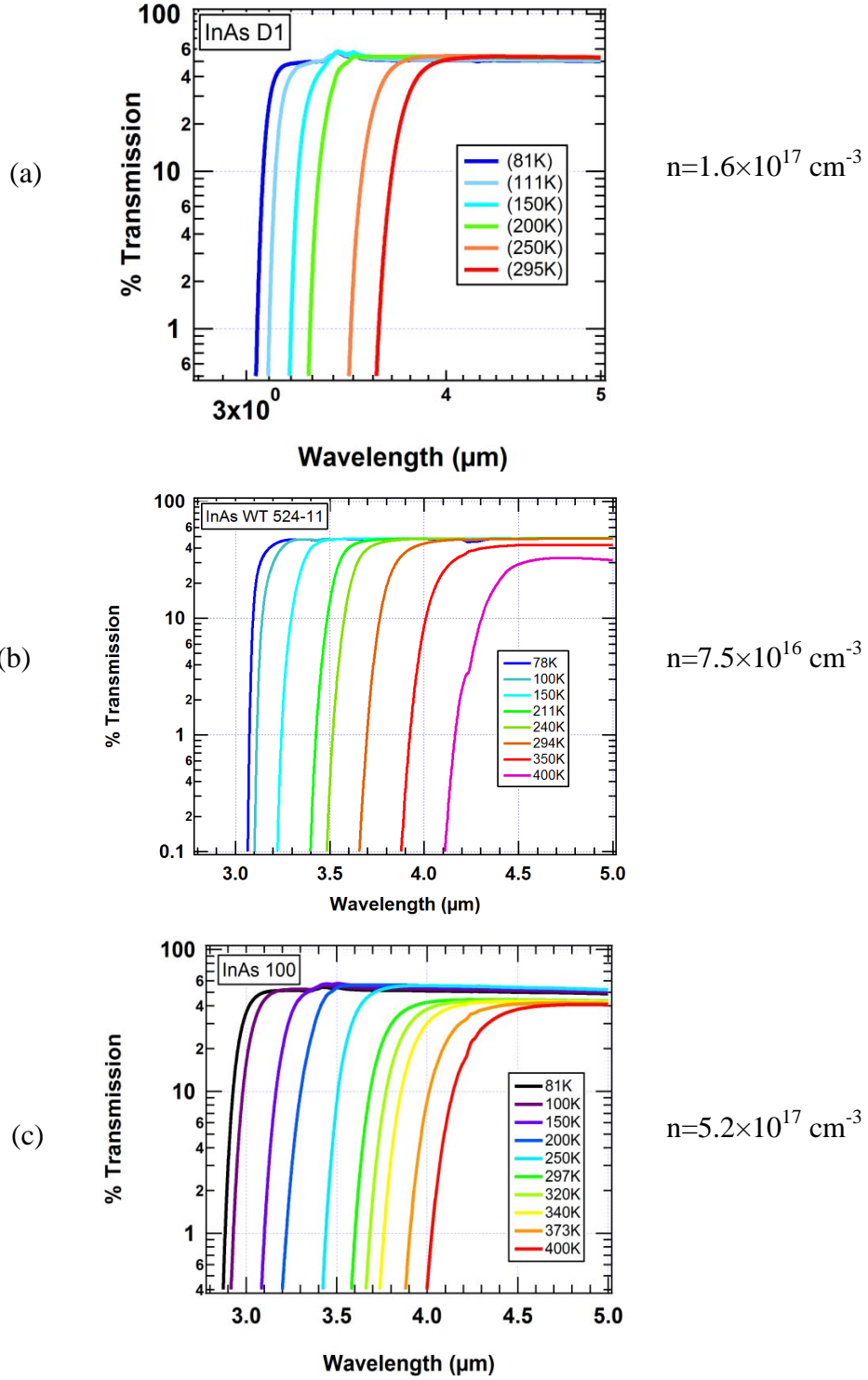


Figure 4.8. Temperature dependent transmission spectra of three InAs samples (a) InAs WT 524-11 (b) InAs D1 (c) InAs 100.

The values of $E_{L\ min}$ were extracted from each transmission spectrum and their bandgap energies then were estimated using $E_g = E_{L\ min} + \theta\sqrt{T}$ ($\theta=0.0015\text{ eVK}^{-0.5}$ for InAs). The results obtained from all four InAs samples are plotted in Fig. 4.9 (symbols), along with the published result (solid curve) by Fang *et al.* [69].

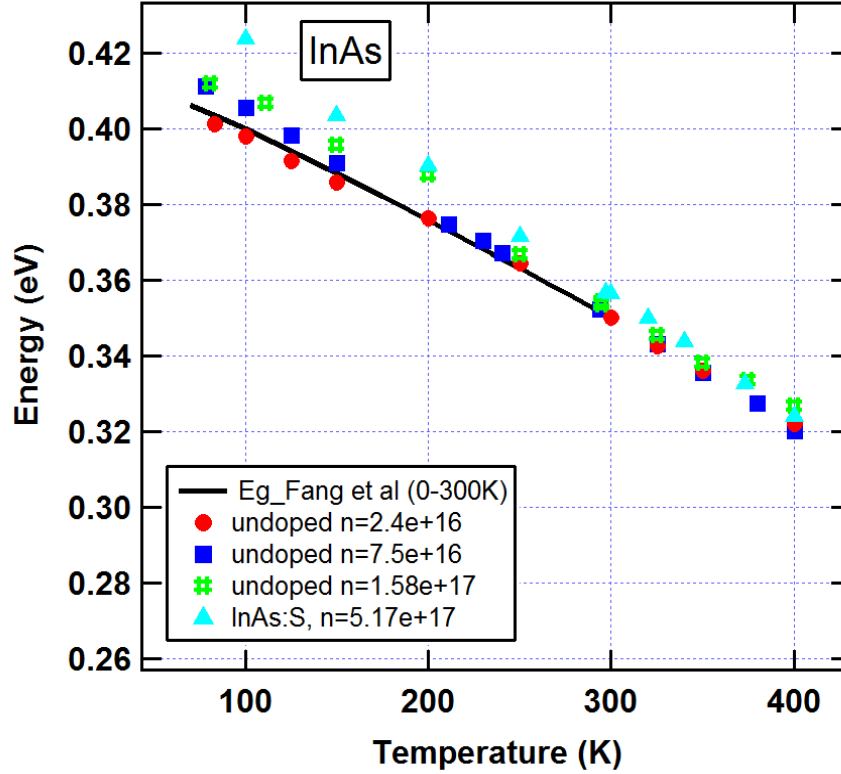


Figure 4.9. Temperature dependent bandgap energies of four InAs samples (symbols). The solid curve is temperature dependent bandgap energies reported by Fang *et al.*

Although there are some differences among the samples, overall, the results obtained from the transmission spectra agree well with each other and the published results. There is a trend shown in Fig. 4.9 that the apparent bandgap increases with carrier concentration, especially in the low temperature region. This behavior is believed to be due to band filling effect.

4.3.2 Temperature Dependent Bandgap of InP

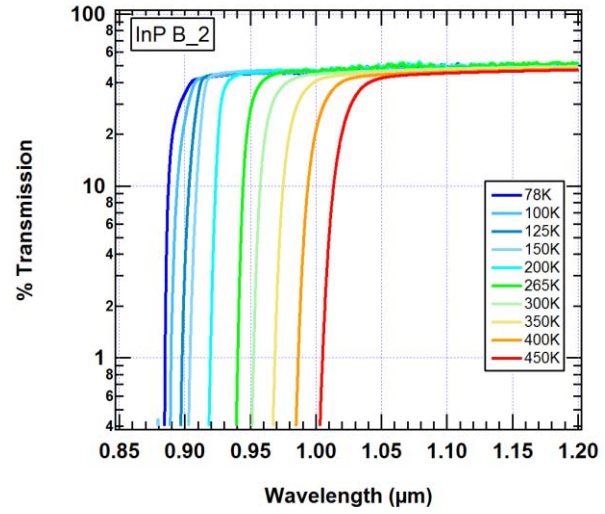
Three InP samples investigated and their detailed sample information are listed in table 4.2.

Table 4.2. InP Sample Information

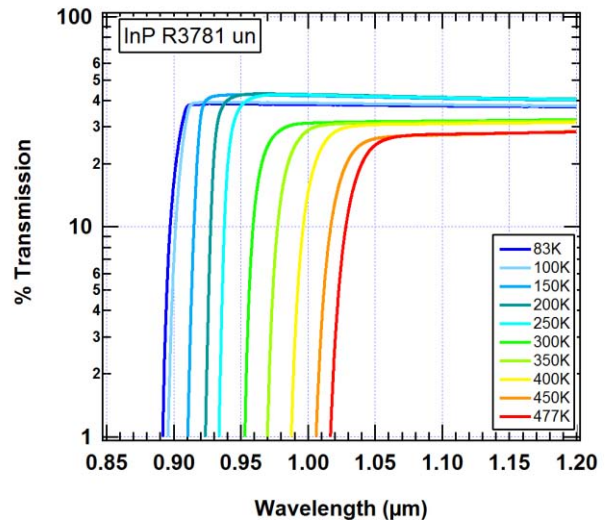
Sample name	Doping	Type	Thickness (mm)	Carrier Concentration (cm ⁻³)
InP R 3781 un_7	undoped	n	1.00	4.02×10^{17}
InP 6	undoped	p	0.96	1.56×10^{18}
InP B_2	undoped	n	1.00	2.47×10^{18}

Temperature dependent transmission spectra of these three InP samples are shown in Fig. 4.10.

(a)
1 mm thick
 $n = 2.47 \times 10^{18} \text{ cm}^{-3}$



(b)
1 mm thick
 $n = 4.00 \times 10^{17} \text{ cm}^{-3}$



(c)
0.96 mm thick
 $p = 1.56 \times 10^{18} \text{ cm}^{-3}$

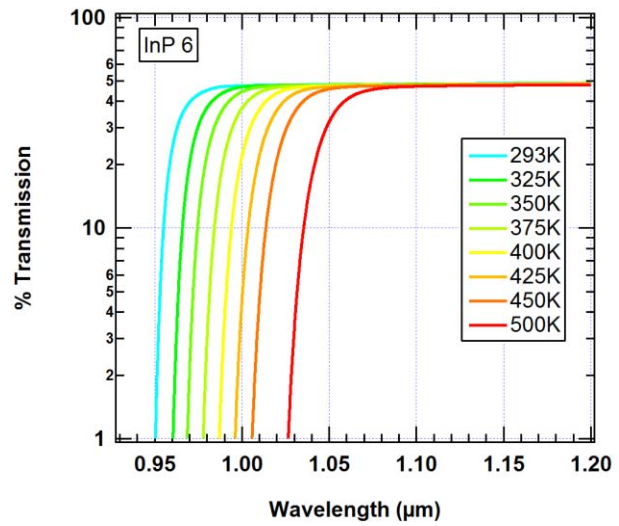


Figure 4.10. Temperature dependent transmission spectra of three InP samples (a) InP B2 (b) InP R3781 un (c) InP 6.

Fig. 4.11 shows two graphs of $(-\frac{dT}{dE})$ vs. photon energy for InP sample B2 and R3781 un, respectively. Sample InP 6 display similar characteristic curves as that of B2 and R3881 un, and it is not shown here. $E_{L\ min}$ values were extracted from the peak locations of $(-\frac{dT}{dE})$ for all InP samples, and were plotted in Fig. 4.12 (top) (symbols), along with the published E_g results (solid curve) [76]. The differences between E_g and $E_{L\ min}$ were plotted in Fig. 4.12 (bottom), and were fitted with equation 4.13. For these InP, the obtained θ value is $0.0036\text{ eV K}^{-0.5}$.

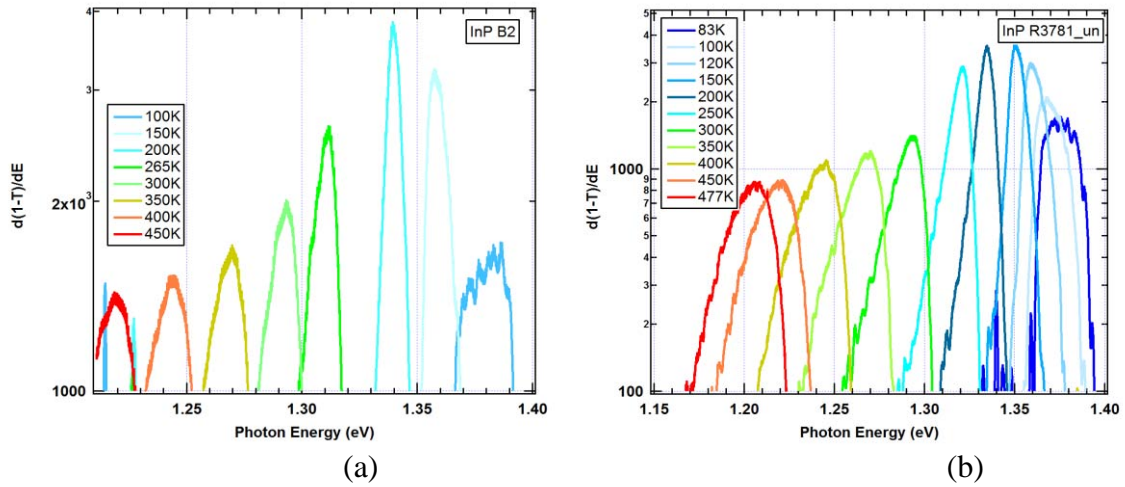


Figure 4.11. $\frac{d(1-T)}{dE}$ vs. E for InP sample at various temperatures (a) InP sample B2. (b) InP sample R3781_un.

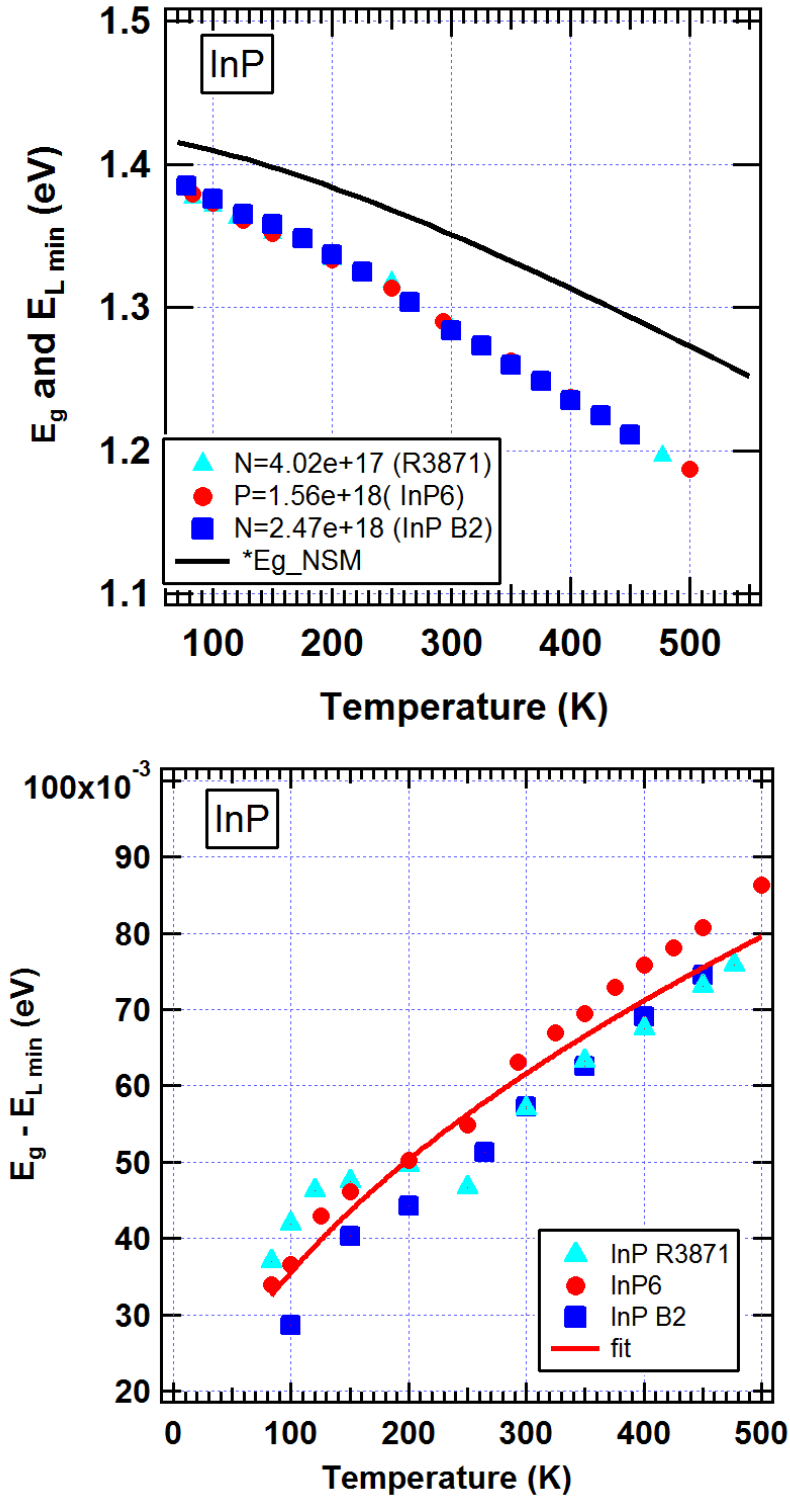


Figure 4.12. (Top) $E_{L\min}$ (symbols) of three InP samples and published E_g (solid curve). (Bottom) $(E_g - E_{L\min})$ plotted as a function of temperature. The curve is fitted with a power series function of θT^b with $b=0.5$.

Bandgap of InP as a function of temperature was calculated using equation 4.13 with known θ and $E_{L\ min}$ and the results are shown in Fig. 4.13. The published bandgap energies of InP [76] calculated using equation 4.14 are also plotted in this figure.

$$E_g(T) = 1.421 - \frac{4.9 \times 10^{-4}}{T + 327} (0 < T < 800). \quad (4.14)$$

The results obtained from transmission data demonstrate good agreement with the published values, and the average deviation is ~ 2 meV. It is interesting to point out that the bandgap energy of InP is less dependent on its carrier concentration than that of InAs. This could be because InAs has much narrower bandgap energy (0.354 eV) than InP (1.412 eV). When impurities are doped into the material, the doping affects band filling more for narrow than for wide bandgap materials.

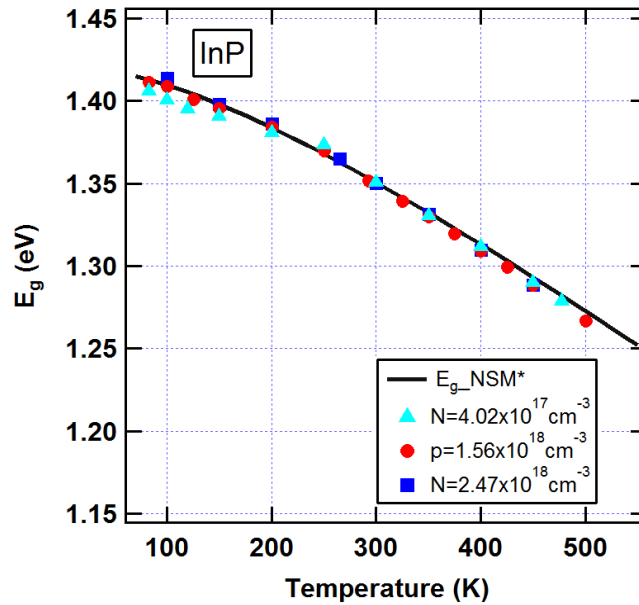


Figure 4.13. Temperature dependent bandgap energies obtained from transmission spectra (triangle, dot, and square) for three InP samples and published bandgap energies (solid curve).

4.3.3 Temperature Dependent Bandgap of GaAs

Transmission spectra were measured for several GaAs samples and they are listed in table 4.3. These are intrinsic samples and their exact carrier concentrations are not available.

Table 4.3. GaAs sample information

Sample name	Vendor	Thickness (mm)
GaAs 82	unknown	0.31
GaAs 19557	Wafer Tech	0.50
GaAs 12472-24	Wafer Tech	0.62

Temperature dependent transmission spectra of three GaAs samples are shown in Fig. 4.14 along with a $-\left(\frac{dT}{dE}\right)$ plot as a function of photon energy for GaAs sample 12472-24. The $-\left(\frac{dT}{dE}\right)$ plots of other two GaAs samples display similar characteristic curves as that of the GaAs sample 12472-24, and they are not shown here.

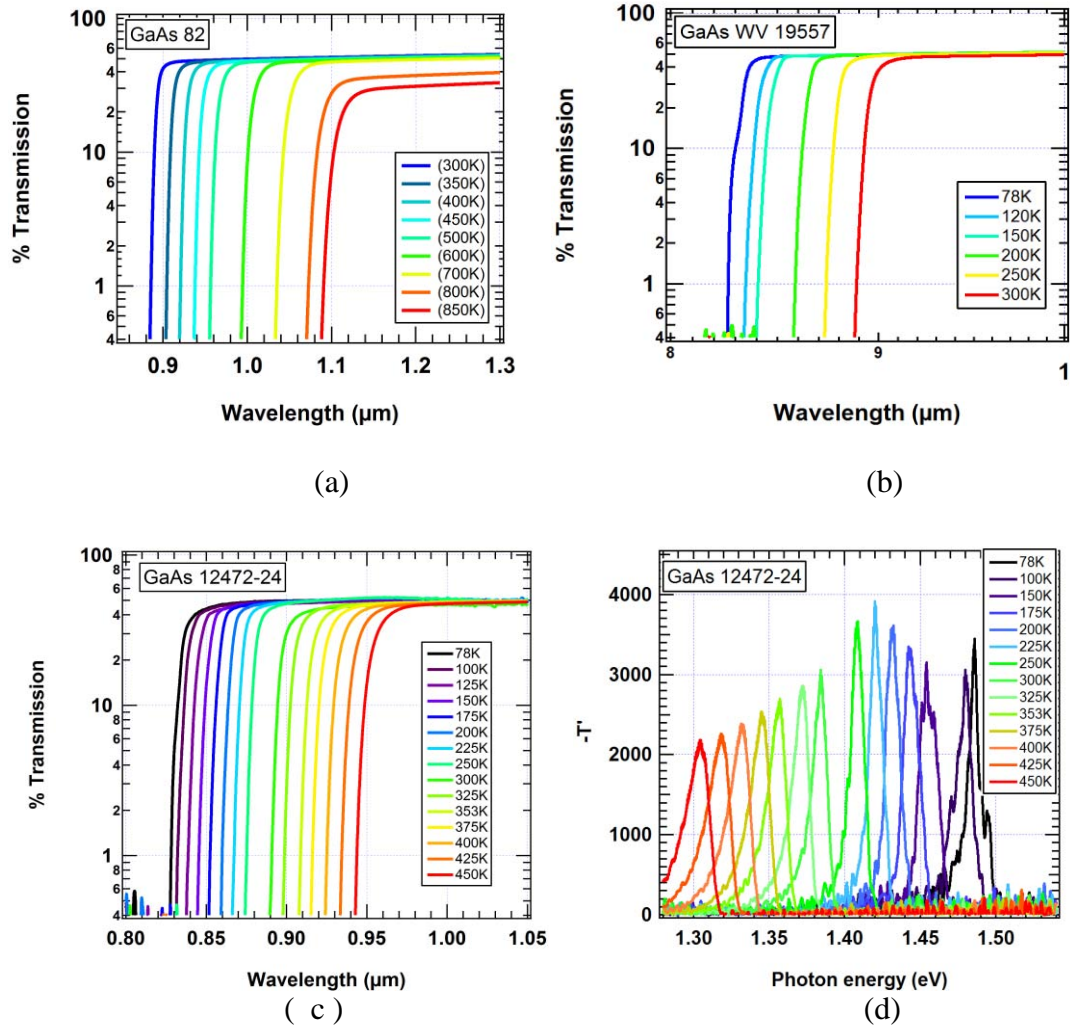


Figure 4.14. (a), (b) and (c) Temperature dependent transmission spectra of three GaAs samples of GaAs 82, GaAs WV 19557 and GaAs 12472-24, respectively. (d) $d(1-T)/dE$ of GaAs 12472-24 plotted as a function of photon energy.

$E_{L \min}$ values of all three GaAs samples were extracted from the peak locations of $-\frac{dT}{dE}$, and were plotted in Fig. 4.15 (a) (symbols) along with the published E_g values (solid curve) [76] that were calculated using the following equation 4.15.

$$E_g(T) = 1.519 - \frac{5.405 \times 10^{-4}}{T + 204} \quad (0 < T < 1000) \quad (4.15)$$

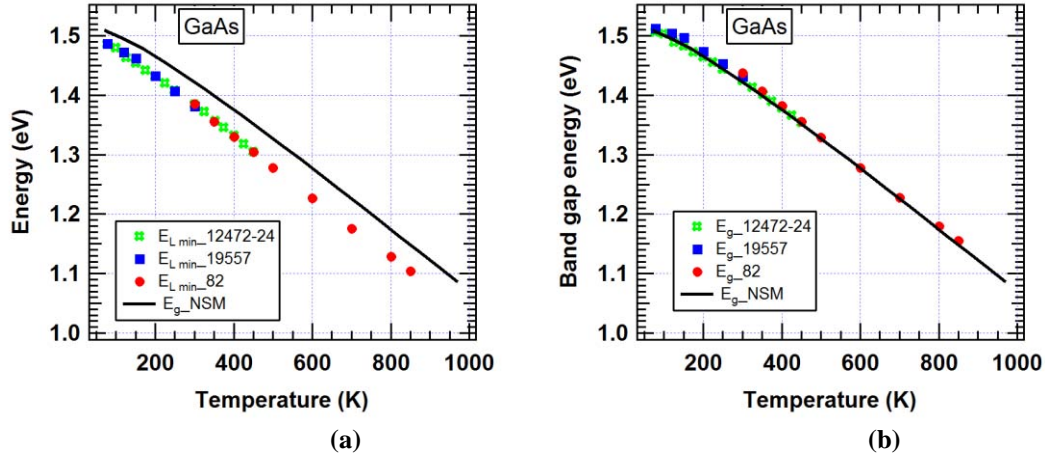


Figure 4.15. (a) Extracted $E_{L\ min}$ of three GaAs samples (symbols) and published E_g values (solid curve). (b) Temperature dependent bandgap energies of three GaAs samples obtained from transmission spectra (#, dot, and square) and published E_g values (solid curve).

The differences between the published bandgap energies and $E_{L\ min}$ of GaAs were curve fitted with a power series function of θT^b with $b=0.5$, and the obtained θ value was $0.0023\text{ eV K}^{-0.5}$. E_g was then calculated using equation 4.13 and the results were shown in Fig. 4.15 (b) along with the published data (solid curve). They exhibit good agreement in all temperature range and the maximum deviation is less than 3 meV.

The obtained θ values of InAs, GaAs and InP were plotted as a function of refractive index in Fig. 4.16. It seems that θ is inversely proportional to the refractive index, which is a purely empirical observation with no physical explanation so far. Further verification is needed to see whether this relationship will hold more generally for other III-V semiconductors such as GaN, GaP, GaSb and InSb or not.

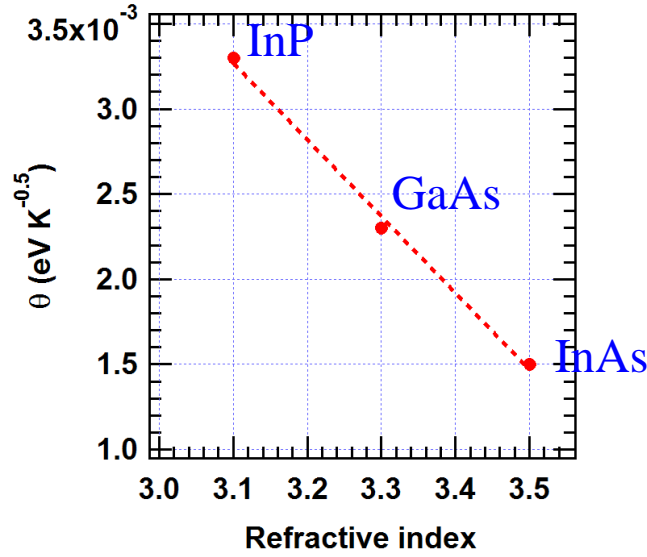


Figure 4.16. Obtained θ values plotted as a function of material's refractive index.

4.4 Determination of dn/dT from dE_g/dT

The refractive index is a very important optical parameter of a material. Measuring temperature dependent refractive index had been a challenge in the past, and thus the information on the temperature dependent refractive indices are lacking in the literature. Fortunately, the thermo optical coefficient, dn/dT , can be obtained from known dE_g/dT according to the theory [47], which was first reported by Dr. Milson. He started with a well-known concept that the refractive index is a function of bandgap energy, and its derivative can be calculated using equations 2.6 and 2.7.

At high temperatures ($T \geq 100$ K), E_g decreases linearly with T . For example, the slope of linear fit of temperature dependent bandgap shown in Fig. 4.7 for InAs sample WT 524-10 gives $dE_g/dT = -2.43$ eV K⁻¹. As a result, dn/dT of InAs can be calculated at different wavelengths using equations 2.6 and 2.7, and the results ($\lambda = 3.39, 4.6, 10.6$ μm) are listed in table 4.4, along with the experimentally measured data. For wavelength at

4.64 μm , there is a good agreement within an accuracy of 1.6% between the predicted dn/dT ($2.58 \times 10^{-4} \text{ K}^{-1}$) and the directly measured dn/dT ($2.54 \times 10^{-4} \text{ K}^{-1}$).

Table 4.4. Comparison between calculated dn/dT and measured dn/dT

λ (μm)	dn/dE_g (eV^{-1})	dE_g/dT ($\times 10^{-4}, \text{eVK}^{-1}$)	Calc. dn/dT ($\times 10^{-4}, \text{K}^{-1}$)	Measured dn/dT ($\times 10^{-4}, \text{K}^{-1}$)
3.39	-1.43	-2.43	3.48	2.55
4.64	-1.06	-2.43	2.58	2.54
10.6	-0.64	-2.43	1.45	1.96

4.5 Refractive-Index Measurements

The prism angle is measured using the setup shown in Fig 4.17. A red HeNe laser was aligned perpendicular to the prism. A photo diode detector with a 25 μm pinhole aperture was mounted next to the HeNe laser. The distance between detector and the prism was about 65 cm, which gives an accuracy of the prism angle measurement to 1.3×10^{-3} degree. To measure the prism angle, first, the initial angle is defined by adjusting the laser beam reflected from the prism as the maximum intensity at the detector location. Then the prism is rotated until the HeNe laser is reflected back from another side of the prism surface to obtain the maximum intensity at the detector position. The prism angle $\alpha = \text{absolute value of } (180 \pm \text{the rotation angle})$, where + or – is dependent on the rotation direction.

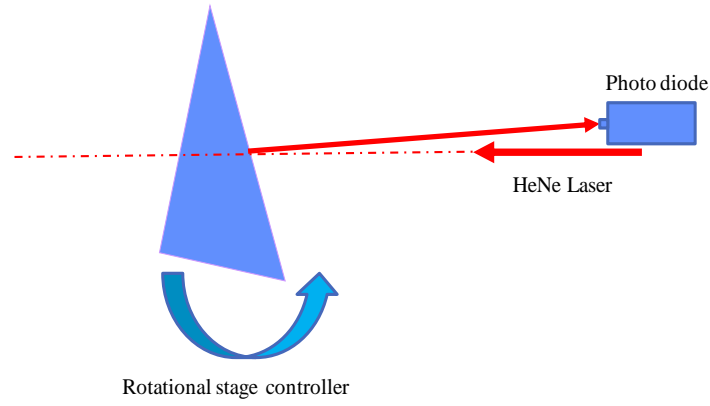


Figure 4.17. Prism angle measurement setup.

After determination of the prism angle and the minimum deviation angle, the temperature dependent refractive indices of InAs were calculated using equation 3.13 at three wavelengths (3.39, 4.6, 10.6 μm) and at temperatures ranging from 95 – 295 K. The measured results of refractive index and dn/dT are shown in Fig. 4.18 (a). The slope of the linear fit (dashed lines) provides the dn/dT at that particular wavelength. The dn/dT of all three wavelengths were obtained and plotted as a function of the wavelength in Fig. 4.18 (b) (red dot), along with the best fit curve (dashed line).

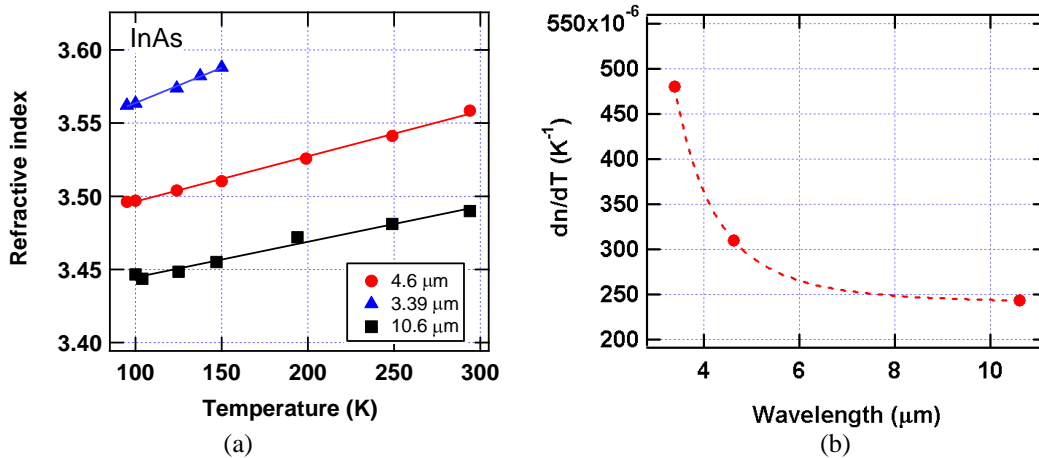


Figure 4.18. (a) Temperature dependent refractive indices of InAs measured at three wavelengths of 3.39, 4.6 and 10.6 μm . (b) Best fit curve for dn/dT vs. wavelength.

Similarly, the temperature dependent refractive indices of InP at four wavelengths (1.55, 3.39, 4.64 and 10.6 μm) were measured and the results are shown in Fig. 4.19 (a) . The slope of the linear fit (dashed line) provides the thermal optical parameter (dn/dT) of InP, and was plotted as a function of wavelength in Fig. 4.19 (b) along with a best fit curve.

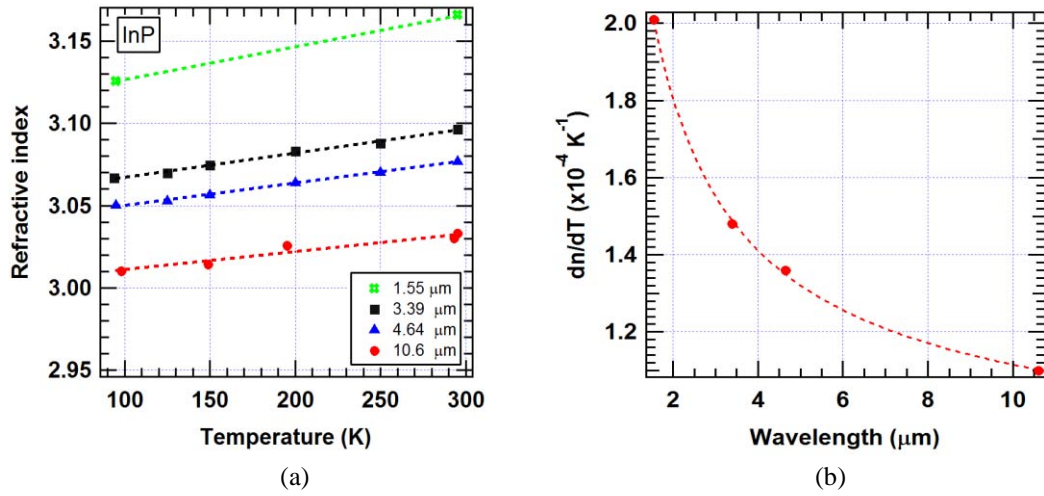


Figure 4.19. (a) Temperature dependent refractive index of InP measured at four wavelengths of 1.55, 3.39, 4.6 and 10.6 μm . (b) Best fit curve for dn/dT vs. wavelength.

Similar to InAs, the theoretical value of dn/dT can be calculated using equations

2.6 and 2.7. Assuming $E_p \approx \frac{3E_g}{4\left(\frac{m_c}{m_e}\right)}$, $E_p \sim 12.66 \text{ eV}$ can be obtained for InP. The

temperature dependent bandgap energy for InP was evaluated in section 4.3, and at high temperatures ($T > 100 \text{ K}$), $dE_g/dT = -2.88 \times 10^{-4} \text{ eV K}^{-1}$. Also dn/dE_g was calculated using equation 2.7. Using these values, dn/dT at different wavelengths were obtained and listed in table 4.7 along with the experimentally measured results. From table 4.7, one can see that the calculated dn/dT does not agree well with the experimental results. This

is probably due to inaccurate dn/dE_g . The relationship $E_p \approx \frac{3E_g}{4\left(\frac{m_c}{m_e}\right)}$, is probably valid only

for narrow bandgap material such as InAs (0.354 eV), and may not be valid for wide bandgap semiconductors such as InP (1.35 eV).

Table 4.5. Comparison between calculated dn/dT and experimental dn/dT

λ (μm)	dn/dE_g (eV^{-1})	dE_g/dT ($\times 10^{-4}, \text{eVK}^{-1}$)	Calc. dn/dT ($\times 10^{-4}, \text{K}^{-1}$)	Exp. dn/dT ($\times 10^{-4}, \text{K}^{-1}$)
1.55	-0.18	-2.88	0.52	2.01
3.39	-0.18	-2.88	0.52	1.48
4.64	-0.18	-2.88	0.51	1.36
10.6	-0.17	-2.88	0.50	1.10

5. Results and Discussions on Bulk Ternary $\text{InAs}_{1-y}\text{P}_y$

Undoped Bulk ternary $\text{InAs}_{1-y}\text{P}_y$ (IAP) polycrystals with diameters up to 50 mm were grown from pseudo-binary InP-InAs melt using the vertical Bridgman technique by United Semiconductor Ltd (USL). In this chapter, $\text{InAs}_{1-y}\text{P}_y$ and its electrical and optical properties are discussed as functions of phosphorus mole fraction and sample temperature. Some of the results were published in [80].

The first section of this chapter begins with a brief introduction regarding $\text{InAs}_{1-y}\text{P}_y$ crystal growth followed by information on the samples used in this investigation. In section two, several visualization techniques are employed to characterize the crystal. From section three and on, discussions will focus on some fundamental yet very important optical and electrical properties of $\text{InAs}_{1-y}\text{P}_y$ crystals.

5.1 Ternary $\text{InAs}_{1-y}\text{P}_y$ Crystal Growth

Undoped melt-grown bulk $\text{InAs}_{1-y}\text{P}_y$ ($0 < y < 1$) polycrystals were grown using the vertical Bridgman technique at United Semiconductor LLC by Geeta Rajapopalan. Here a description of her growth technique is provided for reference.

The compound synthesis and growth were controlled in sealed silica crucibles using pre-synthesized binaries of undoped InP and InAs. Growth temperatures and melt compositions were selected from the pseudo-binary InP-InAs phase diagram reported in the literature [41]. In order to grow a compositionally uniform $\text{InAs}_{1-y}\text{P}_y$ (along the growth direction), excess InP was placed at the top of the melt to provide solute replenishment during crystal growth. First, pre-synthesized polycrystalline ingots of binary InP and InAs were placed inside a flat bottom silica crucible, and the crucible was then evacuated to a

vacuum level of approximately 10^{-6} torr and sealed. No seeds were used in any of the crystal growths. The sealed crucibles were placed inside the uniform temperature zone of the furnace and heated to melt the InAs ingot placed at the bottom of the crucible. The furnace was further slowly heated to the growth temperature (approximately 2-3 °C higher than the liquidus temperature for the desired alloy composition). The InAs acted as the solvent to partially dissolve the InP ingot and form the $\text{InAs}_{1-y}\text{P}_y$ melt. Some portion of the InP ingot remained undissolved and served as the solute replenishment source during the crystal growth process. After the solute dissolution step, the crucible was slowly translated through the temperature gradient of the furnace to implement directional solidification. Typical growth rates were in the range of 0.5-1.0 mm/hr. The entire melt was allowed to solidify and then the grown crystal was cooled to room temperature at a rate of 50 °C/hr. Due to the melt replenishment by the InP feed at the top of the melt, the grown crystals were fairly compositionally homogeneous along the growth direction except at the last two freeze regions. The crystals were also reasonably homogeneous in composition along the radial direction.

A typical crystal boule is shown in Fig. 5.1 (a), which was then sliced by a diamond blade saw to a wafer shown in Fig. 5.1 (b). The surfaces of the wafers were ground using 14 μm boron carbide or silicon carbide abrasives followed by chemo-mechanical polishing using 1 μm and 0.5 μm alumina abrasive slurries. After the final polishing step, high optical quality mirror shining surfaces were obtained. The optical quality of this sample, shown in Fig. 5.1 (c), was imaged using a Santa Barbara Focalplane ImagIR MIR infrared camera. In this picture, the camera was focused on the

ruler placed immediately behind the wafer. Except for some localized dark spots, this figure clearly indicates good infrared optical transmission over the entire wafer.

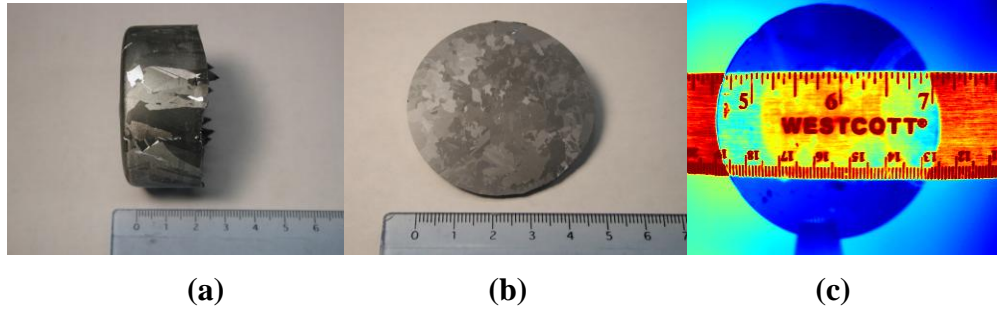
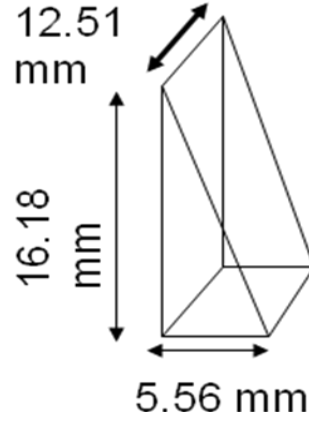


Figure 5.1. (a) Crystal boule, (b) crystal wafer, and (c) MIR image of an $\text{InAs}_{1-y}\text{P}_y$ crystal.

Six $\text{InAs}_{1-y}\text{P}_y$ crystal boules were grown with a different phosphorus mole fraction, ranging from 0.19 – 0.66 by USL in 2009. Then, each boule was used to fabricate a ϕ 25 mm wafer, a square sample with dimensions of 15x15x1 mm, and a right angle prism with prism angle approximately equal to 20° . The prism shape and dimensions are shown in Fig. 5.2. Usually, the circle wafer sample is designed for the PL and a transmission measurement, the square shape sample is designed for the Hall-effect measurement, and the prism is designed for the refractive index measurement. In order to maintain consistency, whenever possible, the same square shape sample was used for PL, transmission, and Hall-effect measurements. The sample names and their compositions are listed in table 5.1. The phosphorus mole fraction compositions were measured using the Cameca SX-100 electron probe micro analyzer. Each composition value was obtained from an average of 16 measurement points, each point covering an approximate $\sim 5 \mu\text{m}^2$ area.

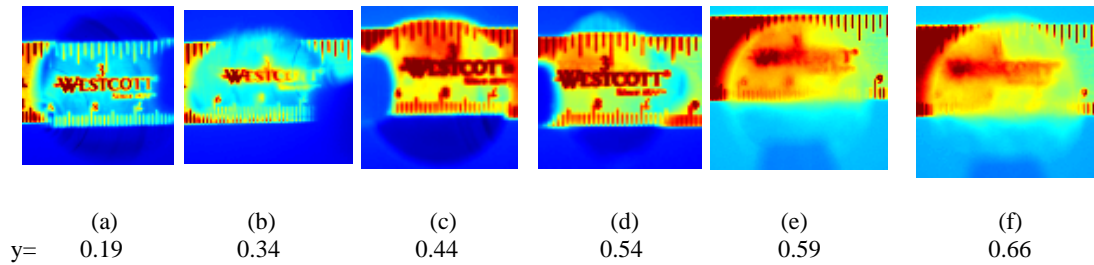
Table 5.1. Bulk ternary InAs_{1-y}P_y sample information

Name	040709B6	040709B3	032009B7	032009B3	020409B7	020409B3
y	0.193 ± 0.008	0.337 ± 0.005	0.441 ± 0.005	0.541 ± 0.004	0.586 ± 0.005	0.659 ± 0.002

**Figure 5.2. Prism used in refractive index measurements using minimum deviation method.**

5.2 Bulk InAs_{1-x}P_y Crystal Images

Bandgap energy of InAs_{1-y}P_y varies from 0.36 to 1.35 eV, corresponding to a cutoff wavelength (λ_c) from 3.44 to 0.92 μm . The MIR Santa Barbara focal plane infrared camera wavelength range is from 3 to 5 μm , which is suitable for full composition range studies for InAs_{1-y}P_y. The IR images of studied samples are shown in Fig. 5.3.

**Figure 5.3. MIR images of InAs_{1-y}P_y crystal samples.**

One can immediately make an initial assessment regarding the crystal's quality by looking at the images shown in Fig. 5.3. For instance, samples (a) and (d) are better optical quality crystals than samples (b) and (c), while samples (e) and (f) show poor optical quality. The optical transmission is a very important property for materials used in optical devices. Poor optical transmission could be due to impurity scattering, crystal defects, as well as inhomogeneity in crystal composition. These negative factors can not only reduce optical transmission, but can also cause serious problems such as phase distortion and reduce the device's efficiency.

By imaging a laser source after passing through a sample, one is able to compare how the sample affects the light (spatial profile). The following investigation is conducted using a pulsed (kHz), frequency doubled Coherent DEOS CO₂ laser with a wavelength of 4.6 μm and maximum power of 2 W. A PyrocamTM III pyroelectric array camera (made by Spiricon Inc.) was used. The recorded images are shown in Fig. 5.4. The first image is the laser beam only, which was imaged without passing through a sample. The second image is the laser beam after passing through an InAs_{1-y}P_y crystal with $y=0$, which is actually a binary crystal (InAs). Therefore, the laser beam quality is unchanged and remains a Gaussian-like beam after passing through the sample, indicating this sample is a high quality crystal. However, as y increases in value, the laser beam quality decreases gradually as shown in Fig. 5.4 (bottom). When the laser beam passes through the sample with $y > 0.53$, it scatters and completely loses its Gaussian beam shape. Finally, when $y=1$ (InP), the laser beam shape is restored and once again it becomes Gaussian-like. This finding is consistent with what we have learned from previous chapters: it is very difficult to grow good quality ternary bulk crystal. This also reveals that it is more

challenging to grow a high quality $\text{InAs}_{1-y}\text{P}_y$ crystal with high phosphorus ($y > 0.34$) composition.

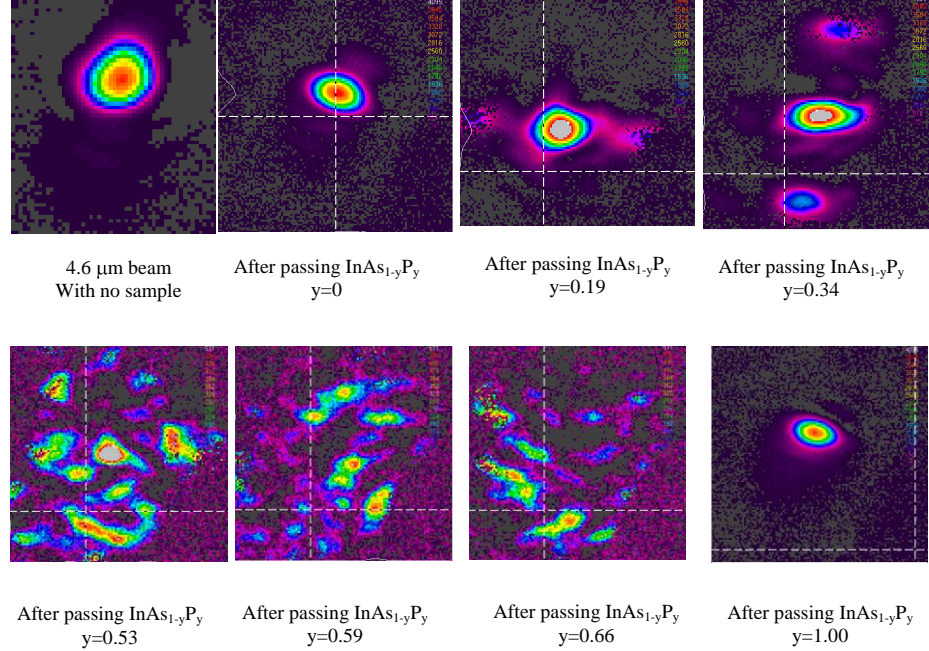


Figure 5.4. Images of a laser beam at 4.6 μm , before or after passing through $\text{InAs}_{1-y}\text{P}_y$ crystals.

This quick screening is necessary and recommended prior to other tests being conducted.

After examining Figs. 5.3 and 5.4 for each wafer, sample $\text{InAs}_{0.81}\text{P}_{0.19}$ was identified as a good quality crystal. PL and refractive index measurements were performed on $\text{InAs}_{0.81}\text{P}_{0.19}$ sample and the results are discussed in the next sections.

5.3 Bandgap Energy of Bulk $\text{InAs}_{1-y}\text{P}_y$

Room temperature transmission spectra of $\text{InAs}_{1-y}\text{P}_y$ samples ($y = 0.19 - 0.66$) were measured using a Perkin Elmer FTIR spectrometer (model Spectrum GX) over the wavelength range of 0.6- 25 μm . Sample thickness is typically 1-1.5 mm and the detailed

composition information is listed in table 5.1. From the transmission spectra shown in Fig. 5.5 (top), each sample has reasonably well defined cutoff wavelength for each phosphorus mole fraction. For a thin film $\text{InAs}_{1-y}\text{P}_y$, the bandgap energy at room temperature was reported [81] as a function of phosphorus mole fraction as

$$E_g(y) = 0.356 + 0.675y + 0.32y^2. \quad (5.1)$$

Bandgap energies of bulk $\text{InAs}_{1-y}\text{P}_y$ crystals to date have not been reported in the literature. In order to obtain the bandgap energy of a bulk $\text{InAs}_{1-y}\text{P}_y$ sample as a function of phosphorus mole fraction, y , directly from the transmission spectra, derivatives of transmission spectra with respect to photon energy were plotted as a function of photon energy as shown in Fig. 5.5 (bottom), from which the $E_{L\min}$, the peak location of dT/dE , was extracted. This method was explained in details in section 4.5.

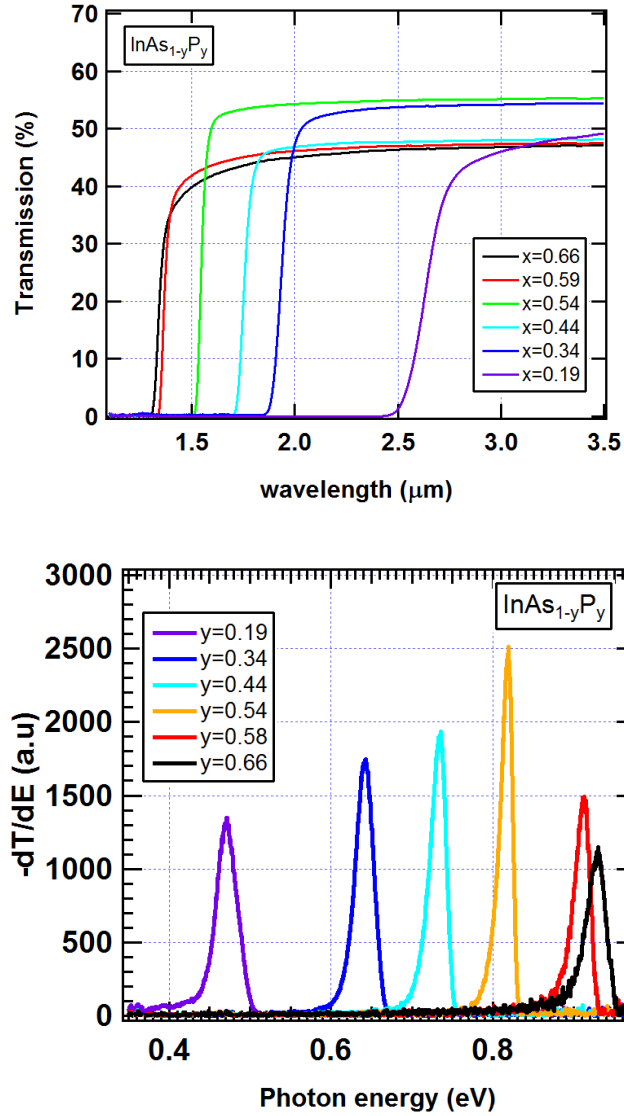


Figure 5.5. (Top) Transmission spectra of six InAs_{1-y}P_y samples with composition ranging from 0.19 to 0.66; (bottom) the 1st derivatives of transmission spectra with respect to photon energy plotted as a function of photon energy.

The obtained $E_{L \min}$ values were plotted as a function of composition in Fig. 5.6 (red dots), along with the bandgap values calculated from thin film results (black solid line) using equation 5.1. The $E_{L \min}$ values generally follow well with the bandgap energies (E_g) that were estimated for the thin epitaxial layers [81].

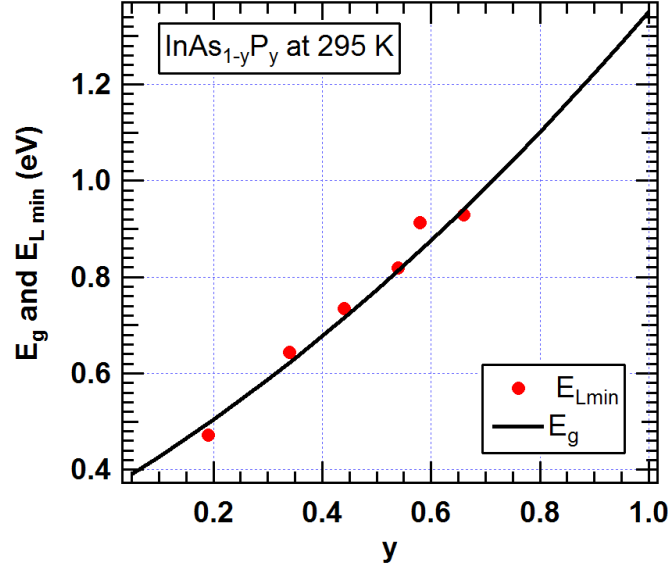


Figure 5.6. $E_{L\min}$ values obtained from transmission spectra (red dots), were plotted as a function of phosphorus composition. The solid line is the bandgap energies of $\text{InAs}_{1-y}\text{P}_y$ calculated from equation 5.1.

Obviously, there are some differences between E_g and $E_{L\min}$ as shown in Fig. 5.6. For example, the $E_{L\min}$ at $y=0.19$ is slightly below the E_g , on the other hand, the $E_{L\min}$ at $y=0.59$ is slightly above the E_g . The difference is about 26 meV. This discrepancy is most likely due to material inhomogeneity and also partly due to the difference between E_g and $E_{L\min}$. Photoluminescence measurement results in the following section will provide further explanations.

5.4 Photoluminescence Measurements

The PL spectra of $\text{InAs}_{0.81}\text{P}_{0.19}$ taken at 10 K with a laser excitation power of 100 mW at different sample locations are shown in Fig. 5.7. Five selected locations on the $\text{InAs}_{0.81}\text{P}_{0.19}$ sample are indicated on top right in Fig. 5.7.

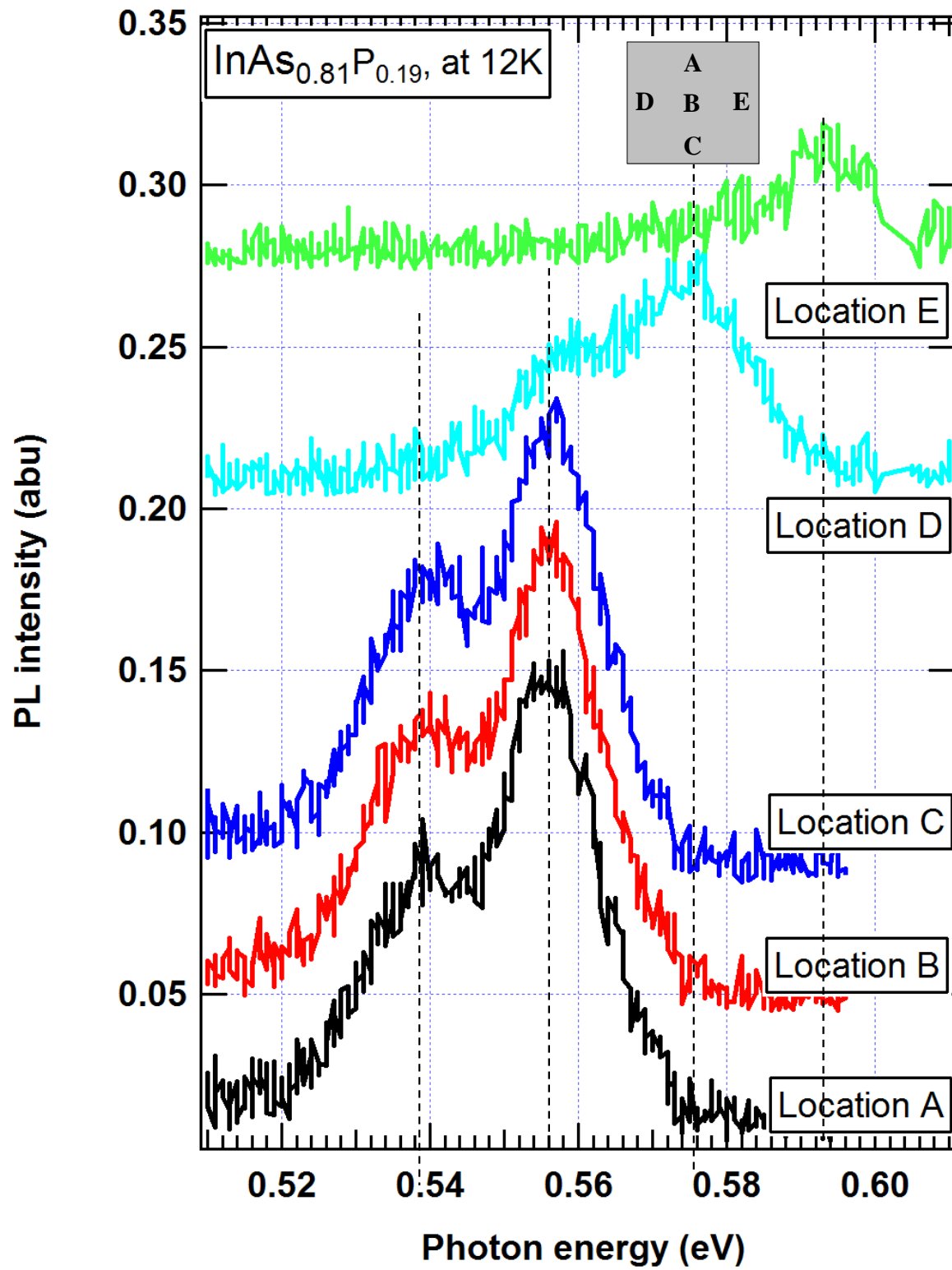


Figure 5.7. Location dependent PL spectra of an $\text{InAs}_{0.81}\text{P}_{0.19}$ sample taken at 12 K with a laser excitation power of 300 mW.

PL peak positions are clearly dependent on the sample position indicating sample nonuniformity. This shows high sensitivity of PL measurement. Normalized PL spectra mainly consist of two peaks which are attributed to the free exciton (FX) and donor-acceptor pair (DAP) transitions. The FX peak locations shown in Fig. 5.7 are 0.556, 0.575, and 0.594 eV, showing a variation of 38 meV. These PL results indicate a compositional variation of approximately 4.8% across the sample, which is about 6× larger than the findings listed in table 5.1 from a micro probe analyzer. This composition variation within the sample may explain some of the discrepancies between $E_{L\min}$ and E_g observed in Fig. 5.6.

Power dependent PL spectra were also measured at 12 K for the $\text{InAs}_{0.81}\text{P}_{0.19}$ sample, and the results are shown in Fig. 5.8. At a lower power level (at or below 200 mW), the dominant PL peak is at 0.540 eV (indicated as B in Fig. 5.8). As the excitation power is increased to above 200 mW, the peak A becomes gradually dominant. These excitation power-dependent PL results can be used to identify the origin of the transition because the relationship between the integrated PL peak intensity and the laser excitation power is dependent on the nature of the PL transition [82]. A linear relationship between the excitation power and the integrated PL intensity indicates an excitonic recombination; a sub-linear relationship indicates a defect or impurity related transition, and a quadratic dependence indicates a band-to-band transition [83, 84].

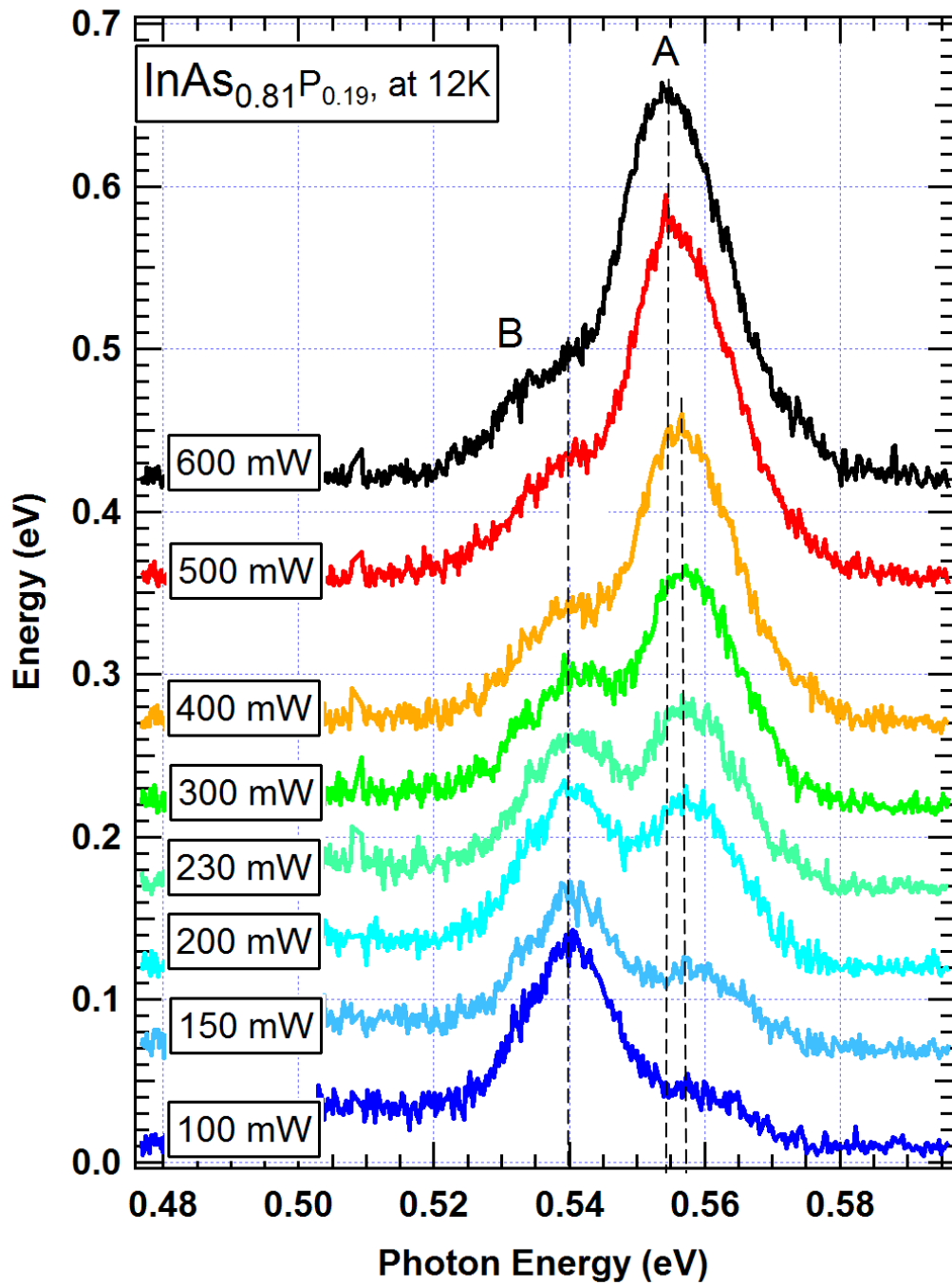


Figure 5.8. Photoluminescence spectra of $\text{InAs}_{0.81}\text{P}_{0.19}$ sample measured at 12 K with different incident laser powers.

The integrated PL intensity of the $\text{InAs}_{0.81}\text{P}_{0.19}$ sample was plotted as a function of excitation power in Fig. 5.9. The integrated PL intensities along with a full width at half maximum (FWHM) for both peaks A and B were estimated from a Gaussian peak fitting of curves. Since the integrated PL intensity of peak A clearly shows a linear dependence on excitation power, the luminescence peak A is attributed to an excitonic recombination. On the other hand, the integrated PL intensity of peak B clearly shows a sub-linear relationship with excitation power, which indicates that the peak B can be attributed to a DAP transition.

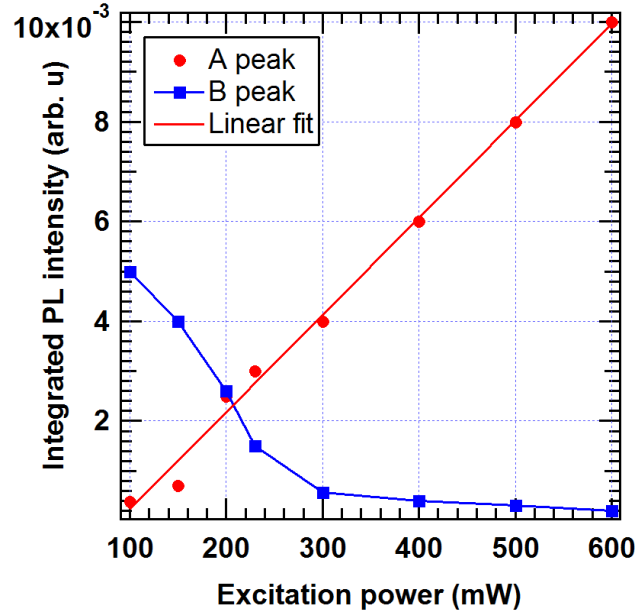


Figure 5.9. Integrated photoluminescence intensities of peaks A and B for $\text{InAs}_{0.81}\text{P}_{0.19}$ sample measured at 12 K plotted as a function of excitation power.

The PL spectra from spot B (indicated in Fig. 5.7, top right) was investigated at various temperatures with a laser power of 300 mW as shown in Fig. 5.10.

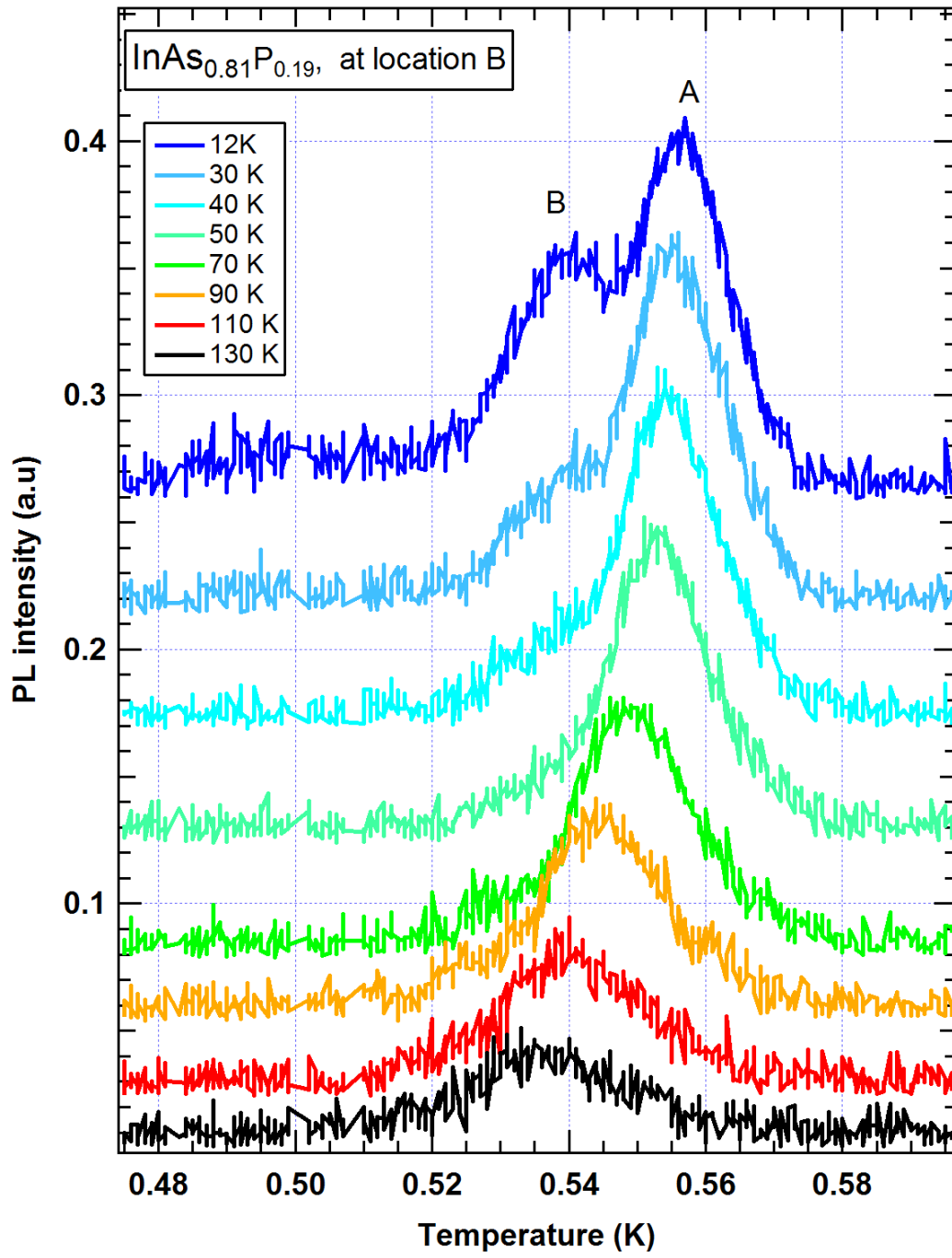


Figure 5.10. Temperature dependent PL spectra of the $\text{InAs}_{0.81}\text{P}_{0.19}$ with a laser power of 300 mW.

The donor to acceptor pair transition peak at 0.540 eV was observed at 12 K, but this peak disappeared after the temperature was raised greater than 30 K. The FX peak red-shifts when the temperature increases. This is due to bandgap shrinkage by the crystal lattice expansion and the increase in lattice vibration in the crystal. The FX peak positions are red-shifted by approximately 40 meV as the temperature is increased from 12 to 130 K.

The FX peak energies (red data points) versus temperature for the $\text{InAs}_{0.81}\text{P}_{0.19}$ sample are shown in Fig. 5.11 along with the $E_{L \min}$ (black squares) obtained from the transmission spectra. They seem to follow each other very well, indicating similar temperature dependencies. Since the free exciton binding energy is assumed to be very small (InP is ~ 3.5 meV, GaAs is ~ 1.5 meV, and InAs is ~ 1.3 meV.) [69, 85], FX can be approximately considered as the bandgap energy. However, the existing inhomogeneity in the sample greatly complicates the problem. Note that these FX peaks were taken at the sample location B (shown in Fig. 5.7), where the FX peak value is smaller than other locations in the sample. The variation in energy between locations B and D is about 24 meV, and between locations B and E is ~ 37 meV.

On the other hand, $E_{L \min}$ should always be below the bandgap. From the discussion in section 4.5, for a 1 mm thick InAs, the difference between E_g and $E_{L \min}$ at room temperature is ~ 30 meV, and is ~ 57 meV for InP.

At room temperature, the composition dependent bandgap energy of ternary $\text{InAs}_{1-y}\text{P}_y$ thin film is mostly known [81]. If bulk $\text{InAs}_{1-y}\text{P}_y$ has the same bandgap energy as that of the thin film, the bandgap of $\text{InAs}_{1-y}\text{P}_y$ at $y=0.19$ can be calculated using

equation 5.1. Since the difference ($E_g - E_{L \min}$) was found to be 22 meV.

$$E_g = E_{L \min} + \theta \sqrt{T}, \text{ and } \theta = 0.00125 \text{ eVK}^{-0.5} \text{ is obtained.}$$

The temperature dependent E_g then can be calculated from $E_{L \min}$ as shown in Fig. 5.11 (blue triangles). The obtained E_g value are curve fitted using the Varshni's equation (equation 2.5), the results are shown in Fig.5.12 as a solid curve. The empirical Varshni coefficients for $\text{InAs}_{0.81}\text{P}_{0.19}$ sample are found to be $E_g(0) = 0.564 \text{ eV}$, $\alpha = 0.450 \text{ meV/K}$, and $\beta = 300 \text{ K}$.

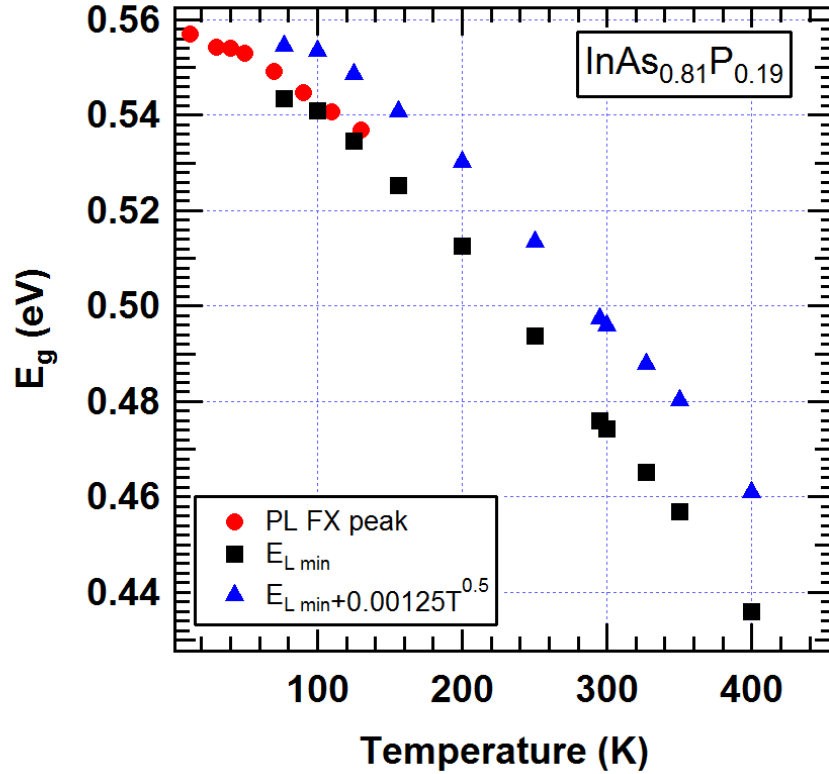


Figure 5.11. FX peak of $\text{InAs}_{0.81}\text{P}_{0.19}$ (red) and $E_{L \min}$ (black) vs. Temperature. E_g (blue) is calculated using equation $E_g = E_{L \min} + \theta \sqrt{T}$.

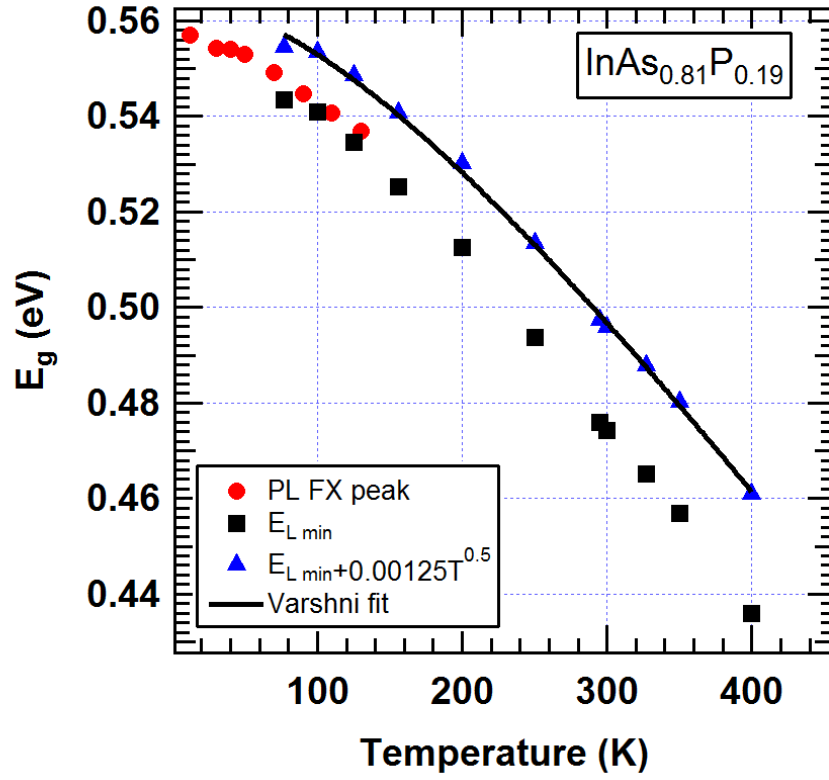


Figure 5.12. FX peak (red dots) and $E_{L \min}$ (black) of $\text{InAs}_{0.81}\text{P}_{0.19}$ vs. Temperature. E_g is calculated using Eq. $E_g = E_{L \min} + \theta\sqrt{T}$ (blue), and the Varshni equation is a solid black line.

Several other $\text{InAs}_{1-y}\text{P}_y$ samples with different compositions were also studied. Their temperature dependent bandgap energies were obtained using temperature dependent PL and transmission spectra but are not shown here. Composition dependent Varshni coefficients were obtained and they are summarized in table 5.2.

Table 5.2. Summary of composition dependent Varshni coefficients for $\text{InAs}_{1-y}\text{P}_y$

Composition y	$E_g(0)$	$\alpha (\times 10^{-4})$ eV/K	β (K)	dE_g/dT from linear fit $\times 10^{-4} (\text{eVK}^{-1})$
0.00	0.415	2.76	83	-2.4314
0.19	0.564	4.50	300	-2.7482
0.24	0.611	5.09	300	-3.1085
0.34	0.704	5.19	300	-3.1696
1.00	1.421	4.90	327	-2.8788

Results of temperature dependent bandgap energy of $\text{InAs}_{1-y}\text{P}_y$ are plotted as a function of temperature in Fig. 5.13.

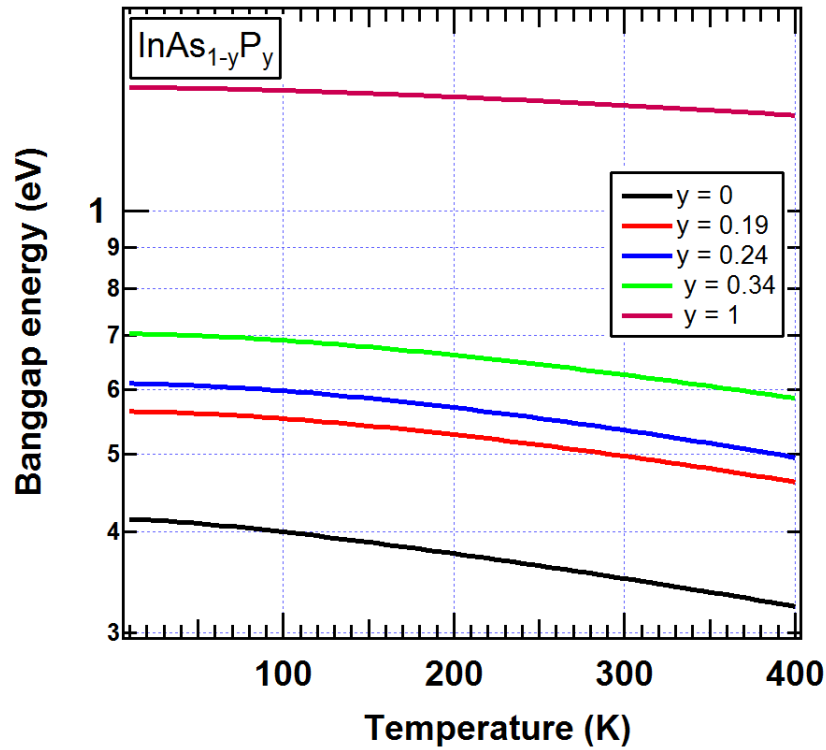


Figure 5.13. Temperature dependent bandgap energy of $\text{InAs}_{1-y}\text{P}_y$.

5.5 Refractive Index Measurements

The refractive index of the $\text{InAs}_{0.81}\text{P}_{0.19}$ crystal was measured as functions of wavelength and temperature, and the results are plotted in Fig. 5.14. At all three wavelengths, the refractive index varied linearly in the temperature range between 90 K and 295 K according to the following relationships:

$$n \text{ at } 3.39 \mu\text{m} = 3.3193 + 2.13 \times 10^{-4}T,$$

$$n \text{ at } 4.64 \mu\text{m} = 3.3106 + 1.94 \times 10^{-4}T,$$

$$n \text{ at } 10.6 \mu\text{m} = 3.2844 + 1.81 \times 10^{-4}T.$$

Fig. 5.15 shows the wavelength dependent refractive indices for $\text{InAs}_{0.81}\text{P}_{0.19}$ measured at various temperatures. The dashed lines are curve-fitted at each temperature for different photon wavelengths (λ) using the Cauchy equation,

$$n(\lambda, T) = A(T) + \frac{B(T)}{\lambda^2} + \frac{C(T)}{\lambda^4}. \quad (5.2)$$

The estimated values of Cauchy coefficients, $A(T)$, $B(T)$, and $C(T)$ are listed in table 5.3 for the $\text{InAs}_{0.81}\text{P}_{0.19}$ alloy, along with the measured values for the binary InAs ($y=0$) and InP ($y=1$).

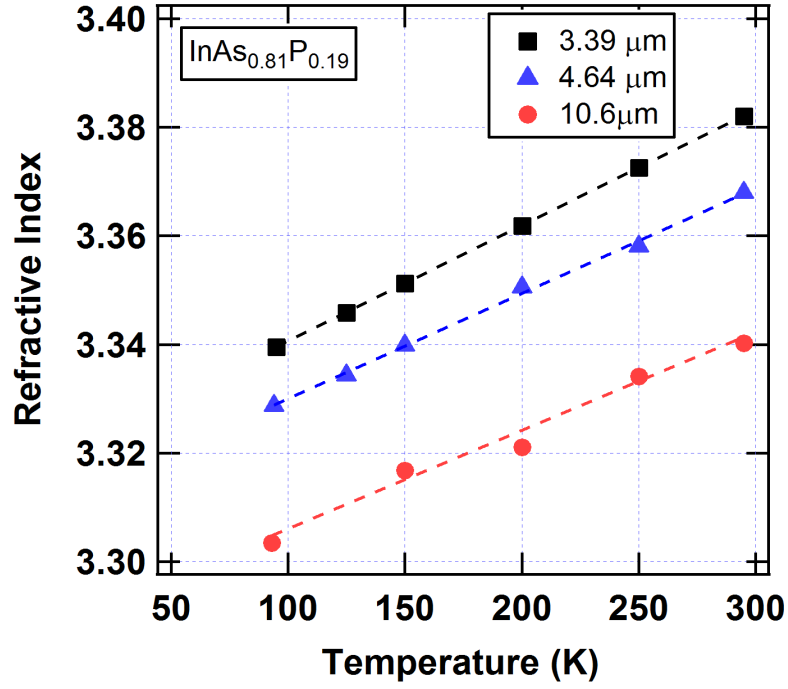


Figure 5.14. Refractive index of $\text{InAs}_{0.81}\text{P}_{0.19}$ alloy as a function of temperature.

Table 5.3. Temperature dependent Cauchy coefficients for $\text{InAs}_{1-y}\text{P}_y$ alloy

y	A (T)	B(T) (μm^2)	C(T) (μm^4)
0	$3.4097+2.40\times 10^{-4}\text{T}$	$1.175+3\times 10^{-5}\text{T}$	$0.50+3.14\times 10^{-2}\text{T}$
0.19	$3.2816+1.79\times 10^{-4}\text{T}$	$0.756+2.7\times 10^{-4}\text{T}$	$-3.70+1.4\times 10^{-3}\text{T}$
1	$2.9886+1.01\times 10^{-4}\text{T}$	$1.366+1.02\times 10^{-3}\text{T}$	$-7.27-5.6\times 10^{-3}\text{T}$

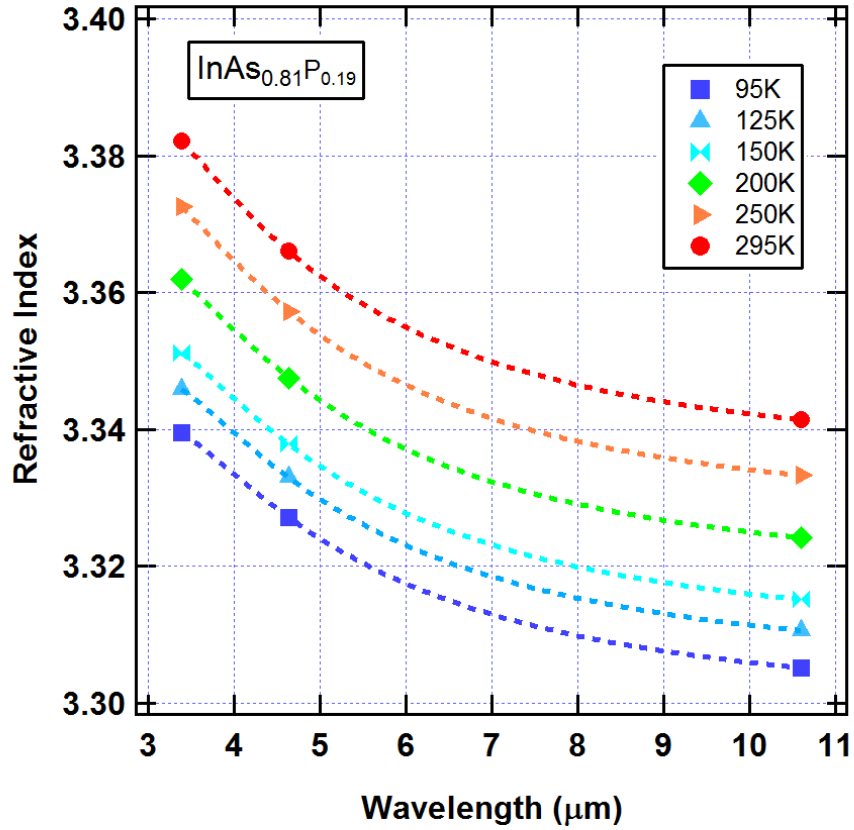


Figure 5.15. Refractive index of $\text{InAs}_{0.81}\text{P}_{0.19}$ alloy as a function of wavelength.

Refractive indices of $\text{InAs}_{1-y}\text{P}_y$ alloys versus full composition at a wavelength of $4.6\ \mu\text{m}$ and at two temperatures (95 and 295K) are shown in Fig. 5.16. Refractive indices at other wavelengths (3.39 and $10.6\ \mu\text{m}$) were also obtained but are not shown here. Refractive indices at $3.39\ \mu\text{m}$ are slightly greater than those measured at $4.6\ \mu\text{m}$, and the results at $4.6\ \mu\text{m}$ are greater than those measured at $10.6\ \mu\text{m}$. However, the difference from different wavelengths is not significant compared to the variations in indices from different compositions.

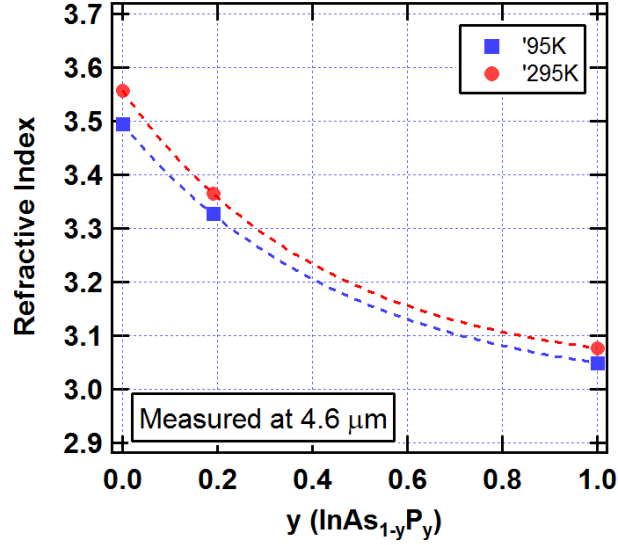


Figure 5.16. Refractive Index of $\text{InAs}_{0.81}\text{P}_{0.19}$ measured at $4.6 \mu\text{m}$, and at 95 K and 295 K as a function of composition.

Earlier work in ternary material properties was based on using linear proportionality with respect to binary semiconductors [42, 43], and adding the bowing factor by using quadratic terms. But this method does not apply to the composition-dependent refractive index of $\text{InAs}_{0.81}\text{P}_{0.19}$ alloy. From Fig. 5.16, the best fit function is an exponential function, which can be expressed as

$$n = 3.0255 + 0.5313e^{-2.340y} \quad \text{at 295 K and at } 4.6 \mu\text{m} \quad (5.3)$$

$$n = 2.9883 + 0.5065e^{-2.116y} \quad \text{at 95 K and at } 4.6 \mu\text{m} \quad (5.4)$$

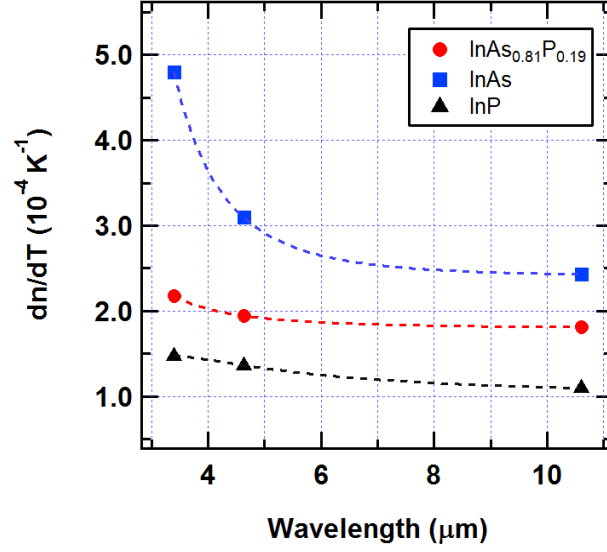


Figure 5.17. Measured dn/dT values of $\text{InAs}_{1-y}\text{P}_y$ alloy for $y=0.00$, $y=0.19$, and $y=1.00$.

The dn/dT of the $\text{InAs}_{1-y}\text{P}_y$ alloy measured as a function of composition at a wavelength of $4.6 \mu\text{m}$ is shown in Fig. 5.17. For the $\text{InAs}_{0.81}\text{P}_{0.19}$ alloy, a comparison between theoretical dn/dT and experimental dn/dT was made at three wavelengths as shown in table 5.4.

Table 5.4. Comparison of theoretical and experimental dn/dT for $\text{InAs}_{0.81}\text{P}_{0.19}$ alloy

Photon wavelength	dn/dE_g (eV^{-1})	dE_g/dT $\times 10^{-4}$ (eVK^{-1})	Calc. dn/dT $\times 10^{-4}$ (K^{-1})	Exp. dn/dT $\times 10^{-4}$ (K^{-1})
3.39	-0.62	-2.75	1.69	2.13
4.64	-0.46	-2.75	1.25	1.94
10.6	-0.37	-2.75	1.03	1.81

From table 5.4, one observes that the experimental dn/dT is always greater than the theoretically predicted values for dn/dT . This is mainly due to the fact that when dn/dE_g was evaluated, the effective mass of InAs was used because the electron and hole

effective mass of the $\text{InAs}_{0.81}\text{P}_{0.19}$ alloy were not available. This may result in an inaccurate calculation of dn/dE_g for $\text{InAs}_{0.81}\text{P}_{0.19}$, and in turn an inaccurate dn/dT .

5.6 Hall-effect Measurements

Square-shaped samples of $\text{InAs}_{1-y}\text{P}_y$ crystals with dimensions of 15x15x1mm were used for the Hall-effect measurements. The ohmic contacts were placed on the periphery of the sample using indium. Hall-effect measurements were conducted at 77 and 300 K under a magnetic field of 5 kG for the samples listed in table 5.1. Carrier concentration and mobility were studied as functions of composition and temperature, and the results are shown in Fig. 5.18.

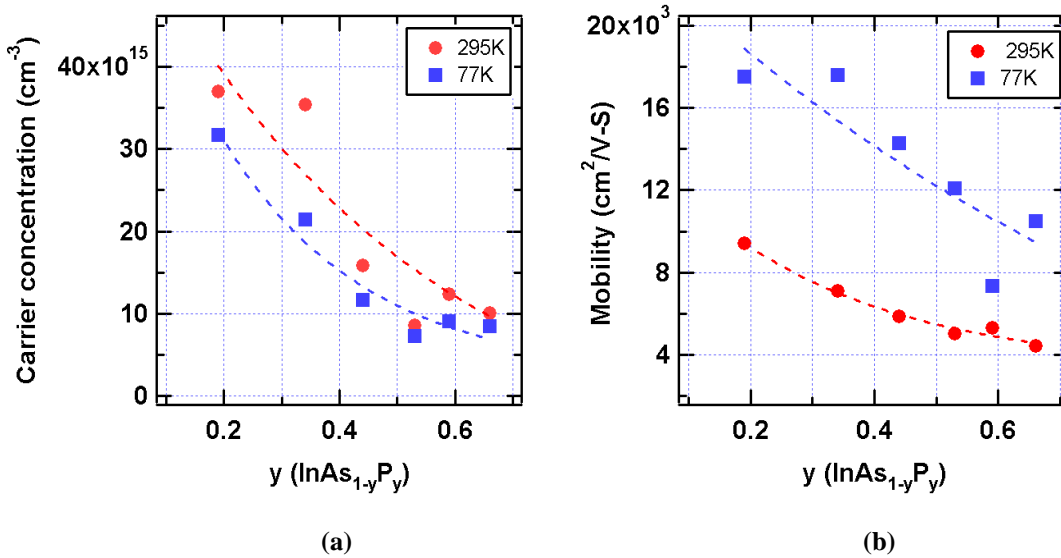


Figure 5.18. Hall-effect measurement data at 77 and 295 K for various $\text{InAs}_{1-y}\text{P}_y$ samples as a function of phosphorus mole fraction: (a) carrier concentration and (b) Hall mobility.

All samples were found to exhibit n-type conductivity, possibly due to residual impurities, native defects such as arsenic and phosphorus vacancies, and/or their antisites in indium. Both carrier concentrations (Fig. 5.18 (a)) and mobilities (Fig. 5.18 (b))

generally decrease with phosphorus mole fraction due to an increase in bandgap. High carrier mobility of $\sim 9,500 \text{ cm}^2/\text{V}\cdot\text{s}$ at 295 K for the $\text{InAs}_{0.81}\text{P}_{0.19}$ sample is an indication of good crystal quality. The room temperature resistivity changed from approximately $0.02 \text{ }\Omega\cdot\text{cm}$ to $0.14 \text{ }\Omega\cdot\text{cm}$ as the phosphorus mole fraction changed from 0.19 to 0.66 (not shown here).

Temperature-dependent Hall-effect measurements were also carried out from 20 to 310 K for $\text{InAs}_{0.9}\text{P}_{0.1}$ sample as shown in Fig. 5.19.

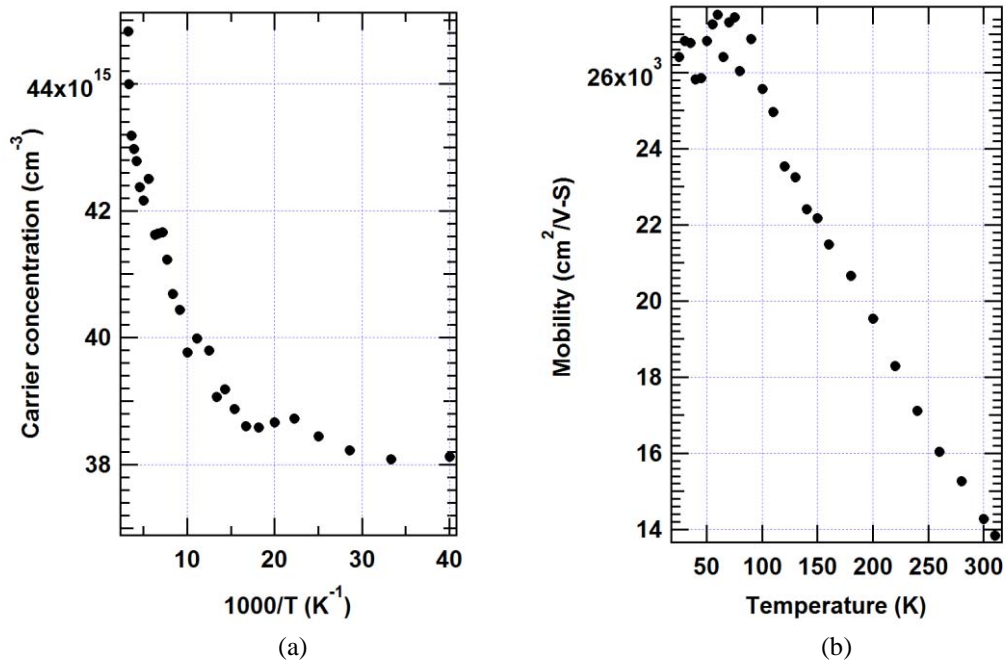


Figure 5.19. Temperature dependent Hall-effect measurements for the $\text{InAs}_{0.9}\text{P}_{0.1}$ from 20 to 310 K.

The carrier concentration is $\sim 3.8 \times 10^{16} \text{ cm}^{-3}$ at 20 K, and it remains almost constant up to approximately 30 K and then increases as the temperature is increased further up to room temperature. This is possibly due to the carriers from ionized shallow donors below about 30 K, but above 30 K, the carriers from ionized deep donors become

dominant in the conduction band. The mobility remains about the same at temperatures up to 50 K and then increases due to screening of ionized impurity scattering and/or alloy disorder scattering. The mobility is $2.8 \times 10^4 \text{ cm}^2/\text{V}\cdot\text{s}$ at 75 K, and then decreases as the sample temperature is increased to 310 K due to increase in optical phonon lattice scattering at higher temperatures.

6. Results and Discussions on Bulk Ternary $\text{In}_x\text{Ga}_{1-x}\text{As}$

Undoped bulk melt-grown $\text{In}_x\text{Ga}_{1-x}\text{As}$ was fabricated using the vertical Bridgman technique by United Semiconductor LLC. The electrical and optical properties of $\text{In}_x\text{Ga}_{1-x}\text{As}$ were investigated as functions of indium mole fraction and sample temperature in a similar manner to those of $\text{InAs}_{1-y}\text{P}_y$ in chapter 5, some of the results are accepted for publish [86]. The optical properties of interest include bandgap energies and refractive index, and the electrical properties include carrier concentration, mobility, and resistivity.

A systematic measurement of PL was carried out in order to gain insight into the various radiative transitions in the $\text{In}_x\text{Ga}_{1-x}\text{As}$ crystal. The discussions include PL measurements as functions of temperature, laser excitation power, and sample location.

6.1 Ternary $\text{In}_x\text{Ga}_{1-x}\text{As}$ Crystal Growth

Undoped bulk $\text{In}_x\text{Ga}_{1-x}\text{As}$ ($0 \leq x \leq 1$) polycrystals were grown using a multi-zone vertical gradient freezing furnace at United Semiconductor LLC by Geeta Rajapopalan. Here a description of her growth technique is provided for reference.

Melt synthesis was carried out using 6N purity polycrystalline GaAs and InAs as the starting material. Appropriate mole fractions of InAs and GaAs were used according to the liquidus composition which corresponded to a desirable crystal composition. The synthesis and growth was conducted in a sealed silica crucible with a vacuum level of 10^{-7} Torr. During the InGaAs synthesis, the molten InAs and GaAs mixtures were vigorously mixed by periodically tilting the crucible along with the furnace. Typical synthesis duration was in the range of 1-2 hours. Following synthesis, the melt was directionally cooled to grow the crystal at a rate of 1 mm/hr. The temperature gradient near the melt-solid interface during

the growth was maintained in the range of 5-10 °C/cm. After the entire melt had solidified, the crystal was cooled at a rate of 50 °C/hr to room temperature. During this process, the melt composition continuously changed for grading the alloy composition of the crystal. In order to grow a homogeneous crystal of a specific composition, the melt needs to be maintained at a constant composition throughout the growth. In these processes, precise control over the solute feeding process and melt composition is necessary [41].

In addition, there are other important parameters that must also be used to obtain crystals with high optical and electrical properties. These growth parameters include: usage of melt encapsulation, vapor pressure control for group V volatile species, crucible material and post growth crystal annealing. Post growth cooling cycles for ternary crystals also needs to be optimized. Faster cooling rates could lead to the thermal strain, inducing cracks in the wafers during processing.

After growth, the $\text{In}_x\text{Ga}_{1-x}\text{As}$ crystal's boule was obtained (shown in Fig. 6.1 (a)) and then sliced into wafers (shown in Fig. 6.1 (b)) using a diamond blade saw. The surfaces of the wafers were ground using 14 μm boron carbide or silicon carbide abrasives followed by chemo-mechanical polishing using 1 μm and 0.5 μm alumina abrasive slurries. After the final polishing step, high quality optical surfaces were obtained.

The optical quality is qualitatively checked using a Santa Barbara Focalplane ImagIR MIR infrared camera. A typical MIR image of $\text{In}_x\text{Ga}_{1-x}\text{As}$ is shown in Fig. 6.1 (c). Each $\text{In}_x\text{Ga}_{1-x}\text{As}$ wafer has dimensions of a ~50 mm diameter and a ~2 mm thickness. Samples selected for Hall-effect measurements were sent back to USL to thin and cut down to dimensions of 10x10x0.5 mm. Unlike $\text{InAs}_{1-y}\text{P}_y$, all refractive index measurements of $\text{In}_x\text{Ga}_{1-x}\text{As}$ crystals were carried out using Michelson and Fabry-Perot

interferometers because an $\text{In}_x\text{Ga}_{1-x}\text{As}$ prism was not available. The Michelson and Fabry-Perot method provides two results: the refractive index and the thickness of a wafer.

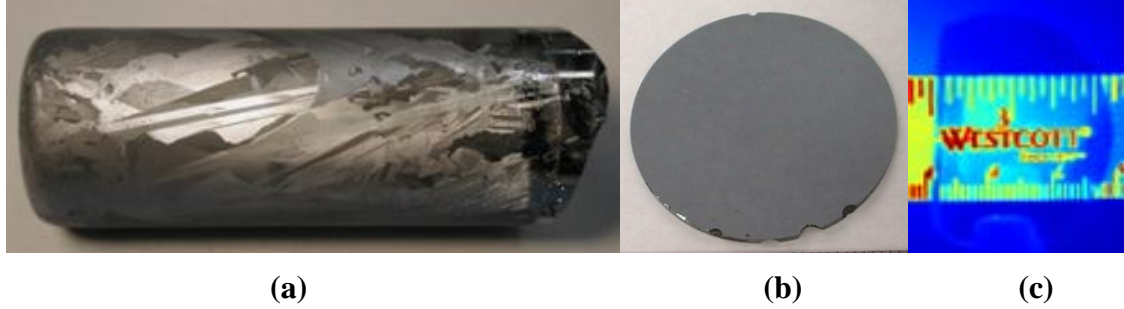
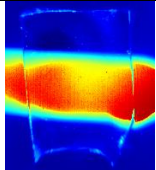
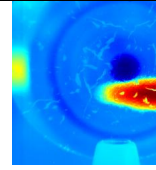
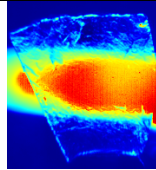
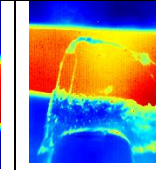
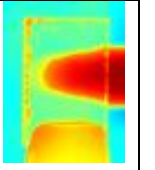


Figure 6.1. Crystal boule (a), crystal wafer (b), and Mid IR image of $\text{In}_x\text{Ga}_{1-x}\text{As}$ (c).

6.2 Bandgap Energy of Bulk $\text{In}_x\text{Ga}_{1-x}\text{As}$

Five $\text{In}_x\text{Ga}_{1-x}\text{As}$ crystals with different indium mole fractions are listed in table 6.1. The indium mole fractions were measured using a Cameca SX-100 electron probe micro analyzer. Each composition value was obtained from an average of 16 measurement points, each point covering an approximate $\sim 5 \mu\text{m}^2$ area. Infrared images through the samples taken with an infrared camera are provided in table 6.1 (A hot soldering iron was placed behind the sample.) along with other sample information. In table 6.1, binary crystals ($x=0$, and $x=1$) are single crystals. They have perfect optical transparency and uniformity. The remaining samples ($x=0.75$, 0.82 and 0.93) are polycrystalline (Note the textures apparent in the MIR images.). Even though these polycrystalline samples show some cloudy spots due to defects, they show generally good optical transmission.

Table 6.1. Various $\text{In}_x\text{Ga}_{1-x}\text{As}$ crystals

Name	GaAs 127-24-4	IGA 041506-1	IGA 052406-1	IGA 052406-4	InAs WT 524-10
y	0.000	0.751 ± 0.004	0.821 ± 0.005	0.926 ± 0.002	1.000
Thickness at 295 K	0.617	1.653	1.004	1.300	1.004
Thickness at 100 K	0.616	1.648	1.001	1.296	1.001
MIR images					

Room temperature transmission spectra of these $\text{In}_x\text{Ga}_{1-x}\text{As}$ samples are measured using the Perkin Elmer Spectrum GX (FTIR spectrometer), and the results are shown in Fig. 6.2 (top). Derivatives of transmission spectra with respect to photon energy were plotted as a function of photon energy as shown in Fig. 6.2 (bottom). $E_{L \min}$ values were determined from the peak locations of Fig. 6.2. $E_{L \min}$ is known to be equal to E_g if the sample thickness reaches zero (see chapter 4). For a sample having a thickness > 1 mm, the difference of $(E_g - E_{L \min})$ is approximately a constant. For InAs, this constant is approximately ~ 30 meV at room temperature, and ~ 45 meV for GaAs. For $\text{In}_x\text{Ga}_{1-x}\text{As}$, this constant should be contributed from both InAs and GaAs, and could be proportional to its composition. This leads to a correction factor that is equal to $(x \cdot 0.030 + (1-x) \cdot 0.045)$ eV, and this value can be added to $E_{L \min}$ to obtain an approximate value of the bandgap energy. The results were plotted in Fig. 6.3, along with the thin film bandgap energies calculated using equation 6.1 [81]:

$$E_g(x) = 0.356 + 0.7(1-x) + 0.4(1-x)^2. \quad (6.1)$$

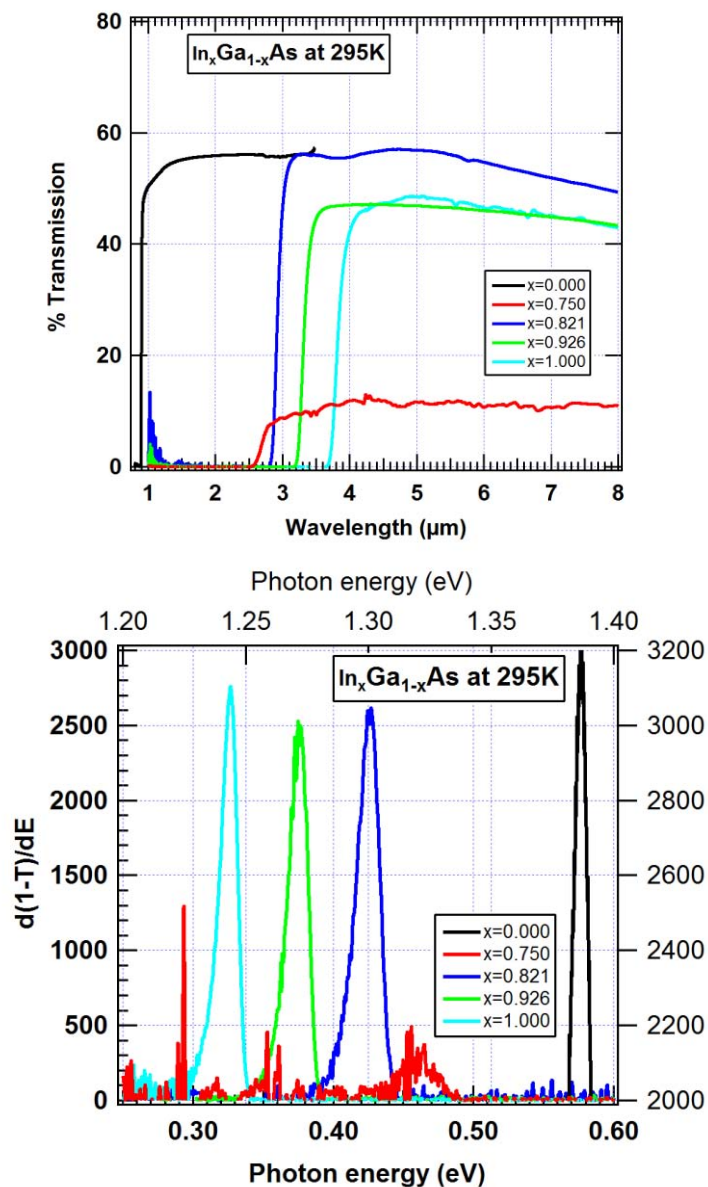


Figure 6.2. (Top) Room temperature transmission spectra of various $\text{In}_x\text{Ga}_{1-x}\text{As}$ samples. (Bottom) First derivatives of transmission spectra with respect to photon energy plotted as a function of photon energy. For $x = 0$, the peak position should be read from the top horizontal scale, and for the rest of $x \geq 0.75$, the peak positions should be read from the bottom horizontal scale.

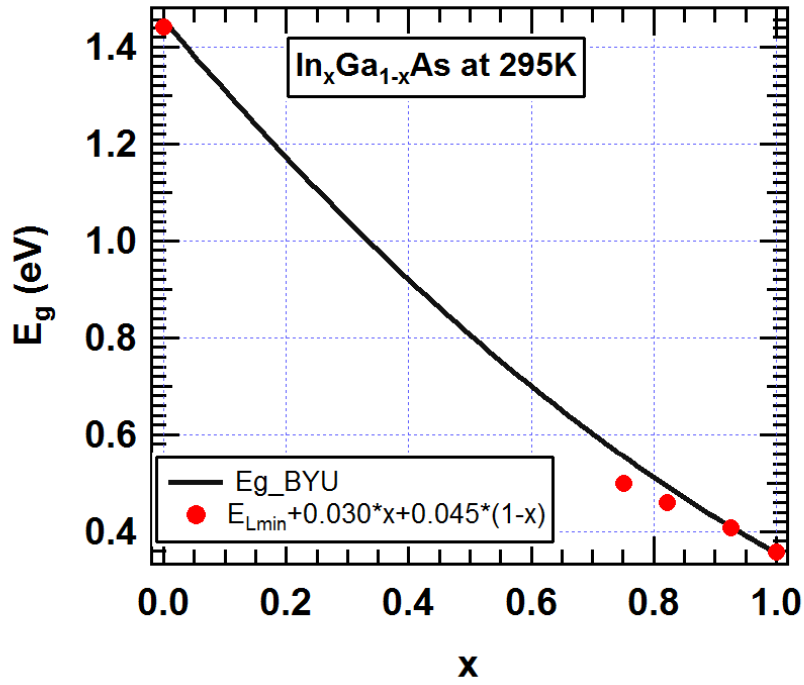


Figure 6.3. The estimated bandgap energy $E_g = (E_{L\ min} + 0.03x + 0.045(1-x))$ from transmission spectra (red dot) for $\text{In}_x\text{Ga}_{1-x}\text{As}$ plotted as a function of In mole fraction. The solid curve represents banggap energies obtained from the published thin film E_g equation.

From Fig. 6.3, one can see that the bandgap energy extracted from transmission spectrum follows well with the published thin film bandgap energy.

6.3 Photoluminescence Studies

Photoluminescence spectra of $\text{In}_x\text{Ga}_{1-x}\text{As}$ samples were measured as functions of sample location, indium composition, laser incident power and temperature. The experimental setup and conditions are similar to those PL studies described in chapter 5.

6.3.1 Sample Location Dependent PL Measurements

PL spectra of $\text{In}_{0.75}\text{Ga}_{0.25}\text{As}$ sample were taken at a temperature of 10 K with a laser excitation power of 100 mW at different sample locations, and the results are shown in Fig. 6.4. The three selected locations are indicated at the top right corner in Fig. 6.4. It can be seen that the PL peak positions are clearly dependent on sample positions. Despite the variations in peak location, all three PL spectra are composed of one broad peak, which is believed to be a band to band transition. The broadening may be due to impurities and defects in the crystal. The peak positions at the three different sample locations are 0.561, 0.548 and 0.534 eV, and the maximum difference is 27 meV for this $\text{In}_{0.75}\text{Ga}_{0.25}\text{As}$. This maybe due to a composition gradient during crystal growth that probably contributed by heat gradient. The indium mole fraction variation is $\sim 3\%$. This finding is consistent with previous findings of bandgap energies determined by transmission spectra that are described in section 6.2.

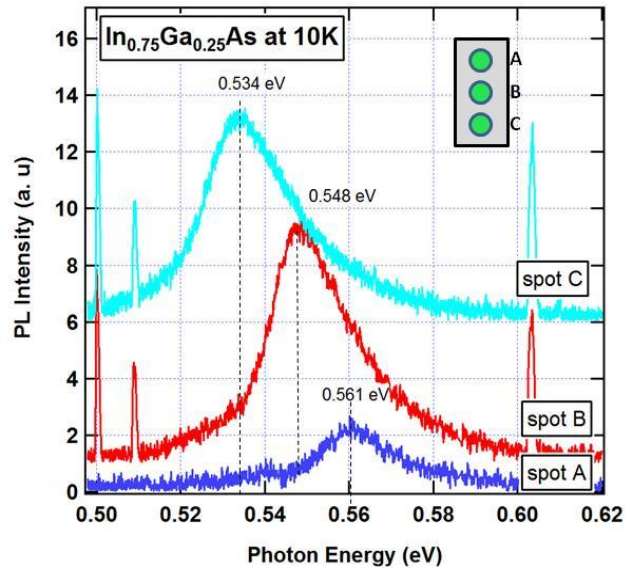


Figure 6.4. Location dependent photoluminescence spectra of $\text{In}_{0.75}\text{Ga}_{0.25}\text{As}$ measured at 12 K with laser incident excitation power of 300 mW.

Sample position dependent PL spectra of $\text{In}_{0.82}\text{Ga}_{0.18}\text{As}$ sample were also measured and the results are plotted in Fig. 6.5. The PL measurements were conducted at 12 K with a laser power of 100 mW. The PL spectra shown in Fig. 6.5 are composed of two strong peaks indicated by A and B, which correspond to the free exciton and the donor to acceptor pair transitions, respectively. A very weak third PL peak is also visible in the low energy region of the PL spectrum.

As seen from Fig. 6.5, the PL peak positions are clearly sample position dependent. The maximum difference in the FX peak energy is about 7 meV, which indicates about 1% indium composition variation. This variation is much smaller than those found in sample $\text{In}_{0.75}\text{Ga}_{0.25}\text{As}$ sample, demonstrating that $\text{In}_{0.82}\text{Ga}_{0.18}\text{As}$ sample has better uniformity than the $\text{In}_{0.75}\text{Ga}_{0.25}\text{As}$ sample. Other observations also support this conclusion. Firstly, the FX peak is observed for $\text{In}_{0.82}\text{Ga}_{0.18}\text{As}$ sample as shown in Fig. 6.5. On the other hand, a broad B-B peak is observed for $\text{In}_{0.75}\text{Ga}_{0.25}\text{As}$ sample as shown in Fig. 6.4. In general, the FX peak can only be seen in pure crystals (see chapter 2). Secondly, the $\text{In}_{0.82}\text{Ga}_{0.18}\text{As}$ sample has higher optical transmission (~4.5 times) than $\text{In}_{0.75}\text{Ga}_{0.25}\text{As}$ sample as shown in Fig. 6.2 (a). Finally, IR images listed in table 6.1 show that the $\text{In}_{0.75}\text{Ga}_{0.25}\text{As}$ sample has more localized defect spots than the $\text{In}_{0.82}\text{Ga}_{0.18}\text{As}$ sample.

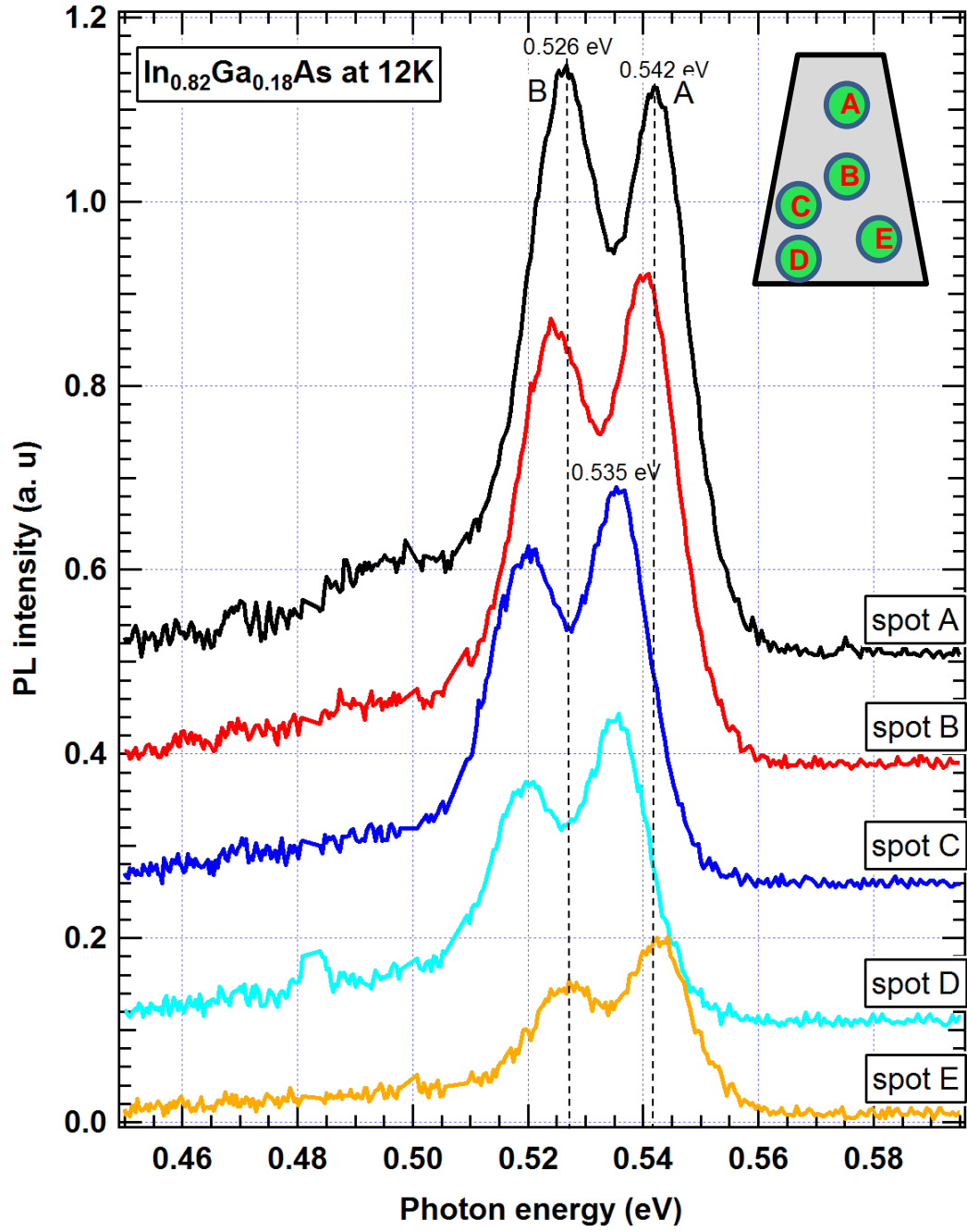


Figure 6.5. Position-dependent photoluminescence spectra for the $\text{In}_{0.82}\text{Ga}_{0.18}\text{As}$ measured at 12 K at five different positions with a laser excitation power of 400 mW.

6.3.2 Laser Excitation Power Dependent PL Measurements

As described in the previous section, power-dependent PL results can be used to identify the transition origin because the relationship between the integrated PL peak intensity and the laser excitation power is dependent on the nature of the PL transition. A linear relationship between the excitation power and the integrated PL intensity indicates an excitonic recombination; a sub-linear relationship indicates a defect or impurity related transition; and a quadratic dependence indicates a band-to-band transition [82, 83]. Laser excitation power dependent PL spectra were measured for both $\text{In}_{0.75}\text{Ga}_{0.25}\text{As}$ and $\text{In}_{0.82}\text{Ga}_{0.18}\text{As}$ crystals at 12 K, and the results are discussed in this section.

The laser excitation power dependent PL spectra for sample $\text{In}_{0.75}\text{Ga}_{0.25}\text{As}$ measured at 12 K are shown in Fig. 6.6. There is a broad peak marked as A at 0.572 eV, and there is another weak peak near 0.55 eV when the laser power is below 200 mW.

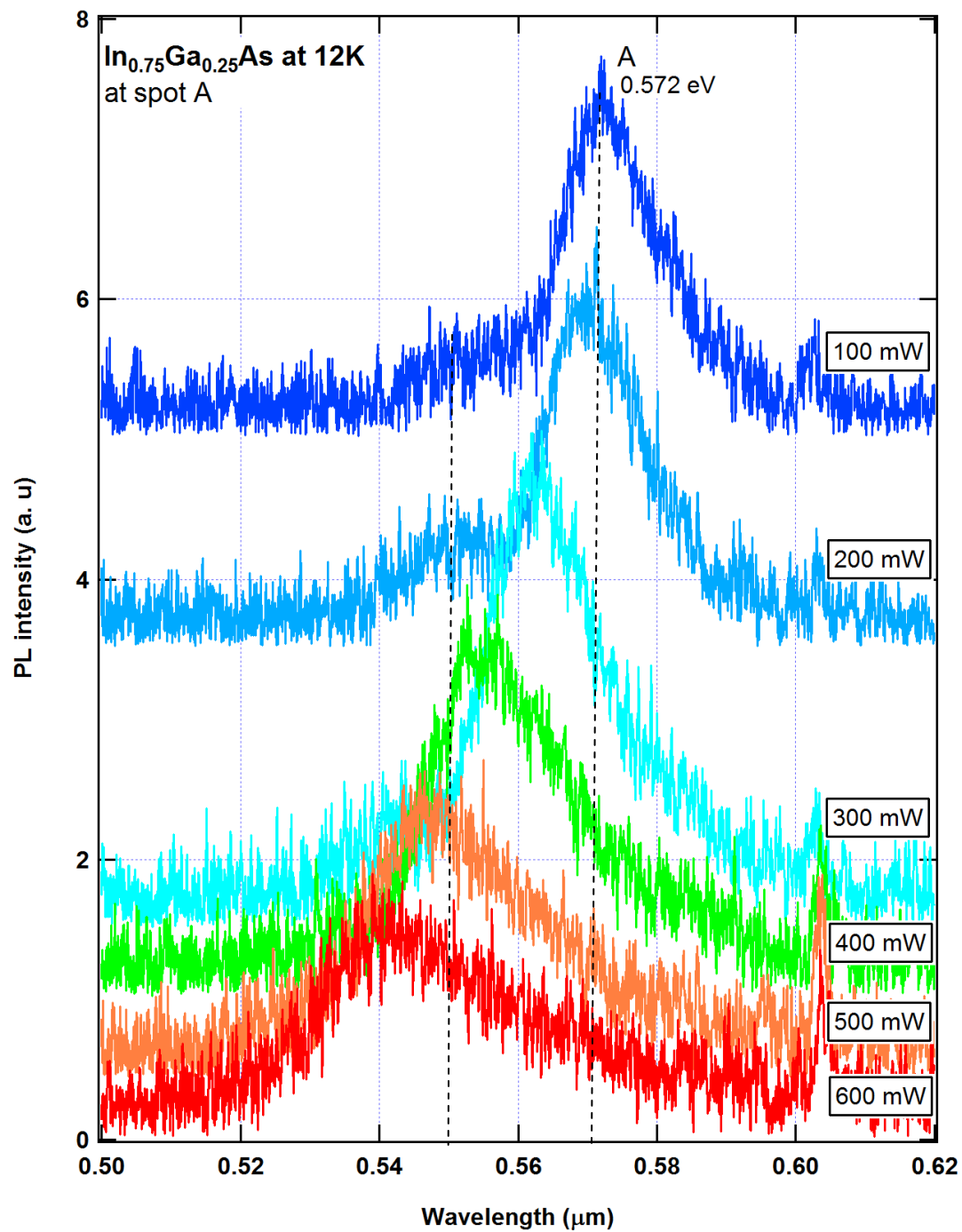


Figure 6.6. Excitation power dependent PL spectra for $\text{In}_{0.75}\text{Ga}_{0.25}\text{As}$ measured at 12 K.

The integrated PL intensity is plotted as a function of excitation power in Fig. 6.7. The intensity of peak A increases as the excitation power increases from 100 mW to 400 mW, and then it decreases. It appears there is a quadratic dependence between the integrated PL intensity and the laser excitation power. Therefore, the broad peak shown in Fig. 6.4 and the peak A observed in Fig. 6.6 for $\text{In}_{0.75}\text{Ga}_{0.25}\text{As}$ sample are a result of band-to-band transition.

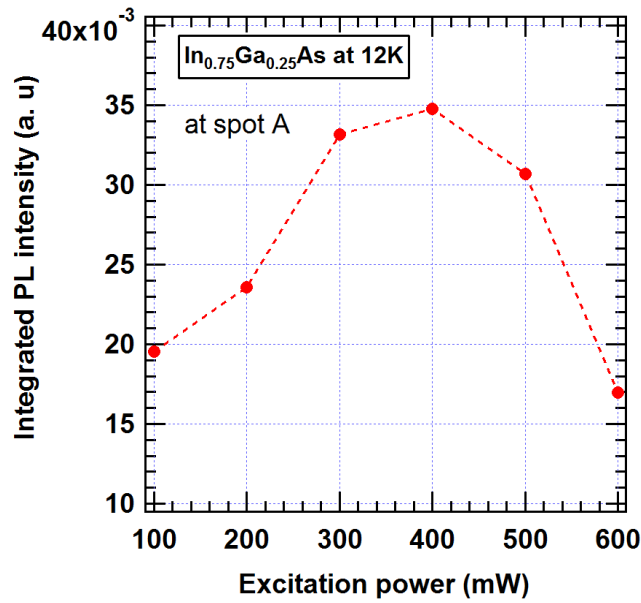


Figure 6.7. Integrated photoluminescence intensities of peak A for the $\text{In}_{0.75}\text{Ga}_{0.25}\text{As}$ sample measured as a function of laser power at 12 K.

For $\text{In}_{0.82}\text{Ga}_{0.18}\text{As}$, the power dependent PL spectra measured at 12 K is shown in Fig. 6.8. They mainly consist of two peaks located at 0.543, and 0.528 eV. The dominant PL peak is at 0.528 eV (indicated by B) when excitation is at or below 400 mW. However, as the excitation power is increased to above 400 mW, the peak A at 0.543 eV becomes dominant and its integrated intensity linearly increases with excitation power.

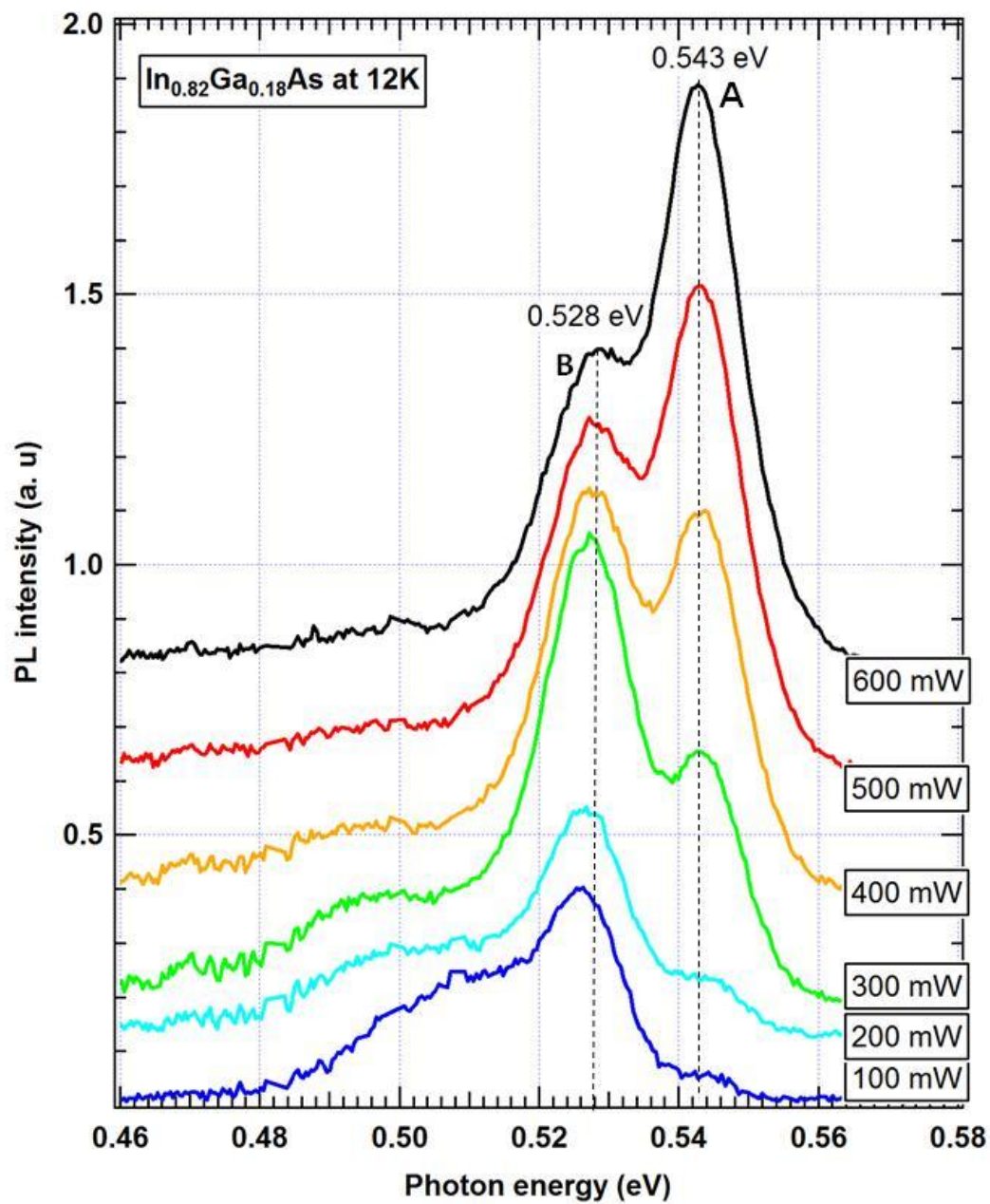


Figure 6.8. Excitation power dependent PL spectra for $\text{In}_{0.82}\text{Ga}_{0.18}\text{As}$ measured at 12 K.

The integrated PL intensities of $\text{In}_{0.82}\text{Ga}_{0.18}\text{As}$ are plotted in Fig. 6.9. Since the integrated PL intensity of peak A clearly shows a linear dependence on excitation power, the luminescence peak A is attributed to an excitonic recombination. On the other hand, the integrated PL intensity of peak B initially increases up to an excitation power of 300 mW, and then decreases gradually with increasing excitation power. This sub-linear relationship indicates that the peak B can be attributed to a DAP transition, which is also consistent with the finding that peak B blue-shifts as the excitation power increases as shown in Fig. 6.8.

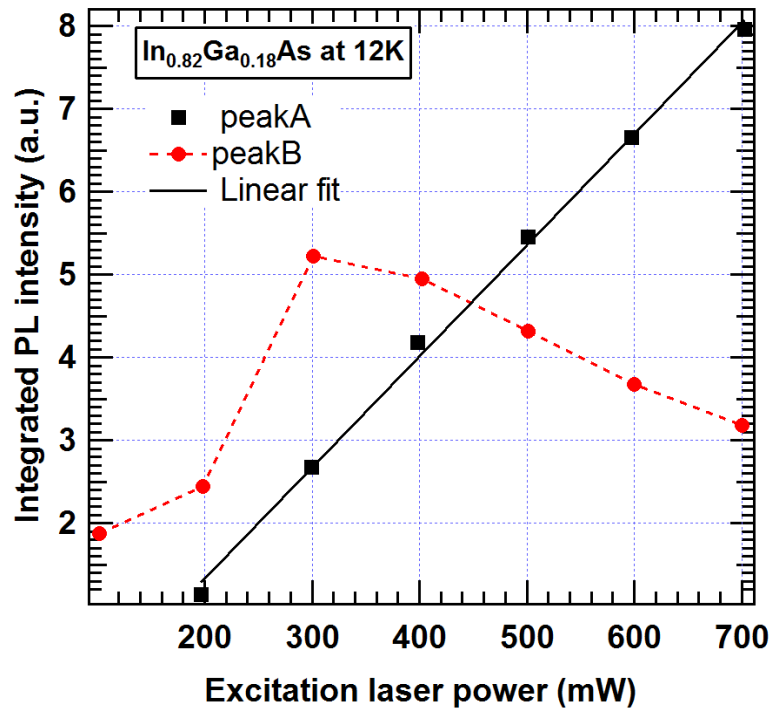


Figure 6.9. Integrated photoluminescence intensities of peaks A and B for the $\text{In}_{0.82}\text{Ga}_{0.19}\text{As}$ sample measured as a function of laser power at 12 K.

6.3.3 Temperature Dependent PL Measurements

PL spectra of the $\text{In}_{0.75}\text{Ga}_{0.25}\text{As}$ sample were measured at a temperature range of 10 – 130 K, and the results are shown in Fig. 6.10. These spectra were taken at spot B on the sample location as indicated at the top right in Fig. 6.4. All spectra show a broad band-to-band recombination peak, and these peaks are broadened and weakened as temperature increases. In addition, the PL peaks red-shift as temperature increases, which is due to E_g decreasing as the temperature increases. The band to band transition peak red shifts by approximately 30 meV as the temperature changes from 12 to 130 K.

The PL spectra for sample $\text{In}_{0.82}\text{Ga}_{0.18}\text{As}$ were also measured at various temperatures and are shown in Fig. 6.11. The PL peak positions indicated by A (FX transition) are red-shifted by approximately 30 meV as the temperature is increased from 12 to 190 K. The peak A persists up to 200 K with decreasing intensity. However, the intensity of the peak B decreases much more rapidly with increasing temperature and completely disappears above 50 K. As shown in Fig. 6.11, both peaks show a red-shift with increasing temperature due to bandgap shrinkage.

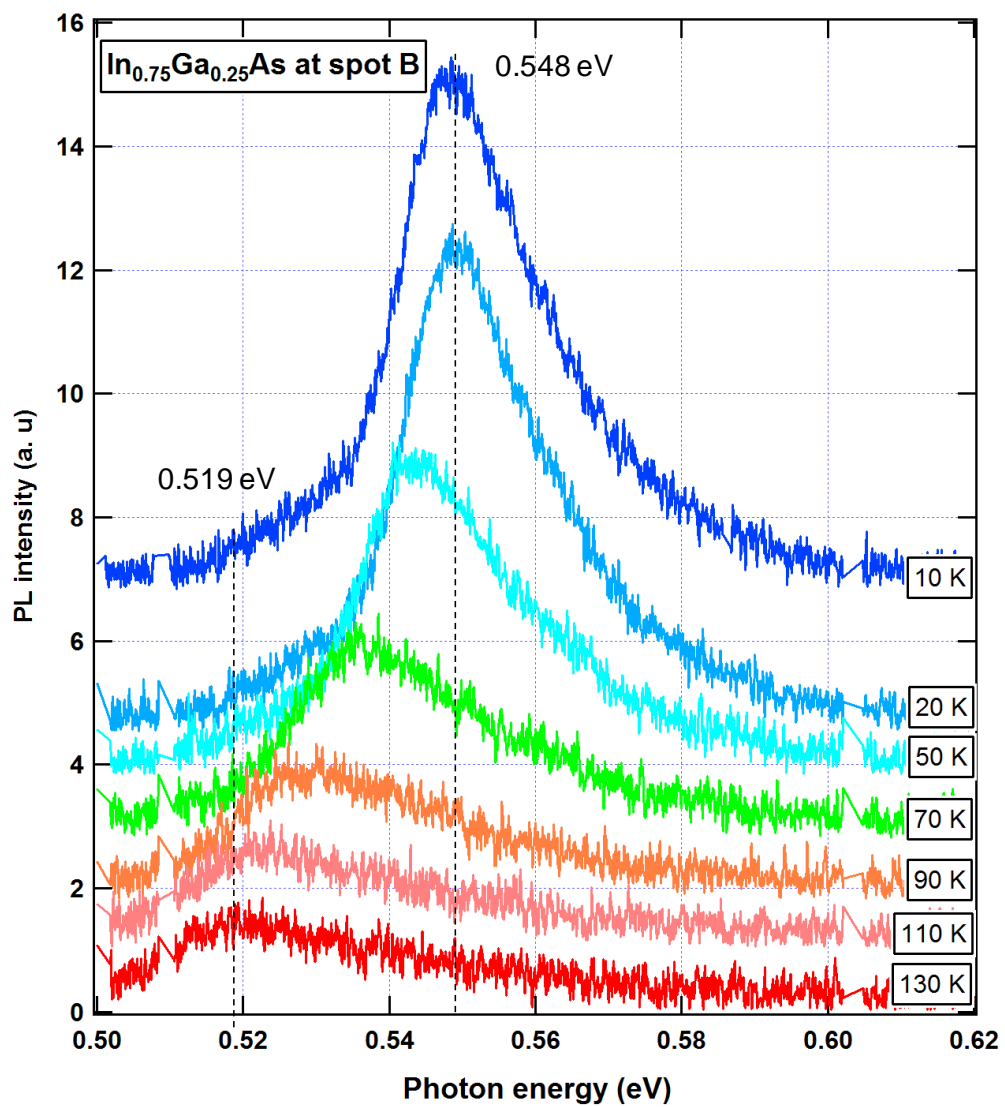


Figure 6.10. Temperature dependent PL spectra for $\text{In}_{0.75}\text{Ga}_{0.25}\text{As}$ with a laser power of 300 mW.

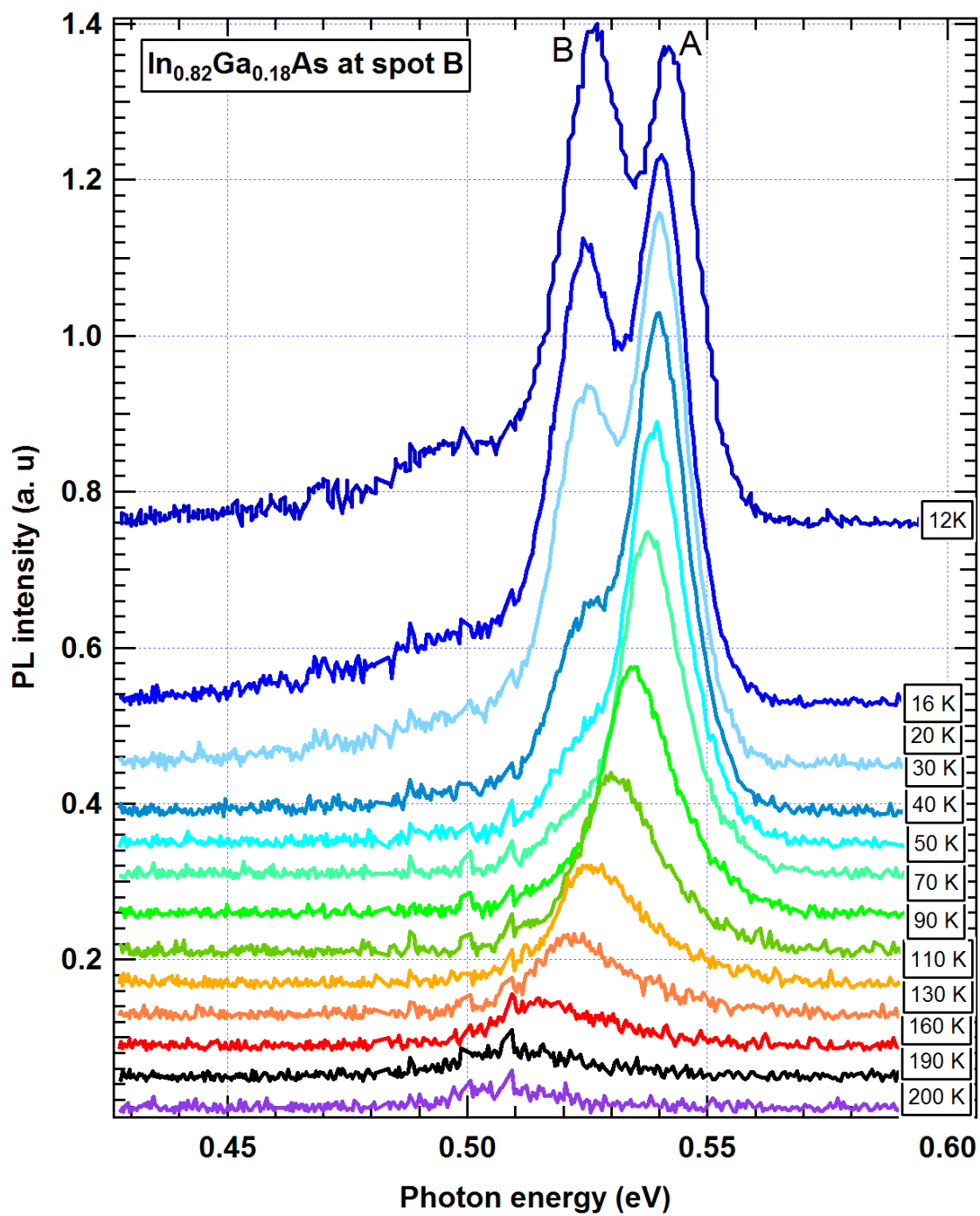


Figure 6.11. Temperature dependent PL spectra for the $\text{In}_{0.82}\text{Ga}_{0.18}\text{As}$ sample measured with a laser excitation power of 300 mW.

In order to compare the temperature dependent bandgap energy between the results from PL and FTIR transmission measurements, temperature dependent transmission spectra ranging from 80 to 440 K were obtained for both $\text{In}_{0.75}\text{Ga}_{0.25}\text{As}$ and $\text{In}_{0.82}\text{Ga}_{0.18}\text{As}$, and the results are shown in Fig. 6.12 (a) and (b), respectively. Temperature dependent $E_{L\min}$ values of $\text{In}_{0.75}\text{Ga}_{0.25}\text{As}$ sample are plotted as a function of temperature in Fig. 6.13 as black triangles, along with B-B PL peak energies acquired at different locations in the sample. In Fig. 6.13, the red dots and blue squares are B-B peak energies obtained from the peaks of PL spectra taken at spot B and C, respectively. They are parallel to each other, and it shows the same temperature dependence. But they are separated by a value of ~ 18 meV due to difference in compositions. It appears that $E_{L\min}$ follows the B-B peak energies very closely, indicating the same temperature dependence.

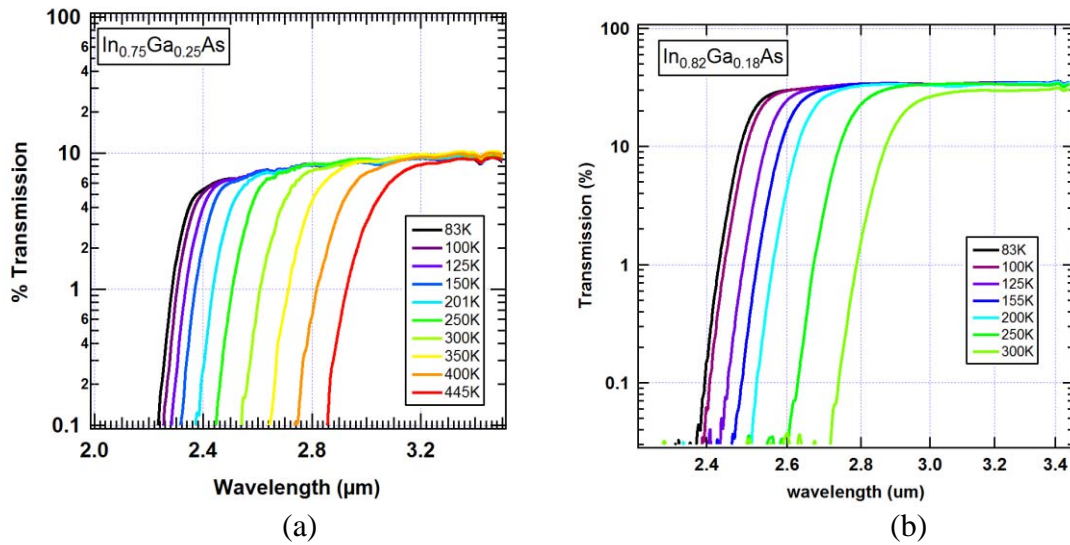


Figure 6.12. Temperature dependent transmission spectra (a) $\text{In}_{0.75}\text{Ga}_{0.25}\text{As}$; (b) $\text{In}_{0.82}\text{Ga}_{0.18}\text{As}$.

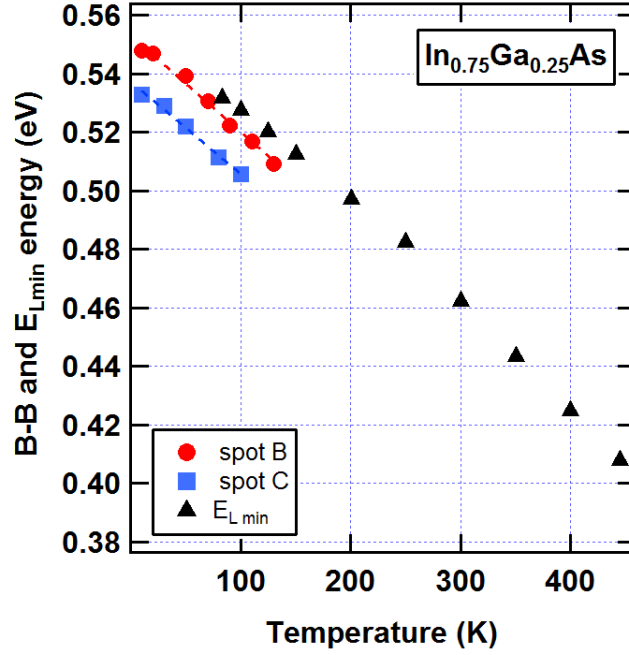


Figure 6.13. Temperature dependent B-B transition energies of $\text{In}_{0.75}\text{Ga}_{0.25}\text{As}$ sample taken at two sample locations. (Red dot taken at spot B, blue square taken at spot C), along with $E_{L\min}$ (black triangle) obtained from transmission spectra.

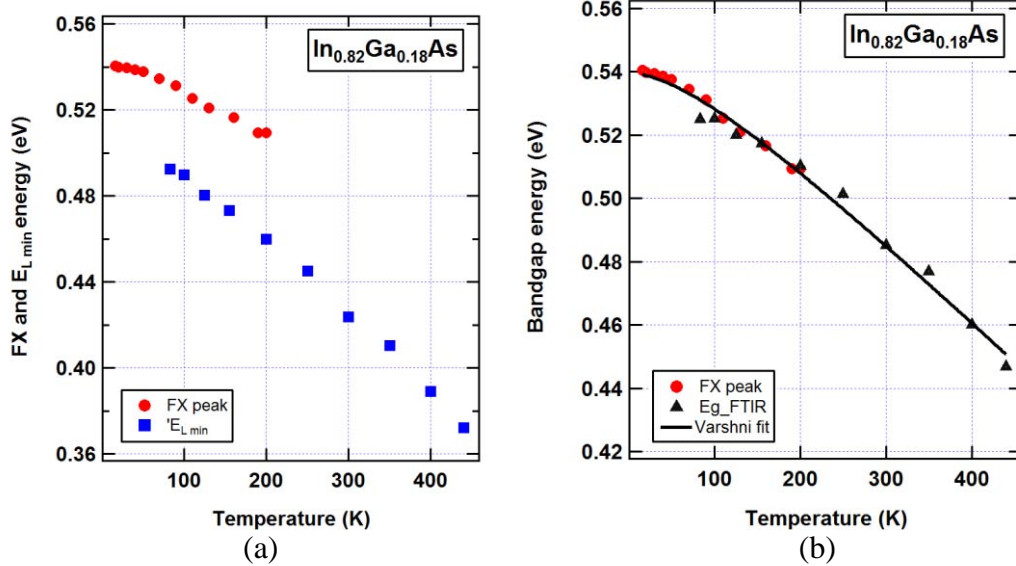


Figure 6.14. (a) Temperature dependent FX peaks (red dots) and $E_{L\min}$ (blue square) of the $\text{In}_{0.82}\text{Ga}_{0.18}\text{As}$; (b) E_g (black triangle) calculated using $E_g = E_{L\min} + \theta\sqrt{T}$ with $\theta = 0.0035 \text{ eVK}^{-0.5}$ plotted as a function of temperature. The solid curve is Varshni equation fit.

For $\text{In}_{0.82}\text{Ga}_{0.18}\text{As}$ sample, the FX peak energy (red dot) is plotted as a function of temperature T in Fig. 6.14 (a) along with the $E_{L \min}$ (blue square) obtained from the temperature dependent transmission spectra. They appear to be parallel with each other at a separation energy of ~ 50 meV, indicating similar temperature dependence. At the $T = 300$ K, the E_g of $\text{In}_{0.82}\text{Ga}_{0.18}\text{As}$ thin film can be calculated using equation 6.1. From known E_g and $E_{L \min}$ values, θ is determined to be of $0.0031 \text{ eV K}^{-0.5}$ using equation 4.13. Thus, the temperature dependent bandgap energy of $\text{In}_{0.82}\text{Ga}_{0.18}\text{As}$ can be calculated and is plotted as a function of temperature (the black triangles) in Fig. 6.14 (b). These calculated bandgap energies are aligned with the FX peak energies (red dots) in the low temperature region as shown in Fig. 6.14 (b). Since the FX binding energy for $\text{In}_{0.82}\text{Ga}_{0.18}\text{As}$ is small (~ 1.5 meV) [69, 83], FX energies for this sample can be approximately considered as the bandgap energy. Combining the results of red dots (FX peaks) and black triangles (from transmission spectra), and curve fitting with the Varshni equation give the temperature dependent bandgap energy relationship for $\text{In}_{0.82}\text{Ga}_{0.18}\text{As}$ as shown in Fig. 6.14 (b) (solid line). The best fit Varshni coefficients are listed in table 6.2 along with the results from other $\text{In}_x\text{Ga}_{1-x}\text{As}$ samples.

Table 6.2. Composition-dependent Varshni coefficients for $\text{In}_x\text{Ga}_{1-x}\text{As}$

Composition x	$E_g(0)$	α ($\times 10^{-4}$) eV/K	β (K)
0.000*	1.519	5.405	204
0.821	0.540	2.90	127
0.99	0.414	4.65	78
1.000*	0.415	2.76	83

* Cited from equation 5.1 and 6.1, which is found at Russia semiconductor web:
<http://www.ioffe.ru/SVA/NSM/Semicond/>

6.4 Refractive Index Measurements

Refractive index measurements on wafer shaped $\text{In}_x\text{Ga}_{1-x}\text{As}$ crystals were performed as functions of wavelength, temperature, and indium composition using Michelson and Fabry-Perot interferometers. The detailed refractive-index measurement method and experimental setup were described in section 3.4.

After the calibration procedure, refractive indices of $\text{In}_x\text{Ga}_{1-x}\text{As}$ crystals were measured using 4.6 μm and 10.6 μm laser beams at temperatures 100 and 295 K. The results are plotted as a function of indium composition in Fig. 6.15 (a) for 4.6 μm and (b) for 10.6 μm . For the full composition range ($0 \leq x \leq 1$), the refractive indices follow a quadratic relation to the composition. The quadratic fitting expressions are listed in table 6.3.

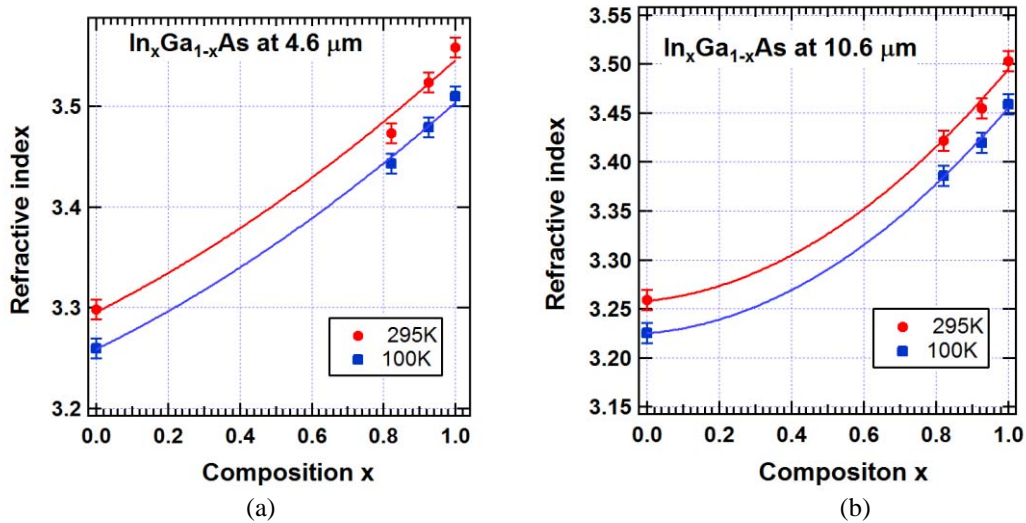


Figure 6.15. Refractive indices of bulk $\text{In}_x\text{Ga}_{1-x}\text{As}$ measured at 100 and 295 K using Michelson and Fabry-Perot method (a) measured at 4.6 μm and (b) measured at 10.6 μm .

Table 6.3. Refractive index of $\text{In}_x\text{Ga}_{1-x}\text{As}$ as a function of composition at various wavelengths and temperatures

Sample Conditions	Refractive Index, $n(x, \lambda, T)$
At 4.6 μm and at 100 K	$3.259+0.175x+0.070x^2$
At 4.6 μm and at 295 K	$3.296+0.180x+0.070x^2$
At 10.6 μm and at 100 K	$3.225+0.031x+0.200x^2$
At 10.6 μm and at 295 K	$3.258+0.037x+0.200x^2$

Note: Michelson and Fabry-Perot interferometry methods are very sensitive to defects in the crystal, and it was a challenge to accurately measure the refractive index for polycrystalline $\text{In}_x\text{Ga}_{1-x}\text{As}$ using these methods. For this work, the accuracy of refractive index is only ± 0.01 , which is far less than the achievable accuracy using the minimum deviation method. The uncertainty is included as an error bar in Fig. 6.15.

6.5 Hall-effect Measurements

Square shaped wafer of $\text{In}_x\text{Ga}_{1-x}\text{As}$ crystal with dimensions $10 \times 10 \times 0.5 \text{ mm}^3$ was used for the Hall-effect measurements. The ohmic contacts were placed on the periphery of the sample using indium. Hall-effect measurements were conducted at 77 and 300 K with a magnetic field of 5 kG for samples with different indium mole fractions. Carrier concentration and Hall mobility were studied as functions of composition and temperature, and the results are shown in Fig. 6.16 (a) for carrier concentration and (b) for Hall mobility.

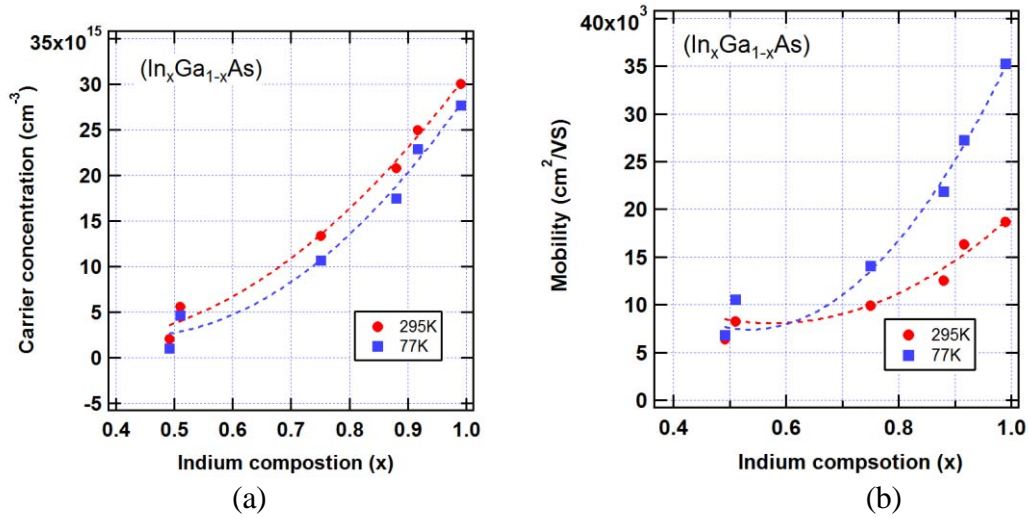


Figure 6.16. Hall-effect measurement results at 77 and 300 K for various $\text{In}_x\text{Ga}_{1-x}\text{As}$ samples as a function of indium mole fraction: (a) carrier concentration and (b) Hall mobility.

All samples were found to exhibit n-type conductivity, which was possibly due to residual impurities and native defects, such as indium and gallium vacancies and/or their antisites. Both carrier concentration and mobility generally increase with indium content due to a decrease in bandgap energy. High carrier mobility of $16,000 \text{ cm}^2\text{V}^{-1}\text{S}^{-1}$ at 295 K for $\text{In}_{0.91}\text{Ga}_{0.09}\text{As}$ sample is an indication of a good crystal. Resistivity at room temperature changes from approximately 0.4 to $0.02 \text{ } \Omega\text{-cm}$ as the indium mole fraction increases from 0.5 to 1 (not shown here).

7. Conclusions and Future Work

Optical and electrical properties of bulk, melt-grown $\text{InAs}_{1-y}\text{P}_y$ and $\text{In}_x\text{Ga}_{1-x}\text{As}$ polycrystals were investigated as functions of phosphorus and indium compositions and temperatures using the photoluminescence (PL), Fourier transform infrared (FTIR) transmission spectroscopy, refractive index, and Hall-effect measurements.

These ternary alloys with diameters up to 50 mm were grown using the vertical Bridgman technique. The critical growth conditions for large diameter (50 mm) crack free bulk ternary $\text{InAs}_{1-y}\text{P}_y$ and $\text{In}_x\text{Ga}_{1-x}\text{As}$ polycrystals were briefly described in this dissertation. The as-grown undoped bulk ternary $\text{InAs}_{1-y}\text{P}_y$ and $\text{In}_x\text{Ga}_{1-x}\text{As}$ polycrystals have been found to exhibit n-type conductivity irrespective of the alloy compositions. This is possibly due to residual impurities and native defects, such as indium and gallium vacancies, and/or their antisites for $\text{In}_x\text{Ga}_{1-x}\text{As}$ samples, and arsenic and phosphorus vacancies, and/or their antisites for $\text{InAs}_{1-y}\text{P}_y$ sample. Although the bulk $\text{InAs}_{1-y}\text{P}_y$ and $\text{In}_x\text{Ga}_{1-x}\text{As}$ crystals showed good optical transmission in the infrared and high carrier mobility, they exhibited random compositional fluctuations across the substrate area.

The refractive index, transport properties, and below-bandgap transmission were presented here as a function of alloy composition and temperature for the first time, to the best of our knowledge. A practical method of extracting bandgap energies directly from the FTIR transmission spectra has been presented in this work. The method was verified to several binary semiconductors with known bandgaps and was applied to determine the unknown properties of novel ternary semiconductors $\text{In}_x\text{Ga}_{1-x}\text{As}$ and $\text{InAs}_{1-y}\text{P}_y$. The results are promising, although further improvement is required. Bandgap energies

estimated from the transmission spectra agree well with those obtained from PL peaks and the previously reported values from the thin film studies.

FTIR spectra were measured for all these ternary samples, and they showed little or no absorption for photon energy less than bandgap. The temperature dependent bandgap energies and temperature dependent refractive indices were also able to be extracted from the composition and temperature dependent FTIR transmission spectra. This process involves taking the derivative of the transmission with respect to photon energy (dT/dE). A Gaussian-like curve was observed for all (dT/dE) studied when it is plotted as a function of photon energy. The values of $E_{L\min}$ could be determined from the peak locations of (dT/dE). Then, using the relationship, $E_g = E_{L\min} + \theta\sqrt{T}$, the bandgap energy (E_g) was obtained. The fitting parameter θ can be determined from the known bandgap energy at a given temperature (for instance, the bandgap energy of the thin films at room temperature). This method of bandgap estimation from the FTIR transmission spectra shows very promising results for InAs, InP, GaAs, $\text{InAs}_{1-y}\text{P}_y$, and $\text{In}_x\text{Ga}_{1-x}\text{As}$.

A systematic measurement of photoluminescence was carried out in order to gain insight into the various radiative transitions in $\text{InAs}_{1-y}\text{P}_y$ and $\text{In}_x\text{Ga}_{1-x}\text{As}$ crystals. This study includes temperature, laser excitation power, and sample position dependent PL measurements. The excitation power-dependent PL results can be used to identify the origin of the transition because the relationship between the integrated PL peak intensity and the laser excitation power is dependent on the nature of the PL transition. The results of PL measurements show that free exciton (FX) transitions are dominant for high quality $\text{InAs}_{1-y}\text{P}_y$ and $\text{In}_x\text{Ga}_{1-x}\text{As}$ crystals. The temperature dependent PL measurements show that PL peaks red-shift with increasing temperature due to the bandgap decreasing as a

result of lattice expansion and phonon vibration. The FX peak positions of $\text{InAs}_{0.81}\text{P}_{0.19}$ are red-shifted by approximately 40 meV as temperature changes from 12 to 130 K. The FX peak positions of $\text{In}_{0.82}\text{Ga}_{0.18}\text{As}$ are red-shifted by approximately 30 meV as temperature changes from 12 to 190 K. The red-shift is also observed with an increase of indium mole fraction for $\text{In}_x\text{Ga}_{1-x}\text{As}$ and a decrease of the phosphorus mole fraction for the $\text{InAs}_{1-y}\text{P}_y$ crystal. The FX peak positions of $\text{In}_x\text{Ga}_{1-x}\text{As}$ are red-shifted from 0.568 to 0.412 eV as an indium mole fraction increases from 0.75 to 0.99.

Temperature-dependent bandgap energies were also obtained from temperature-dependent PL spectra, and the results were compared with those obtained from the transmission spectra as well as the published thin film data. It shows that both results are in good agreement with each other and also they fit well with the Varshni expression. Varshni coefficients over temperature range of 10 - 400 K were obtained for the first time for the bulk $\text{In}_x\text{Ga}_{1-x}\text{As}$ at $x=0.82$ and 0.99, and for the $\text{InAs}_{1-y}\text{P}_y$ at $y = 0.19, 0.24,$ and 0.34.

From the location dependent PL measurements, it has been observed a FX PL peak energy variation on the order of 5 - 11 meV within a $\text{In}_x\text{Ga}_{1-x}\text{As}$ wafer, indicating about 1-3% of variation in composition across this bulk sample. Also the FX PL peak locations of $\text{InAs}_{0.81}\text{P}_{0.19}$ measured at 12 K are at 0.556, 0.575, and 0.594 eV. This shows a variation of 38 meV, indicating the variation in composition of about 5% across the sample.

The refractive index of $\text{InAs}_{0.81}\text{P}_{0.19}$ was measured as functions of wavelength and temperature using the minimum deviation method. At all three wavelengths (3.39, 4.64 and 10.60 μm), the refractive index varied linearly in the temperature range between 90

and 295 K. Refractive indices of $\text{InAs}_{1-y}\text{P}_y$ were also obtained for various compositions at two temperatures with IR wavelength of 4.6, 3.39 and 10.6 μm . The refractive indices measured at 3.39 μm are greater than those at 4.6 μm , and those at 4.6 μm are greater than those measured at 10.6 μm . However, the difference due to different photon wavelengths is not significant compared to the variations in indices due to different compositions. For $\text{InAs}_{0.81}\text{P}_{0.19}$, a comparison between theoretical dn/dT and experimental dn/dT was made at three wavelengths, and they agreed reasonably well. In order to improve the accuracy, an accurate electron effective mass of $\text{InAs}_{0.81}\text{P}_{0.19}$ is needed in Kane energy (E_p) calculation.

The refractive index was measured for wafer shaped $\text{In}_x\text{Ga}_{1-x}\text{As}$ crystals as functions of wavelength, temperature and indium composition using Michelson and Fabry-Perot interferometers. The refractive indices of full composition range (from 0 to 1) were obtained for the first time, to the best of our knowledge, for $\text{In}_x\text{Ga}_{1-x}\text{As}$ at 4.6 and 10.6 μm and at 100 and 295 K. Also, for the first time, the temperature dependent refractive indices for $\text{InAs}_{0.81}\text{P}_{0.19}$ were obtained at wavelengths 3.39, 4.64 and 10.60 μm , and at temperatures ranging from 90 to 295 K.

All as-grown $\text{In}_x\text{Ga}_{1-x}\text{As}$ samples show high mobilities, e.g., 4.8×10^3 and $1.4 \times 10^4 \text{ cm}^2/\text{V}\cdot\text{s}$ at 300 K for $\text{In}_{0.75}\text{Ga}_{0.25}\text{As}$ and $\text{In}_{0.99}\text{Ga}_{0.01}\text{As}$, respectively, indicating a good crystal quality. Both carrier concentration and mobility generally increase with indium content due to a decrease in bandgap energy. All $\text{In}_x\text{Ga}_{1-x}\text{As}$ and $\text{InAs}_{1-y}\text{P}_y$ samples show n-type conductivity. Carrier concentration for $\text{In}_{0.5}\text{Ga}_{0.5}\text{As}$ at room temperature is $\sim 5 \times 10^{15} \text{ cm}^{-3}$, and it increases with indium mole fraction.

For $\text{InAs}_{1-y}\text{P}_y$ samples, both carrier concentration and mobility generally decrease with phosphorus mole fraction due to an increase in bandgap. High carrier mobility of $8,200\text{cm}^2/\text{V}\cdot\text{s}$ at 295 K for the $\text{InAs}_{0.81}\text{P}_{0.19}$ sample is an indication of good crystal quality. The room temperature resistivity changes from approximately 0.02 to 0.14 $\Omega\cdot\text{cm}$ as the phosphorus mole fraction increases from 0.19 to 0.66.

Temperature-dependent Hall-effect measurements were also carried out from 20 to 310 K for $\text{InAs}_{0.9}\text{P}_{0.1}$. The carrier concentration was $3.8\times 10^{16}\text{ cm}^{-3}$ at 20 K, and remained almost constant up to approximately 50 K, then it increases as the temperature is increased further up to room temperature. The mobility remains about the same at temperatures from 20 to 50 K, and then it starts to decrease linearly with temperature. It reaches a peak mobility of $2.7\times 10^4\text{ cm}^2/\text{V}\cdot\text{s}$ at 70 K, and then decreases to $1.4\times 10^4\text{ cm}^2/\text{V}\cdot\text{s}$ as the sample temperature is increased to 300 K.

In summary, optical and electrical properties of bulk $\text{In}_x\text{Ga}_{1-x}\text{As}$ and $\text{InAs}_{1-y}\text{P}_y$ crystals were systematically studied as functions of composition (indium mole fraction for $\text{In}_x\text{Ga}_{1-x}\text{As}$ and phosphorus mole fraction for $\text{InAs}_{1-y}\text{P}_y$ in full range) and temperature (ranging from 10 – 400 K). Many of these properties are reported for the first time, to the best of our knowledge. It seems that it is more challenging to grow high quality ternary crystals with small indium content (x) for $\text{In}_x\text{Ga}_{1-x}\text{As}$, and large phosphorus content (y) for $\text{InAs}_{1-y}\text{P}_y$. Optical and electrical properties of these crystals are well suited for a variety of applications that do not require a single crystal.

For future work, it would be very desirable to grow bulk $\text{In}_x\text{Ga}_{1-x}\text{As}$ and $\text{InAs}_{1-y}\text{P}_y$ single crystals or perhaps polycrystals with a large enough area of single crystal section so that the single crystal area can be used as a substrate for subsequent growth of good

epitaxial layers with a wide range of compositions. The presence of random macroscopic composition fluctuations and the intrinsic defects formed in the crystals requires refinement of crystal growth conditions. More efficient melt mixing processes or enhancements with magnetic fields during crystal growth may help eliminate the intrinsic defects formed in the crystals using current techniques. Undoubtedly, further characterization studies are required for improved bulk ternary alloys. Also, work in the temperature dynamics of carrier properties and on nonlinear optical properties of these materials at various infrared wavelengths and temperatures will be needed to be carried out. Newer materials and their applications need to be developed, and often binary and ternary III-V compounds (GaSb, GaP, GaSbP etc) can also be studied using the method developed in this work.

Appendix A

Related Publications

J. Wei, J. Barnes, S. Guha, L. P. Gonzalez, Y. K. Yeo, R. L. Hengehold and G. Rajagopalan, “Electrical and Optical Characterization of Melt Grown Bulk $\text{InAs}_{1-y}\text{P}_y$ Crystals”, J. Electronics Materials, **40** (2) p1432-9 (2011).

Y. K. Yeo, A. C. Bergstrom, R. L. Hengehold, J. Wei, S. Guha and L. P. Gonzalez, G. Rajagopalan, Mee-Yi Ryu, “Optical and Electrical Properties of Bulk-Grown Ternary $\text{In}_x\text{Ga}_{1-x}\text{As}$ ”, Accepted for publication at Journal of the Korean Physical Society 2010.

Xiaofeng Duan, Jean Wei, Larry Burggraf, and David Weeks, “Mapping Ground-State Properties of Silicon Carbide Molecular Clusters using Quantum Mechanical Calculations: Si_mC_n and $\text{Si}_m\text{C}_n\text{-(m, n < 4)}$ ”, Computational Material Science, **47** (3) p630-644 (2010)

P. G. Schunemann, L. a. Pomeranz, K. T. Zawilski, Jean Wei, Leonel P. Gonzalez, Shekhar Guha, T. M. Pollak, “Efficient Mid-infrared Optical Parametric Oscillator Based on CdSiP_2 ”, published in 2009 at Advances in Optical Materials, OSA.

J. W “Use of Quantum Mechanical Calculations to Investigate Small Silicon Carbide Clusters” (Master thesis on file at Air Force Institute of Technology Academic Library, 2001)

Appendix B

Hall Effect Measurements

Sample and system preparation

Sample

1. Use the green card holder. Place the sample in the center of these pressure pins.
2. Turn on the ultrasonic soldering iron.
3. Apply indium solder at the four corner of the squared sample as ohmic contact.
4. Apply a small drop of rubber cement to the back of the sample using a sharpened cotton swap stick. Place each one of the four pressure probes on each contact.
5. Use the curve tracer (power on, memory 1, hit recall) to check the connections, a vertical straight line indicates good ohmic contact.
6. Insert card into sample mount.
7. Connect the 4 yellow testing cables to the top of the sample probe.
8. Check that the temperature sensor cable is connected.
9. Turn on the water line to cool the magnets. Checks to make sure the return water lines are open.

System Preparation

1. Check for water leaking from the connections at the back of the magnets.
2. Check the placement of the Gaussmeter.
3. Flip the switch on the front of the magnet power supply into stand by mode.
4. Make sure all the interlock lights are green. Hit the reset button if any are red.
5. Push the green button to power on the magnets.
6. Turn on equipment stack. (red button upper right side on cabinet)

7. Turn on the computer and log in with password Lake Shore.
8. Open the program from icon on desktop. (Hall Measurement System)
9. Make sure all equipment is functioning by checking the Systems Logs box in the program.

Measurement

1. Choose a current to test the samples, one that works through the entire temperature range.
 - Click on the resistivity button at the top right corner of the program.
 - Choose high or low resistivity.
 - Select the contact configuration to test (12, 12).
 - Select a current and click the measure button.
 - Monitor that the output is in range and that there are no errors.
 - Check that the current works for all contact pairs. (23,23; 34,34; 14,14)
2. Check that the contacts are linear.
 - Do an I-V test with the selected current chose a step that result in about 5 measurement points. (right click in the measurements box on the left and choose I-V measurement)
 - Choose high or low resistivity based on the sample material.
 - Choose default contact pairs, click ok.
 - Click the Start button at the top of the program.
3. Create a program for RT, HT or LT measurements. (right click in the measurements box on the left and choose variable field of variable temperature measurement)
 - Select Hall and resistivity measurements
 - Select to calculate resistivity at zero field.
 - Select a magnetic field of 5 kG; choose a step of 1 kG.

- Enter the chosen current both positive and negative.
- Select high or low resistivity.
- Enter the temperatures for measurement.

* Temperature-dependent measurements take ~5 hours.

* Room temperature measurements with different three currents take ~20 min.

Shut Down

1. Turn off the magnets. (red button)
2. Put the magnet power supply out of stand by mode. (toggle switch)
3. Turn off water to magnets.
4. Turn off compressor after LT measurements.
5. Turn of water to the compressor.
6. Close the HMS.exe program.
7. Turn off computer monitor or entire stack if not going to use for awhile.
8. Wait for systems to return to room temperature. (294 K)
9. Turn off vacuum pump. (ONLY if system is at room temperature)
10. Wait for sample chamber to pressurize.
11. Unplug the necessary cables to remove sample mount.
12. Remove sample.
13. Assemble the sample chamber to keep dust and contaminants out while not in use.

Photoluminescence Measurements

Sample and system preparation

1. Cleaning the sample surface with TCE, acetone, methanol, and DI water.
2. A Spectro-Physics BeamLok 2085-20 Ar Ion laser is the exciting source. This laser is chopped at ~ 170 Hz using a ThorLabs optical chopper.
3. Apply some crycon thermal grease on the back of sample and attach the grease side to the cold finger that connected to the Helitran, the incident laser and sample is approximately at 45^0 angle. Close the chamber and turn on the vacuum pump.
4. Open the valve that connects the sample system and the liquid helium tank after the vacuum reaches 20 mili-Torr, so the temperature can be cooled down using evaporated liquid helium gas.

Measurement

1. After the temperature reaches approximately 10 K, adjust the collecting lenses and sample angle so the photoluminescence enter the entrance slit of the spectrometer (SPEX 750 M), the spectrometer is purged using high purity nitrogen gas.
2. The intensity of photoluminescence spectra is measured using a Teledyne Judson Technologies J10D InSb detector (it is liquid nitrogen-cooled and operated with a 12 V bias preamplifier) and a lock-in amplifier which is synchronized with the optical chopper.
3. Make sure to use a full range for the first scan; choose a lower resolution to save time (only for the first scan). Then use a higher resolution after identifying the main PL peak as well as adjusting the scan range according to the PL peak location.
4. Conducting the sample location variation and laser power dependent as well as temperature dependent PL spectra.
5. Adjust the temperature to the desired one using the Lakeshore temperature controller by touching “set the point” and press the up and down button then press “enter”.
6. Adjust the laser power by adjusting output power using the laser control panel.

Shut Down

1. Close the Helium gas flow meter (connect with the sample dewar).
2. Set the sample temperature to 295K.
3. Release the Helium tank valve (two yellow valve handles, release them gently).
4. When sample chamber temperature reaches $> 200\text{K}$, unplug the heater (connected to the Helium flow meter tube).
5. Shut down the laser. (turn the current to the minimum, turn the key to off).
6. Shut down the purge nitrogen gas. (Close N_2 flow meter, close the main valve of the N_2 bottle).
7. Turn off the chiller.
8. Turn off the water connected to the chiller (yellow valve under the optical table).
9. Turn off the optical chopper (controller power off).
10. Turn off the power supply connected to the preamplifier of the detector.
11. Close the spectrometer slot. (push down the nub)
12. By the time temperature reach 295K, choose heater off (on the Lake shore temperature controller)
13. By the time the Helium release is complete, close one of the yellow valves, and leave another yellow valve completely open (the one that has pressure control)

Appendix C

Magnetic Field Reading Correction

Resistivity

Let B_S = sample field and B_P = field at magnetic pole.

$$R_{HS}^{real} = \frac{\Delta R_{13,24}}{B_S}$$

$$\Delta R_{13,24}^{real} = \left[R_{13,24} \right]_{B_S=0} - \left[R_{13,24} \right]_{B=B_S} \leftarrow \text{depends on B-field}$$

$$R_{HS}^{real} = \frac{\Delta R_{13,24}}{B_S} \times \frac{B_P}{B_P} = \left(\frac{B_P}{B_S} \right) \frac{\Delta R_{13,24}}{B_P} = \left(\frac{B_P}{B_S} \right) R_{HS}^{\text{computer calculated}}$$

Let r = real and cc = computer calculated.

$$(1) \quad \boxed{R_{HS}^r = \left(\frac{B_P}{B_S} \right) R_{HS}^{cc}} \text{ real accurate value to be obtained.}$$

$$R_{HS}^{cc} = \frac{\Delta R_{13,24}}{B_P} \leftarrow \text{depends on applied B field}$$

Hall Mobility

$$\mu_H^{real} = \frac{R_{HS}^{real}}{\rho_S} = \left(\frac{B_P}{B_S} \right) \frac{R_{HS}^{cc}}{\rho_S} = \left(\frac{B_P}{B_S} \right) \mu_S^{cc}$$

$$(2) \quad \boxed{\mu_H^r = \left(\frac{B_P}{B_S} \right) \mu_S^{cc}}$$

Carrier concentration

$$n_S^{real} = \frac{1}{e R_{HS}^{real}} = \frac{1}{e \left(\frac{B_P}{B_S} \right) R_{HS}^{cc}} = \left(\frac{B_S}{B_P} \right) \frac{1}{e R_{HS}^{cc}} = \left(\frac{B_S}{B_P} \right) n_S^{cc}$$

$$(3) \quad \boxed{n_S^{real} = \left(\frac{B_S}{B_P} \right) n_S^{cc}}$$

At two different fields: B_{P1} , B_{P2} , B_{S1} , B_{S2}

$$R_{HS}^{r,1} = \frac{\Delta R^{r,1}}{B_{S1}} \quad \text{and} \quad R_{HS}^{r,2} = \frac{\Delta R^{r,2}}{B_{S2}}$$

$$\Delta R^{r,1} = \left[R_{13,24} \right]_{B_S=0} - \left[R_{13,24} \right]_{B=B_{S1}} \quad \text{and} \quad \Delta R^{r,2} = \left[R_{13,24} \right]_{B_S=0} - \left[R_{13,24} \right]_{B=B_{S2}}$$

$$R_{HS}^{r,1} = \left(\frac{B_{P1}}{B_{S1}} \right) R_{HS}^{cc1} \quad R_{HS}^{r,2} = \left(\frac{B_{P2}}{B_{S2}} \right) R_{HS}^{cc2}$$

$$\mu_H^{r,1} = \left(\frac{B_{P1}}{B_{S1}} \right) \mu_H^{cc1} \quad \mu_H^{r,2} = \left(\frac{B_{P2}}{B_{S2}} \right) \mu_H^{cc2}$$

$$n_S^{r,1} = \left(\frac{B_{S1}}{B_{P1}} \right) n_S^{cc1} \quad n_S^{r,2} = \left(\frac{B_{S2}}{B_{P2}} \right) n_S^{cc2}$$

We must have $\boxed{\mu_H^{r,1} = \mu_H^{r,2} \quad \text{and} \quad n_S^{r,1} = n_S^{r,2}}$

$$\text{Then } \left(\frac{B_{P1}}{B_{S1}} \right) \mu_H^{cc1} = \left(\frac{B_{P2}}{B_{S2}} \right) \mu_H^{cc2} \quad \text{or} \quad \left(\frac{B_{S1}}{B_{P1}} \right) n_S^{cc1} = \left(\frac{B_{S2}}{B_{P2}} \right) n_S^{cc2}$$

$$\text{If } \left(\frac{B_{P1}}{B_{S1}} \right) = \left(\frac{B_{P2}}{B_{S2}} \right), \text{ then } \mu_H^{cc1} = \mu_H^{cc2} \quad \text{or} \quad n_S^{cc1} = n_S^{cc2}$$

$$\text{Also, } \mu_H^{r,1} = \frac{R_{HS}^{r,1}}{\rho_S} \quad \text{and} \quad \mu_H^{r,2} = \frac{R_{HS}^{r,2}}{\rho_S}$$

$$\text{Then } \left(\frac{B_{P1}}{B_{S1}} \right) R_{HS}^{cc1} = \left(\frac{B_{P2}}{B_{S2}} \right) R_{HS}^{cc2}$$

$$\text{If } \left(\frac{B_{P1}}{B_{S1}} \right) = \left(\frac{B_{P2}}{B_{S2}} \right), \text{ then } R_{HS}^{cc1} = R_{HS}^{cc2} \quad \text{that is} \quad \frac{\Delta R_{P1}^{r,1}}{B_{P1}} = \frac{\Delta R_{P2}^{r,2}}{B_{P2}}$$

$$\text{Therefore, } \boxed{R_{HS}^{r,1} = R_{HS}^{r,2}}$$

Bibliography

1. www.sarracenia.com/.../physics060.html
2. T. Baba, Y. Yogo, K. Suzuki, F. Koyama, and K. Iga, "Near room temperature continuous wave lasing characteristics of GaInAsP/InP surface emitting laser", *Electron. Lett.* **29**, p913-914, (1993).
3. T. Uchida, T. Uchida, F. Koyama, and K. Iga, "Control of GaInAs/InP layer thickness for surface-emitting lasers by chemical beam epitaxy", *Electron. Communi. in Japan Part II* **75**, p101-107, (1992).
4. S. H. Pyun and W. G. Jeong, "Luminescence characteristics of InGaAs/GaAs quantum dots emitting near 1.5 μm ", *J. Korean Phys. Soc.* **56**, p586-590, (2010).
5. M. R. Soulby, D. G. Revin, J. P. Commin, A. B. Krysa, J. S. Roberts, and J. W. Cockburn, "Probing diagonal laser transitions in InGaAs/InP quantum cascade lasers", *J. Appl. Phys.* **106**, p123106-123109, (2009).
6. H. Shoji, T. Uchida, T. Kusunoki, M. Matsuda, H. Kurakake, S. Yamazaki, K. Nakajima, and H. Ishikawa, "Fabrication of $\text{In}_{0.25}\text{Ga}_{0.75}\text{As}/\text{InGaAsP}$ strained SQW lasers on $\text{In}_{0.05}\text{Ga}_{0.95}\text{As}$ ternary substrate", *IEEE Photon. Technol. Lett.* **8**, p1170-1171, (1994).
7. A. H. Moore, B. Lent, and W. A. Bonner, "Fabrication of high power InGaAs/AlInGaAs strained SQW lasers on InGaAs ternary substrates", *Electron. Lett.* **32**, p2018-2019, (1996).
8. H. Shoji, K. Otsubo, T. Kusunoki, T. Suzuki, T. Uchida, and H. Ishikawa, "In_{0.38}Ga_{0.62}As/InAlGaAs/InGaP strained double quantum well lasers on In_{0.21}Ga_{0.79}As ternary substrate", *Jpn. J. Appl. Phys.* **35**, L778-780, (1996).
9. A. M. Jones, B. Lent, J. F. Kluender, S. D. Roh, A. H. Moore, W. A. Bonner, and J. J. Coleman, "Aluminum-free strained-layer lasers emitting at 1.14 μm on low-composition InGaAs:n substrates by metalorganic chemical vapor deposition", *IEEE Photon. Tech. Lett.* **9**, p1319-1321, (1997).
10. M. R. Matthews, R. J. Steed, M. D. Frogley, C. C. Phillips, R. S. Attaluri, and S. Krishna, "Transient photoconductivity measurements of carrier lifetimes in an InAs/In_{0.15}Ga_{0.85}As dots-in-a-well detector", *Appl. Phys. Lett.* **90**, p103519, (2007).
11. S. Tsao, H. Lim, W. Zhang, and M. Razeghi, "High operating temperature 320x256 middle-wavelength infrared focal plane array imaging based on an

- InAs/InGaAs/InAlAs/InP quantum dot infrared photodetector”, *Appl. Phys. Lett.* **90**, p201109, (2007).
12. A. Bouzid, J.-B. Park, S. Moon, “Effects of the active hold-off technique in 1.55 μm single photon diction”, *J. Korean Phys. Soc.* **56**, p1418-1422, (2010).
 13. K. Zekentes, G. Halkias, A. Dimoulas, A. Tabata, T. Benyattou, G. Guillot, J. R. Morante, F. Peiró, A. Cornet, A. Georgakilas, and A. Christou, “Materials problems for the development of InGaAs/InAlAs HEMT technology”, *Mater. Sci. Eng. B* **20**, p21-25, (1993).
 14. Y.-H. Baek, J.-H. Oh, S.-G. Choi, W.-S. Sul, and J.-K. Rhee, “Comparison of the characteristic of Metamprpic HEMTs with different passivation materials”, *J. Korean Phys. Soc.* **54**, p1868, (2009).
 15. J. P. Connolly and C. Rohr, “Quantum well cells for thermophotovoltaics”, *Semicond. Sci. Technol.* **18**, S216-220, (2003).
 16. M. W. Wanlass, S. P. Ahrenkiel, R. K. Ahrenkiel, J. J. Carapella, R. J. Wehrer, and B. Wernsman, “Recent advances in low-bandgap, InP based GaInAs/InAsP materials and devices for thermophotovoltaic (TPV) energy conversion”, *AIP Conf. Proc.* **738**, p427-435, (2004).
 17. R. E. Nahory, M. A. Pollack, W. D. Johnston, and R. L. Barns, “Band gap versus composition and demonstration of Vegard’s law for $\text{In}_{1-x}\text{Ga}_x\text{As}_y\text{P}_{1-y}$ lattice matched to InP”, *Appl. Phys. Lett.* **33**, p659-661, (1978).
 18. G. C. Osbourn, “ $\text{In}_x\text{Ga}_{1-x}\text{As}-\text{In}_y\text{Ga}_{1-y}\text{As}$ strained layer superlattices: A proposal for useful, new electronic materials”, *Phys. Rev. B* **27**, p5126-5128 (1983).
 19. J.-Y. Marzin, M. N. Charasse, and B. Sermage, “Optical investigation of a new type of valence-band configuration in $\text{In}_x\text{Ga}_{1-x}\text{As}-\text{GaAs}$ strained superlattices”, *Phys. Rev. B* **31**, p8298-8301, (1985).
 20. K. B. Kahen and J. P. Leburton, “Optical constant of $\text{GaAs}-\text{Al}_x\text{Ga}_{1-x}\text{As}$ superlattices and multiple quantum wells”, *Phys. Rev. B* **33**, p5465-5472, (1986).
 21. I. J. Fritz, J. F. Klem, J. E. Schirber, J. A. Olsen, and W. A. Bonner, “InGaAs/GaAs multiple strained-layer structure grown on a lattice-matched InGaAs substrate wafer”, *Appl. Phys. Lett.* **66**, p1957-1959, (1995).
 22. Sadao Adachi and Kunishige Oe, “Internal strain and photoelastic effects in $\text{Ga}_{1-x}\text{Al}_x\text{As}/\text{GaAs}$ and $\text{In}_{1-x}\text{Ga}_x\text{As}/\text{P}_{1-y}/\text{InP}$ crystals”, *J. Appl. Phys.* **54** p6620-6627 (1983).

23. Y. Guldner, J. P. Vieren, M. Voos, F. Delahaye, D. Dominguez, J. P. Hirtz, and M. Razeghi, "Quantum Hall effect in $\text{In}_{0.53}\text{Ga}_{0.47}\text{As}$ -InP hetero junctions with two populated electric sub bands", *Phys. Rev. B* **33**, p3990-3993, (1986).
24. C. Lamberti and S. Bordiga, "Structure and optical investigation of $\text{InAs}_x\text{P}_{1-x}$ /InP strained superlattices", *J. appl. Phys.* **83**, p1058-1077, (1998).
25. W. A. Bonner, International Conference on Indium Phosphide and Related Materials, "Bulk ternary indium phosphide arsenide, $\text{InP}_{1-x}\text{As}_x$: growth and characterization", 11-15, p205-208, (1997).
26. K. J. Bachmann, F. A. Thiel and H. Schreiber, "Melt and solution growth of bulk single crystals of quaternary III-V alloys", Jr., *Progress in Crystal Growth and Characterization* 2, p171-206, (1979).
27. W.A. Bonner, B. J. Skromme, E. Berry, H. L. Gilchrist, R. E. Nahory, in: J.S. Harris (Ed.), *Inst. Phys. Conf. Ser.* 96, (1989) pp. 337
28. A. Tanaka, A. Watanabe, M. Kimura and T. Sukagawa, "The solute-feeding Czochralski method for homogeneous GaInSb bulk alloy pulling", *J. Crystal Growth*, **135**, p269-272, (1994).
29. K. Nakajima, K. Osamura, K. Yasuda and Y. Murakami, "The pseudo quaternary phase diagram of the Ga-In-As-Sb system", *J. Crystal Growth* **41**, p87-92, (1977).
30. K. Hashio, M. Tatsumi, H. Kato, K. Kinoshit, "Directional solidification of $\text{In}_x\text{Ga}_{1-x}\text{As}$ ", *J. Crystal Growth*, **210**, p471-477, (2000).
31. P. S. Dutta, Ch. 10. *Bulk Crystal Growth of Ternary III-V Semiconductors* in Springer Handbook of Crystal Growth (Eds: G. Dhanaraj, K. Byrappa, V. Prasad, and M. Dudley, Springer, 2010).
32. Y. Nishijima, K. Nakajima, K. Otsubo, and H. Ishikawa, *Indium Phosphide and Related Mater. Conf. Proc.*, 45 (1998).
33. P. S. Dutta, "III-V ternary bulk substrate growth technology: a review", *J. Crys. Growth* **275**, p106-112, (2005).
34. Y. Hayakawa, T. Ozawa, T. Araki, M. Haris, and M. Kumagawa, "Growth of InGaAs ternary bulk crystals by rotational Bridgman method", *J. Crys. Growth* **275**, e421-e425, (2005).

35. Y. Nishijima, H. Tezuka, and K. Nakjima, "A modified zone growth method for an InGaAs single crystal", *J. Crys. Growth* **280**, p364-371, (2005).
36. T. J. Kim, T. H. Ghong, Y. D. Kim, S. J. Kim, D. E. Aspnes, T. Mori, T. Yao, and B. H. Koo, "Dielectric functions of In_xGa_{1-x}As alloys", *Phys. Rev. B* **68**, p115323-115332, (2003).
37. S. Adachi, "Physical properties of gallium indium arsenide phosphide", *J. Appl. Phys.* **53**, p8775-8792, (1982).
38. S. Adachi and Kunishige Oe, "Properties of group IV, III-V and II-VI semiconductors", *J. Appl. Phys.* **56**, p74 (1984).
39. W. Yeo, R. Dimitrov, W. J. Schaff, and L. F. Eastman, "Material properties of bulk InGaAs and InAlAs/InGaAs heterostructures grown on (111) B and (111) B misoriented by 1° towards <211> InP substrates", *Appl. Phys. Lett.* **77**, p4292-4294 (2000).
40. Y. Fedoryshyn, M. Beck, P. Kaspar, and H. Jaechel, "Characterization of Si volume- and delta-doped InGaAs grown by molecular beam epitaxy", *J. Appl. Phys.* **107**, p093710 (2010).
41. R. Bhat, P.S. Dutta, and S. Guha, "Crystal growth and below-bandgap optical absorption studies in InAs for non-linear optic applications", *J. Crystal Growth* **310**, p1910-1916, (2008).
42. S. Adachi, "Physical properties of gallium indium arsenide phosphide", *J. Appl. Phys.* **53**, p8775-8792, (1982).
43. S. Adachi, "Optical properties of In_{1-x}Ga_xAs_yP_{1-y} alloys", *Phys. Rev. B* **39**, p12612-12621 (1989).
44. S. M. Kelso, D. E. Aspnes, M. A. Pollack, and R.E. Nahory, "Optical properties of In_{1-x}Ga_xAs_yP_{1-y} from 1.5 to 6.0 eV determined by spectroscopic ellipsometry", *Phys. Rev. B* **26**, p6669-6681, (1982).
45. <http://www.google.com/images?q=semiconductor+band+structures>
46. Shekhar Guha "Nonlinear Properties of Semiconductor", Research group meeting
47. P.S. Dutta, "Bulk Crystal Growth of Ternary III-V Semiconductors", SPIN, Springer *Hand book of Experimental Solid Mechanics*, 2009.

48. W.A. Bonner, B. Lent, et al, “substrate-quality ternary III-V single crystal for II-VI device applications: growth and characterization”, *SPIE* 2228, p33-43, (1994).
49. K. Nakajima, K. Osamur, et al, “InGaAs single crystal with a uniform composition in the growth direction grown on an InGaAs seed using the multi component zone growth method”, *J. Crystal Growth*, **208**, p171-178, (2000).
50. A. Tanak, A. Watanabe, et al, “Multi-step pulling of GaInSb bulk crystal from ternary solution”, *J. Crystal Growth*, **209**, p625-629, (2000).
51. P.S. Dutt and T. R. Miller, “Engineering phase formation thermo chemistry for crystal growth of homogeneous ternary and quaternary III-V compound semiconscious from melts”, *J. Electronic Materials* **29**, p956-963, (2000).
52. <http://www.google.com/imgres?imgurl=http://www.ll.mit.edu>
53. <http://www.google.com/imgres?imgurl=http://www.phys.au.dk>.
54. Ashcroft/Mermin, “*Solid State Physics*”, Brookscole Thomson , (1975), chapter 9
55. <http://www.google.com/imgres?imgurl=http://www.physics.ucsd.edu>
56. Varshni, Y. P., “Temperature dependence of the energy gap in semiconductors”, *Physica* **34**, p149-154, (1967).
57. Dr. Phil Milson private communication
58. Van der Pauw, L.J. “A method of measuring specific resistivity and Hall effect of discs of arbitrary shape,” *Philips Research Reports* 13: p1–9, (1958).
59. Elizabeth A. Moore. “*Electrical Activation Studies of Silicon*”, PhD dissertation, AFIT, 2008.
60. Perkin Elmer Spectrum GX manual (www.Perkin Elmer.com)
61. Yacobi, B. G. *Cathodoluminescence Microscopy of Inorganic Solids*. New York: Plenum Press (1990).
62. Fellows, James. “*Electrical Activation studies of ion implanted GaN*”, PhD Dissertation, AFIT, 2001.
63. John C. Brasunas and G. Mark Cushman, “Interferometric but nonspectroscopic technique for measuring the thickness of a transparent plate,” *Opt. Eng.* **34**, p2126 – 2130, (1995).

64. Glen D. Gillen and Shekhar Guha, "Use of Michelson and Fabry-Perot interferometry for independent determination of the refractive index and physical thickness of wafers," *Appl. Opt.* **44**, p344 – 347, (2005).
65. Glen D. Gillen and Shekhar Guha, "Refractive-Index Measurements of Zinc Germanium Diphosphide at 300 and 77K by Use of a modified Michelson Interferometer", *Appl. Opt.* **43**, p2054-2058, (2004).
66. H. W. Icenogle, B. C. Platt, and W. L. Wolfe, "Refractive indexes and temperature coefficients of germanium and silicon," *Appl. Opt.* **15**, (10) p2348-2351, (1976).
67. Gary Hawkins and Roger Hunneman, "The temperature dependent spectral properties of filter substrate materials in the far infrared (6-40 μm)", *Infrared Phys. Technol.* **45**, p69-79, (2004).
68. http://www.sbfpr.com/imagir_camera.html
69. Z. M. Fang, K. Y. Ma, et al "Photoluminescence of InSb, InAs, and InAsSb growth by organometallic vapour phase epitaxy", *J. Appl. Phys.* **67** (11), p7034-7039, (1990)
70. Pallab Bhattacharya, *Semiconductor Optoelectronic Devices*, Prentice-Hall, 2nd Edition 1997, p 131.
71. T. S. Moss, *J. Appl. Phys.* **32**, 2136 (1961).
72. M. D. Sturge, "Optical Absorption of Gallium Arsenide between 0.6 and 2.75 eV", *Phys. Rev.* **127**, p768-773, (1962).
73. F. Urbach, "The long wavelength edge of photographic sensitivity and of the electronic absorption of solids", *Phys. Rev.* **92**, p1324-1324, (1953).
74. E. O. Kane, "Band structure of indium antimonite", *J. Phys. Chem. Solids* **1**, p249-261, (1957).
75. V. Ariel, V. Garber, D. Rosenfeld, and G. Bahir, "Estimation of HgCdTe band-gap variations by differentiation of the absorption coefficient", *Appl. Phys. Lett.* **66** (16) p2101-2103, (1995).
76. <http://www.ioffe.ru/SVA/NSM/Semicond>
77. Sadao Adachi, "Band gaps and refractive indices of AlGaAsSb, GaInAsSb, and InPAsSb: Key properties for a variety of the 2-4 μm optoelectronic device applications", *J. Appl. Phys.* **61** (10), p4869-4876, (1987).

78. Jacques I. Pankove, *Optical Processes in Semiconductors*, Dover publications, Inc. p36, (1975).
79. J. Bardeen, F. J. Blatt, and L. H. Hall, *Proc. Of Atlantic City Photoconductivity Conference* (1954), J. Wiley and Chapman and Hall, p 146, (1956).
80. J. Wei, J. Barnes, S. Guha, L. P. Gonzalez, Y. K. Yeo, R. L. Hengehold and G. Rajagopalan, : “Electrical and Optical Characterization of Melt Grown Bulk InAs_{1-y}Py Crystals”, 40 (2) Journal of Electronics Materials, **40** (2) p1432-9 (2011).
81. Brigham Young University web: http://www.cleanroom.byu.edu/EW_ternary.phtml
82. P. J. P. Tang, C. C. Phillips and R. A. Stradling, “Excitonic photoluminescence in high purity InAs MBE epilayers on GaAs substrates”, Semicond. Sci. Tech. **8**, p2135-2138 (1993).
83. M. Fisher and A. Krier, “Photoluminescence of epitaxial InAs produced by different growth methods”, *Infrared Phys. Tech.* **38**, p405-413, (1997).
84. R. D. Grober and H. D. Drew, “Evidence for an electron-hole plasma in the photoluminescence spectra of insulating InSb at very low pump intensities”, *Phys. Rev. B* **43**, p11732-11739, (1991).
85. S. B. Nam, D. C. Reynolds, C. W. Litton, R. J. Almassy, T. C. Collins, and C. M. Wolfe, “Free exciton energy spectrum in GaAs”, *Phys. Rev. B* **13**, p761-767, (1976).
86. Y. K. Yeo, A. C. Bergstrom, R. L. Hengehold, J. Wei, S. Guha and L. P. Gonzalez, G. Rajagopalan, Mee-Yi Ryu, “Optical and Electrical Properties of Bulk-Grown Ternary In_xGa_{1-x}As”, Accepted for publication at Journal of the Korean Physical Society 2010.

REPORT DOCUMENTATION PAGE				Form Approved OMB No. 074-0188	
<p>The public reporting burden for this collection of information is estimated to average 1 hour per response, including the time for reviewing instructions, searching existing data sources, gathering and maintaining the data needed, and completing and reviewing the collection of information. Send comments regarding this burden estimate or any other aspect of the collection of information, including suggestions for reducing this burden to Department of Defense, Washington Headquarters Services, Directorate for Information Operations and Reports (0704-0188), 1215 Jefferson Davis Highway, Suite 1204, Arlington, VA 22202-4302. Respondents should be aware that notwithstanding any other provision of law, no person shall be subject to a penalty for failing to comply with a collection of information if it does not display a currently valid OMB control number.</p> <p>PLEASE DO NOT RETURN YOUR FORM TO THE ABOVE ADDRESS.</p>					
1. REPORT DATE (DD-MM-YYYY) 24-03-2011		2. REPORT TYPE Dissertation		3. DATES COVERED (From – To) Nov. 2008 – Jan. 2011	
4. TITLE AND SUBTITLE Optical and Electrical Characterization of Melt-Grown Bulk InxGa1-xAs and InAs1-yPy Alloys				5a. CONTRACT NUMBER	
				5b. GRANT NUMBER	
				5c. PROGRAM ELEMENT NUMBER	
6. AUTHOR(S) Jean Wei				5d. PROJECT NUMBER	
				5e. TASK NUMBER	
				5f. WORK UNIT NUMBER	
7. PERFORMING ORGANIZATION NAMES(S) AND ADDRESS(S) Air Force Institute of Technology Graduate School of Engineering and Management (AFIT/EN) 2950 Hobson Way, Building 640 WPAFB OH 45433-7765				8. PERFORMING ORGANIZATION REPORT NUMBER AFIT/DS/ENP/11-M02	
9. SPONSORING/MONITORING AGENCY NAME(S) AND ADDRESS(ES) Dr. Kitt Reinhardt and Dr. Gernot Pomrenkl Directorate of Physics and Electronics Air Force Office of Scientific Research (AFOSR/RSE) 875 N. Randolph St. Arlington, Virginia 22203				10. SPONSOR/MONITOR'S ACRONYM(S)	
				11. SPONSOR/MONITOR'S REPORT NUMBER(S)	
12. DISTRIBUTION/AVAILABILITY STATEMENT APPROVED FOR PUBLIC RELEASE; DISTRIBUTION UNLIMITED.					
13. SUPPLEMENTARY NOTES					
14. ABSTRACT A new method to determine semiconductor bandgap energy directly from the easily measured transmission spectra was developed. The method was verified using many binary semiconductors with known properties and utilized to determine the unknown ternary semiconductors were determined at various wavelengths and temperatures. Photoluminescence and Hall-effect measurement were performed to identify various electronic transitions, as well as sample quality. The determination of electrical and optical properties of the material will provide important addition to the database of material properties for future optoelectronic device applications. In the near future, newer materials and their applications need to be developed, and often binary and ternary III-V compounds (GaSb, GaP, GaSbP etc.) can be studied using the method developed in this work.					
15. SUBJECT TERMS Bulk III-V semiconductors, Optical Characterization, Electrical Characterization, Photoluminescence, Bandgap energy, Fourier Transform Infrared spectroscopy, Transmission spectra.					
16. SECURITY CLASSIFICATION OF:			17. LIMITATION OF ABSTRACT	18. NUMBER OF PAGES	19a. NAME OF RESPONSIBLE PERSON
a. REPORT	b. ABSTRACT	c. THIS PAGE			Dr. Yung Kee Yeo, ENP
U	U	U	UU	160	19b. TELEPHONE NUMBER (Include area code) (937) 255-3636, x5432; email: yung.yeo@afit.edu